CARBON ION IMPLANTED SILICON FOR SCHOTTKY LIGHT-EMITTING DIODES

A Thesis Submitted to the College of
Graduate Studies and Research
In Partial Fulfillment of the Requirements
For the Degree of Doctor of Philosophy
In the Department of Physics and Engineering Physics
University of Saskatchewan
Saskatoon

By

Sarah K. Purdy

PERMISSION TO USE

In presenting this thesis in partial fulfilment of the requirements for a Postgraduate degree from the University of Saskatchewan, I agree that the Libraries of this University may make it freely available for inspection. I further agree that permission for copying of this thesis in any manner, in whole or in part, for scholarly purposes may be granted by the professor or professors who supervised my thesis work or, in their absence, by the Head of the Department or the Dean of the College in which my thesis work is done. It is understood that any copying or publication or use of this thesis or parts thereof for financial gain shall not be allowed without my written permission. It is also understood that due recognition shall be given to me and to the University of Saskatchewan in any scholarly use which may be made of any material in my thesis.

Requests for permission to copy or to make other use of material in this thesis in whole or part should be addressed to:

Head of the Department of Physics and Engineering Physics

116 Science Place

University of Saskatchewan

Saskatoon, Saskatchewan

Canada

S7N 5E2

ABSTRACT

Research in the field of Photonics is in part, directed at the application of light-emitting materials based on silicon platforms. In this work silicon wafers are modified by carbon ion implantation to incorporate silicon carbide, a known light-emitting material. Ion beam synthesis treatments are applied with implant energy of 20 keV, and ion fluences of 3, 5 and 10×10^{16} ions/cm^2 at both ambient temperature and high temperature (400 °C). The samples are annealed at 1000 °C, after implantation.

The carbon ion implanted silicon is characterized using Raman and Fourier transform infrared spectroscopic techniques, grazing-incidence X-ray diffraction, transmission electron microscopy and electron energy loss spectroscopy. The materials are observed to have a multilayer structure, where the ambient temperature implanted materials have an amorphous silicon layer, and an amorphous silicon layer with carbon-rich, nanoscale inclusions. The high temperature implanted materials have the same layers, with an additional polycrystalline Si layer at the interface between the implanted layer and the target substrate and the amorphous Si layer with SiC inclusions is reduced in thickness compared to the ambient temperature samples. The carbon-rich inclusions are confirmed to be SiC, with no evidence of carbon clusters in the materials observed using Raman spectroscopy.

The carbon ion-implanted material is used to fabricate Schottky diodes having a semitransparent gold contact at the implanted surface, and an aluminum contact on the opposite side. The diodes are tested using current-voltage measurements between -12 and +15 V. No reverse breakdown is observed for any of the diodes. The turn-on voltages for the ambient temperature implanted samples are 2.6±0.1 V, 2.8±0.6 V and 3.9±0.1 V for the 3, 5 and 10×10^{16} ions/cm^2 samples, respectively. For the high temperature implanted samples, the turn-on

voltages are 3.2±0.1 V, 2.7±0.1 V, and 2.9±0.4 V for the implanted samples with same fluences. The diode curves are modeled using the Shockley equation, and estimates are made of the ideality factor of the diodes. These are 188±16, 224.5±5.8, and 185.4±9.2 for the ambient temperature samples, and 163.6±6.3, 124.3±5.3, and 333±12 for the high temperature samples. The high ideality factor is associated with the native oxide layer on the silicon substrate and with the non-uniform, defect-rich implanted region of the carbon ion implanted silicon.

Red-orange visible light emission from the diodes is observed with voltage greater than the turn-on voltage applied across the diodes. The luminescence for the ambient temperature samples is attributed to porous silicon, and amorphous silicon. The high temperature implanted samples show luminescence associated with porous silicon, nanocrystalline silicon carbide, and defects in silicon related to ion implantation. The luminescent intensity observed for the ambient temperature samples is higher than for the high temperature samples. The dominant luminescence feature in the carbon ion-implanted silicon material is porous silicon, which is described by quantum confinement of excitons in silicon.

ACKNOWLEDGEMENTS

I would like to express my deepest gratitude to my supervisors Michael P. Bradley and Gap Soo Chang. Their patience and guidance have helped me greatly during the course of my project. I would like to thank my committee members: Tim Kelly, Peter Mascher, Kaori Tanaka, and Chijin Xiao, for their feedback over the course of my work and on my thesis. I am grateful to the Faculty and Staff of the Physics and Engineering Physics Department their support and engagement in my academic and extra-curricular progress and success. Materials synthesis for this project is conducted at the Centre for Emerging Device Technologies at McMaster University in collaboration with Dr. Andrew Knights and Doris Stevanovic. Data collection is assisted by Himanshu Rai, Junyi Yang and at the University of Saskatchewan; Victoria Jarvis at the McMaster Analytical X-ray Diffraction facility; and Andreas Korinek at the Canadian Centre for Electron Microscopy.

I am immeasurably grateful to my parents and my sister for all of the support and advice they have given over the years. I am glad to have worked with many excellent graduate students: Robert Bauer, Paul Bazylewski, Jesse Hall, Adrian Hunt, Darren Hunter, John A. McLeod, David Muir, Niloofar Zarifi, and many others.

This research has been funded by the NSERC Discovery Grants Program via the grant entitled "New Methods and Ideas in Silicon Photonics" as well as the University of Saskatchewan President's NSERC Fund. Abacus Consulting Services Ltd has also supported this research. The Herzberg Travel award was presented twice for presentation of this work at national and international conferences. I am deeply thankful to have received the Alex Kavadas Memorial Scholarship (2011, 2012), and the Russel Haid Memorial Scholarship (2012) as support for my PhD work.

TABLE OF CONTENTS

LIST OF TABLES

LIST OF FIGURES

LIST OF ABBREVIATIONS

3C-SiC	Silicon carbide, zinc blende polytype (see also β-SiC)
6H-SiC	Silicon carbide, hexagonal polytype (see also α-SiC)
α-SiC	Silicon carbide, hexagonal polytype (see also 6H-SiC)
β-SiC	Silicon carbide, zinc blende polytype (see also 3C-SiC)
a-Si	Amorphous silicon
a-SiC	Amorphous silicon carbide
a-$Si_{(1-y)}C_y$	Amorphous sub-stoichiometric SiC
a-SiC:H	Hydrogenated amorphous silicon carbide
Al	Aluminum
Ar	Argon
ARO	All-reflective objective
AT	Ambient temperature
Au	Gold
BF	Bright field
C	Carbon
C^+	Carbon ion (positive)
C:Si	Carbon ion implanted silicon
c-Si	Crystalline silicon
CCEM	Canadian Centre for Electron Microscopy
CEDT	Centre for Emerging Device Technology
CMOS	Complimentary metal-oxide semiconductor
Cu	Copper

DF	Dark field
EELS	Electron energy loss spectroscopy
EL	Electroluminescence
FTIR	Fourier-transform infrared
FWHM	Full width at half maximum
G-XRD	Grazing-incidence X-ray diffraction
H^+	Hydrogen ion (positive)
H	Hydrogen
HAADF	High-angle annular dark field
HOPG	Highly ordered pyrolitic graphite
HT	High temperature
HV	High voltage
IBS	Ion beam synthesis
IGBT	Insulated-gate bipolar transistor
IR	Infrared
I-V	Current - voltage
J-V	Current density - voltage
LED	Light-emitting diode
MAX	McMaster Analytical X-ray
N_2	Nitrogen gas
nc-Si	Nano-crystalline silicon
nc-SiC	Nano-crystalline silicon carbide
N	Nitrogen

Ni	Nickel
O	Oxygen
p-Si	Porous silicon
p-SiC	Porous silicon carbide
PIII	Plasma immersion ion implantation
PL	Photoluminescence
PVD	Physical vapor deposition
RF-ICP	Radio frequency inductively coupled plasma
RF	Radio-frequency
RSS	Residual sum of squares
Si	Silicon
SiC	Silicon carbide
SOI	Silicon-on-insulator
SRIM	Stopping and range of ions in matter
SSSC	Saskatchewan Structural Sciences Centre
TEM	Transmission electron microscopy
U of S	University of Saskatchewan
Xe	Xenon
XRD	X-ray diffraction

CHAPTER 1

INTRODUCTION

Computer technologies from supercomputers to personal computers operate using multi-core processors [1], and the number of processing cores ranges from two up to several hundred cores on one chip [2]–[4]. These multi-core processors use traditional metal wire connections to transmit and receive information. The processing speed is limited by the scale of the wires used: as the wires become smaller and more closely packed, cross-coupling between them induces noise [5], and at nanoscale the properties of the wires can be very different [6]. Photonics research has the potential to overcome these limitations and aims to replace metallic connections, with silicon (Si) or other semiconductor materials that emit, transmit, modulate and receive light [3], [4]. The need for silicon-compatible components that can be included in currently existing manufacturing infrastructure is a topic of ongoing development [3], [7]–[9]. Optoelectronic high-speed modulators [10]–[12], waveguides [13]–[15], and detectors [16]–[20] have been developed for silicon platforms, as have light-emitting diodes (LEDs) [21]–[23]. Some of these devices use other optoelectronic materials that need to be specially bonded to silicon platforms [24]–[26]. In order to avoid this added manufacturing step, there is interest in developing silicon-based components. The development of such components is challenging, in part because Si has an indirect band gap shown in Figure 1.1 [27]. The recombination of an electron-hole pair in a material with an indirect band gap requires the interaction between the electron, the photon, and a phonon, which has a lower probability than a direct band gap interaction that does not require a phonon [27].

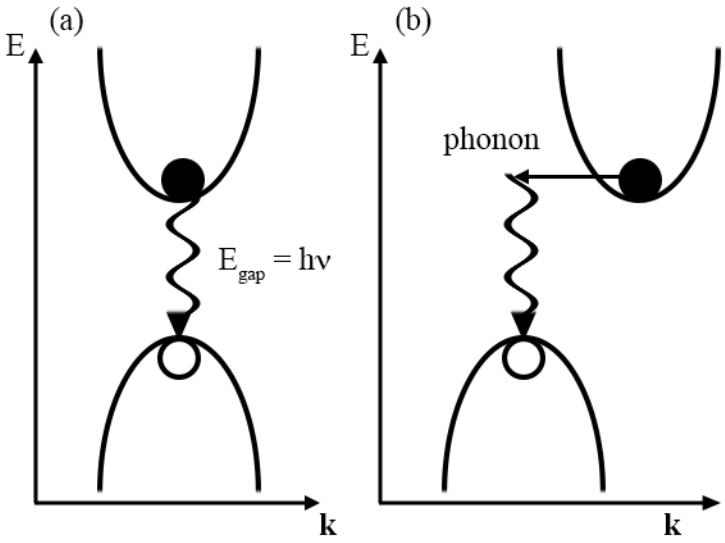

Figure 1.1 (a) Direct band gap materials may emit a photon when an electron in the conduction band combines with a hole in the valence band of the material. (b) In materials with an indirect band gap the electron must change momentum by electron-phonon interaction in order to undergo the recombination process.

It is appealing to use ion implantation processing when researching silicon photonic materials, since ion implantation is widely used in contemporary silicon device fabrication. The development of the implantation parameters could be easily implemented for use in industrial scale processing, with existing infrastructure and techniques.

The research presented here is motivated towards producing Si that is modified to emit light for photonic applications such as on-chip optical interconnects for multi-core processors. The materials discussed in this thesis may also be applied in high-voltage (HV) electronics and complimentary metal-oxide-semiconductor (CMOS) applications. In this work, silicon wafers with boron doping (*p*-type) are modified using ion beam synthesis (IBS) to implant mass-selected carbon ions (C^+), followed by annealing to facilitate the formation of silicon carbide (SiC) within the Si target [28]. Light emission from SiC was first reported by H. Round in the early 1900s [29], therefore the SiC is expected to contribute to the luminescence of light-emitting Schottky diodes fabricated for this study with the hope of accessing the green-blue region of the

emission spectrum. A subset of targets is heated during the implantation process to investigate the effect of *in situ* annealing on SiC formation in the C:Si, and on LED device performance. The ion implantation energy is selected with the goal of process transfer from IBS to Plasma Immersion Ion Implantation (PIII). The carbon ion implanted silicon (C:Si) is characterized using Fourier transform infrared (FTIR) and Raman spectroscopic techniques, as well as X-ray diffraction (XRD), transmission electron microscopy (TEM) and electron energy loss spectroscopy (EELS). This array of materials characterization techniques is used to identify the composition and structure of the synthesized C:Si material. Schottky diodes consisting of metal-semiconductor interface with rectifying behavior are fabricated from the C:Si, and the current-voltage (*I-V*) and electroluminescence (EL) characteristics are observed from working devices. The luminescence mechanisms for the LEDs are determined, the fabrication process and the suitability of further study and application are discussed as a result of this study.

1.1. Silicon Carbide Light-Emitting Diodes

Silicon carbide materials are studied for photovoltaic [30] and light-emitting applications, discussed in this section. The mechanical and structural properties of Si and SiC are summarized in Table 1.1. The first SiC diode fabricated using ion implantation was reported by Marsh and Dunlap in 1970, using *n*-type dopants in hexagonal and cubic SiC to generate *p-n* junctions [31]. Blue light-emitting SiC diodes are commercially available, patented by Cree Inc. in 1990 [32]. The similar structures of Si and SiC present an opportunity to work with stoichiometric and non-stoichiometric compounds. The crystal structure of SiC may take on any of a range of polytypes, including cubic and hexagonal structures, shown in Figure 1.2, with the stacking of the layers in

Table 1.1 Properties of Si and SiC.

	Silicon	**β-SiC**	**α-SiC**
Crystal structure [33]	diamond	zinc blende (cubic)	hexagonal
Lattice constant (Å) [33]	5.4310	4.3596	3.0806, 15.1173
Density (g/cm^3) [33]	2.3291	3.2142	3.2153
Band gap (eV) [33]	1.12	2.39	3.0
Melting point (K) [33]	1687	2810	2810
Thermal conductivity (mW/cm·K) [34], [35]	1.240	3.6	4.9

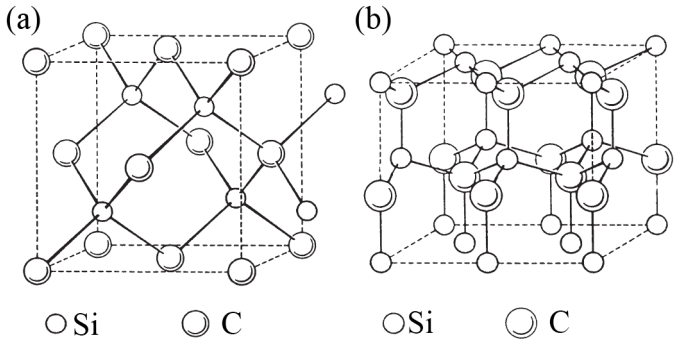

Figure 1.2 Illustration of (a) cubic and (b) hexagonal crystal structures. Adapted from: W.D. Kingery *et al*., "Introduction to Ceramics", 2nd ed., Wiley, New York, 1976 [36].

the unit cell having a range of offsets [33]. The most commonly discussed polytypes for our purposes are 3C-SiC (β-SiC) zinc blende (cubic), and 6H-SiC (α-SiC) hexagonal structure

The high thermal conductivity, and the mechanical and chemical stability of SiC make it appealing for high-powered electronics and hostile operating environments, further expanding the applications for research in C:Si materials [37]. The luminescence properties of SiC are of interest for this work. The EL of SiC in blue, green, yellow and orange colours were first (briefly) remarked upon by H. J. Round in 1907 [29]. Early investigations into "The fabrication of SiC Electroluminescent displays" [38] were presented by Philips company [39] and General Electric company [Brander, R. W., *G. E. C. J. Sci. Technol.* **32**, pp. 15, (1965) [40] and [41]]. Brander included use of ion implantation to investigate cathodoluminescence (CL) (light emission stimulated by electron bombardment) in SiC implanted with krypton and helium. The same luminescence was seen by Hamilton, Choyke and Patrick near 540 nm (2.3 eV) at 77 K, and is attributed to exciton recombination in SiC [42].

1.2. Ion implantation for Synthesis of Silicon Carbide

Ion implantation is a technique that is used to synthesize SiC for high-powered, photovoltaic and photonic applications. Two common implantation techniques are IBS [43]–[49] and PIII [50]–[52], details are discussed in Chapter 3. Early application of ion implantation for SiC semiconductor technology was focused on incorporation of dopants in crystalline SiC targets [41]. The main dopants for SiC are nitrogen (*n*-type) and aluminum (*p*-type) [37]. Implantation of inert elements (helium, argon, krypton, xenon), or implantation without the intention of incorporating the implanted ion (nitrogen that would outgas after annealing) has been used to explore structural defect-related properties of SiC [53].

The first application of C:Si for synthesis of SiC was presented by Borders [28], using IBS to implant C^+ ions at a fluence of 10^{17} ions/cm^2 at 200 keV into *p*-type Si. The adaptation of PIII for synthesis of SiC makes use of methane (CH_4), acetylene (C_2H_2), or toluene (C_7H_8) as a precursor gas to generate C^+ for implantation [50], [51], [54]–[56]. The molecular ions break apart on impact with the target surface, and each atom from the molecule is implanted with a fraction of the implant energy that is dependent on its atomic weight and the number of atoms in the molecule. Larger molecules result in smaller energy-fractions transferred to the component atoms, for example this would make toluene less suitable for C^+ implantation than methane [51].

The formation mechanism of SiC crystallite inclusions from implanted materials is described by Wang *et al*. using the 3-dimensional Avrami equation for growth of a transformed volume of material from one phase to another [57], [58]. Carbon has poor solubility in silicon, the maximum concentration of carbon in silicon solid solution is reported as (4.5×10^{17} cm^{-3}) [59], [60]. In the case of high-fluence ion implantation, used for C:Si materials, the carbon aggregates in carbon clusters [44], [61]. For the C:Si discussed in this thesis the carbon concentration is $\leq 1.2 \times 10^{22}$ ions/cm^3 in Si (density of 5×10^{22} atoms/cm^3) which corresponds to a relative concentration of $\leq$24%.

The implantation process results in breaking of the bonds of the Si crystal target, leaving Si available to bond with the alien C^+. Annealing provides energy for Si—C bonds to form, which nucleates a cubic β-SiC cluster that has the same crystal orientation as the native lattice [46]. The SiC lattice constant is smaller than the Si lattice constant, leaving space for more Si—C bonds to form and grow the SiC inclusion [33], [46]. The formation of Si—O bonds (from oxygen impurities natural to the target, or implanted intentionally) also serves to create space for growth of SiC inclusions in ion-implanted silicon [43]. Carbon ion implantation through a

capping SiO_2 layer is shown to promote growth of a buried SiC layer at the SiO_2/Si interface [62]. The formation of ß-SiC in C:Si is limited by the formation of amorphous C, Si and SiC and by the number of ions implanted compared to the number of ions lost by sputtering in the implantation process [43], [51].

The work presented in this thesis uses IBS with mass-selected C^+ ions to implant to Si targets. Based on previous work outlined in this section, the native oxide layer of the Si targets is not removed before ion treatment, since it is known to enhance SiC growth in the target [43].

1.2.1. Ion Implantation Parameters

The parameters for ion implantation synthesis are selected for the intended stoichiometry and physical position of the implanted layer. The stoichiometry depends on the energy and the fluence (ions/cm^2) which are user-controlled parameters of a typical ion implantation treatment [28]. It is important to distinguish between ion fluence and concentration of implanted impurities in the target. The fluence is the number of ions implanted into the surface of the target per unit area (ions/cm^2), it is sometimes called "dose" [63], [64]. The concentration of ions is used in the traditional meaning, the number of ions in a unit volume (ions/cm^3) of material, and this can vary with depth in the sample.

The energy of the implanted ions and the density of the target determine the distribution of implanted atoms within the target, and are calculated using a Stopping and Range of Ions in Matter (SRIM) program, discussed further in Chapter 3 [65]. The implant energy is determined by the desired position of implanted layer. Ion implantation studies of C:Si materials use implantation energies as low as 15 keV [55] and as high as 300 keV [66]. The ion fluence depends on the ion distribution in the target after implant, during the implantation process. The

fluence of C^+ ions is selected for the desired stoichiometry of the implanted region based on the simulated ion distribution, described in section 3.1.3 [65]. Stoichiometric [28], [48], [67]–[69] and sub-stoichiometric (Si_xC_{1-x}, $x < 1$) [66], [70] SiC, and hydrogenated amorphous SiC (a-SiC:H) [50], [55] buried layers in Si have been generated by the C:Si process.

The implantation process necessarily damages the structure of the target; higher fluence induces more damage. Oostra *et al.* report a hetero-junction bipolar transistor fabricated using ion implantation, and demonstrate that the device suffers from non-uniform interface between the implanted region and the substrate due to this effect [70]. This defect-rich region negatively affects device performance [70]. A low energy implant, with relatively thin implanted ion distribution could reduce the thickness of the defect region at the interface. The energy selected for ion implantation is chosen to be 20 keV for the present work, which has the added benefit of matching the capabilities of the PIII reactor at the University of Saskatchewan for a later stage in the C:Si project.

The threshold for SiC formation based on ion fluence is determined by over-stoichiometry and sputtering of atoms from the target. High-fluence implantations that result in carbon-silicon ratios above unity are shown to generate graphitic and amorphous carbon inclusions in addition to the SiC buried layer [44], [71]. The excess carbon inhibits growth of SiC crystals [44]. SiC has a distinct absorption band in the infrared (IR) spectrum that can be used to quantify the amount present [44]. The full width at half-maximum (FWHM) of the SiC IR band reaches a maximum at the saturation concentration, with corresponding fluence, for C:Si materials [56]. The saturation fluence for C:Si has been observed using PIII of methane (1.1×10^{18} ions/cm^2 at -40 keV), and IBS with C^+ (5×10^{17} ions/cm^2 at 65 keV, and 1.2×10^{18} ions/cm^2 at 90 keV) [47], [51], [56].

Implantation of stoichiometric SiC with the hope of generating uniform, buried crystalline layers is one area of focus of previous work on C:Si materials. The use of target heating and post-implant heavy ion irradiation to induce re-crystallization are cited as techniques that assist in the formation of a single-crystal SiC layer [44], [49], [67]. However, some lattice defects persist after recrystallization of the implanted material [49]. In contrast, other studies are constructed to emulate the intense luminescence seen in porous silicon (p-Si)[1] by synthesizing porous SiC (p-SiC) or amorphous SiC (a-SiC) by implanting with a heavy element such as germanium before C^+ implantation, or implanting to electrochemically etched p-Si, or annealing then anodizing the C:Si [52], [68], [72]–[76]. These reports show luminescence from the p-SiC in the blue region of the visible spectrum [52], [68], [72]–[74].

Silicon target density and formation of SiC are influenced by heating the target during implantation [77], [78]. It has been shown that heating the target during C^+ ion implantation to Si enhances SiC bond formation and crystal growth [67], [78]. Temperatures from 400 °C to 950 °C have been reported [46], [48]. In the case of PIII treatment with hydrocarbon molecules, target heating above 500 °C reduces the amount of hydrogen incorporated in the C:Si, and temperatures above 850 °C expel the accompanying hydrogen from the target [54].

The purpose of this study is to examine EL of annealed C:Si with respect to ion dose and application of high temperature implantation at low energy. The energy for the implantation is chosen to be 20 keV for a thin (projected range ~660 Å see Section 3.1) buried layer, the energy is selected to match the capabilities of the PIII reactor at the University of Saskatchewan. The fluence of the implantation experiment is also limited by ion beam stability at low implant

[1] There may be confusion regarding p-Si referring to "porous" and *p*-type Si. Let it be clarified here that amorphous Si is denoted as "a-Si" and crystalline Si is "c-Si." By this convention, the sensible notation for porous Si should be "p-Si" referring to the phase of the material, and "*p*-type Si" refers to the doping of the semiconductor.

energy, 20 keV. The fluences are selected as 3, 5, and 10×10^{17} ions/cm^2. The target temperature is set to 400°C, based on the capabilities of the heating stage of the IBS implanter at the Center for Emerging Device Technologies (CEDT).

1.2.2. Post-implant Treatment

Ion implantation of carbon into silicon results in interstitial carbon and Si—C compounds, a-SiC, and carbon clusters [50], [61], [66]–[68]. Post-implant annealing is a common method for promoting the formation of Si—C bonds in C:Si materials. The melting point of silicon is 1414 ˚C and that of ß-SiC is 2797 ˚C [33]. Borders *et al*. showed that annealing at temperatures above 850 ˚C enhances crystalline ß-SiC growth in C:Si [28]. It is also shown that ß-SiC is stable during annealing of C:Si and that amorphous carbon introduced by high fluence implantation can be eliminated by the annealing process [50], [67], [79]. Additionally, high-temperature annealing is known to reduce defects that reduce carrier lifetime and mobility in ion implanted materials, resulting in improvement of device performance for *p-n* junctions fabricated from C:Si [66]. The non-uniformity of the interface between the implanted region and the substrate is also reduced (but not eliminated) after annealing above 900 ˚C [70]. The optimal annealing temperature for C:Si at 65 keV is reported to be 1100 ˚C [71]. The growth kinetics of SiC in C:Si during the annealing process is described by classical theory of crystal phase changes [57].

Recrystallization of SiC in C:Si has also been achieved by post-implant irradiation using Si^+, xenon (Xe^{2+}), and nickel (Ni^{8+}) [45], [49], [80], with varying levels of success. Pérez-Rodríguez *et al.* use Si^+ ions to irradiate the C:Si, and report formation of SiC crystal inclusions with size varied by depth in the target [80]. Irradiation with Xe ions is shown to recrystallize the

C:Si, depending on the implant energy [45]. Use of Ni ions for irradiation did not result in crystallization of the prepared C:Si [49].

Crystallization of the implanted region of C:Si materials is of major interest for improved device performance, and p-SiC is reported in the literature for applicability in blue light-emitting applications [68], [72]–[74]. Porous Si on a c-Si substrate is synthesized by an anodization process using the post-anneal C:Si as an anode in a hydrofluoric acid:ethanol etching mixture. The porous layer is constructed with the intention of accessing quantum confinement of charge carriers to manipulate the colour of light emission [72], [76].

Post-implant annealing appears to be the more reliable and less expensive method for crystallizing the C:Si and improving device performance. The optimal annealing temperature is 1100 ˚C, however, due to the capacity of the furnace available for the current work, an annealing temperature 1000 ˚C is used for this work, which is within the range of annealing temperatures reported in the literature [71]. The results of materials characterization methods (FTIR, PL and EL, XRD and scanning TEM) from previous work on C:Si experiments are used for comparison with the work presented in this thesis. The significance of each method is discussed in Chapter 3.

1.3. Characterization of Carbon Ion Implanted Silicon Materials

Characterization of C:Si materials can be done using a wide range of tools for investigating the chemical and physical structure of the implanted region. For this work, the characterization methods are selected to be easily accessible, inexpensive, and widely used. FTIR and Raman spectroscopic techniques are used to verify the chemical composition of the materials. FTIR is used to identify the Si—C transverse-optical (TO) phonon peak in hexagonal and cubic SiC is observed at ~800 cm^{-1} [81], [82]. In as-implanted C:Si materials the Si—C peak

appears broadened with peak position at 700-740 cm^{-1}, this is interpreted to be amorphous SiC [28]. After annealing at 800 ˚C the Si—C peak appears sharpened, with peak position ~800 cm^{-1} [55]. Khamsuwan *et al.* demonstrate this change in SiC structure after irradiation with Xe ions at 4 MeV as a post-implant treatment instead of annealing [45]. For annealing temperatures above 600 ˚C, An *et al*. report a peak at 1080 cm^{-1} attributed to formation of silicon sub-oxide (SiO_x, $x < 2$) [55]. The FWHM of the SiC peak may be compared to the implantation fluence [56]. For fluences above 1.2×10^{18} ions/cm^2 at 90keV, the FWHM plateaus where the concentration of C is high enough to form carbon clusters. The area under the FTIR peak may similarly be used, and the saturation of C:Si is reported as 5×10^{17} ions/cm^2 at 65 keV [47]. Compounds of Si, O, H and C are observed in C:Si experiments, and are expected in the current work. The characteristic IR bands have been observed at: 1100 cm^{-1} interstitial carbon, 1100 cm^{-1} SiO_2, 670 cm^{-1} Si—C stretch or SiH_n wagging, 1000 cm^{-1} CH_n wagging, 1275 cm^{-1} C—O, 1450 cm^{-1}, C—H_2, and 1590 cm^{-1} C=C [55].

Raman spectroscopy is used to examine Si—Si and C—C bonds in C:Si materials, the C—C band in Raman spectra indicates the formation of carbon clusters, and is interpreted to mean that implanted C^+ is not fully incorporated into SiC [56]. There are two C—C bands commonly discussed in Raman spectra: the disordered *D*-band (~1350 cm^{-1}) and graphitic *G*-band (1580 to 1600 cm^{-1}) [83]. The graphitic band indicates carbon sp^2 bonding, as is seen in graphite, the disordered band is related to contributions from sp^2 and sp^3 carbon bonds that are less organized. These bands are observed in as-implanted and in annealed C:Si for over-stoichiometric fluences [67], [80]. Raman spectra are also sensitive to crystalline Si (520 cm^{-1}, 2^{nd} order 970 cm^{-1}), amorphous Si (broad peak 100-600 cm^{-1}), amorphous carbon (770-780 cm^{-1}), and Si—H (2800 cm^{-1}) [43], [45], [47], [55], [56], [67], [80]. The probability of

observing a Si—C band in Raman spectra is low, however it has been reported in C:Si literature: ß-SiC at 817 cm^{-1}, SiC at 668 cm^{-1}, 4H-SiC at 615 cm^{-1}, and ß-SiC at 800 cm^{-1} [45], [48], [50].

The crystal structure of C:Si before and after annealing is investigated by XRD [47], [84]. This technique provides information on the crystal structure and orientation of SiC precipitates. The XRD results of previous studies show that the implantation process results in an amorphous layer of Si and C, which crystallizes after annealing. In most cases, the Si and SiC are polycrystalline, having multiple orientations, and the SiC has cubic structure (ß-SiC) [45], [47], [49], [69], [71], [84]. However, heating the target is shown to promote the growth of ß-SiC precipitates that have the same orientation as the target [46], [67].

The structure of C:Si materials is also investigated using TEM techniques, which provides direct observation of buried structures, and regions of different chemical composition. The scanning TEM micrographs in the literature are consistent with each other, across varied implant energies (25 keV to 300 keV), and fluences (2.5×10^{16} ions/cm^2 to 1×10^{18} ions/cm^2)[67], [70], [71], [80]. As-implanted samples show amorphous Si and C in the implanted regions, where the implanted carbon follows predictions made by SRIM calculations [49], [67], [71], [80]. Post-implant annealing has been shown to induce crystallization of the Si and C, and three distinct regions were reported: an amorphous silicon (a-Si) layer, a crystallized SiC layer, and a re-crystallized Si region on the bulk single-crystal substrate; [43], [46], [49], [67], [69]–[71], [80], [84]. The size of the crystallites and depth of these regions is depends on implant energy and target temperature, as would be expected where the final concentration of the ions depends on the implant energy and the target density (which is temperature dependent)[65]. High temperature (HT) implantation treatment produces samples similar to the samples implanted without external heating (called ambient temperature, abbreviated AT). Samples that have been

heated to >400 °C during implantation are observed to have sharper interfaces – a more box shaped distribution of SiC in the target [44]. The layers observed in HT samples are: a Si layer near the surface, with a buried ß-SiC layer with the same orientation as the substrate, and a damaged Si layer beneath [46], [67].

Luminescence measurements are the most significant characteristic for materials application in photonics research. Early reports of ion implanted SiC demonstrate yellow cathodoluminescence, and green luminescence from ion implanted SiC *p-n* junctions [31], [41]. The luminescence of the C:Si based materials is reported with blue to IR emission. Photoluminescence (PL) measurements of annealed C:Si can be modeled with Gaussian curves that have peaks at ~390 nm (3.2 eV), 445 nm (2.8 eV), 480 nm (2.6 eV), and 560 nm (2.2 eV) [68], [72]–[74]. The peak at 390 nm is unidentified [68], [73]. The PL peak at 445 nm and 480 nm are associated with quantum confinement in ß-SiC, with energies larger than the band gap of bulk ß-SiC (2.2 eV) [68], [72]–[74]. TEM images of the materials show porous structure with nanoscale SiC precipitates on the scale of 2-5 nm in the case of the 445 nm PL band, and 2-10 nm sized particles for the C:Si with 480 nm emission [68], [72]. The emission energy decreases with increasing particle size, which is expected in quantum confinement effects, further discussed in section 2.2.2.1. These studies of PL in C:Si include ion implantation of C^+ into p-Si, which was generated by etching of crystalline Si [72]. The PL of the p-Si without C+ implantation is reported as 560 nm, and this was used to explain the emission at that same energy in the C:Si materials [72].

Electroluminescence measurements show similar spectra, with peaks at 560 nm (2.2 eV), and 450 nm (2.8 eV) that are attributed to p-SiC [74]. The PL from PIII treatment of p-Si yields luminescence at 603 nm (2.1 eV) seen in the untreated p-Si, and 454 nm (2.7 eV) seen after ion

implantation. Annealing C:Si above 800 °C has been shown to enhance luminescence, by facilitating the growth of crystalline phase material, with long range period lattice structure, which has improved carrier mobility; or presents nanoscale crystalline precipitates that present emission from quantum confinement effects [41], [66], [71], [72]. Annealing temperatures above 1250 ˚C the incorporation of O and H into the SiC compounds in the material contribute additional luminescence bands in the visible region of the spectrum [52], [85]. This annealing temperature is slightly higher than the observed optimal temperature for SiC formation, and is also above the range of operation of the furnace used in the current work [71].

Silicon sub-oxide compounds are seen to contribute to the PL of C:Si at 430 nm (2.9 eV), with emission from p-SiC at 500 nm (2.5 eV) [55]. Infrared emission is also observed at 1130 nm (1.1 eV) from nano-patterned Si, and 1278 nm (0.97 eV) from carbon clusters which disappear after annealing above 200 ˚C [86]. Baraban *et al.* measured EL using an "electrolyte-insulator-semiconductor" system, using SiO_2 implanted with Si^+ and C^+ [87]. The reported EL emission is from SiO_2 defects at 653 nm (1.9 eV) and 539 nm (2.3eV), and from a Si—O complex luminescent center at 459 nm (2.7 eV) and 288 nm (4.3 eV). Emission from SiC is seen in the same EL measurements at 387 nm (3.2 eV), [87]. In the present EL measurements, luminescence from p-Si, p-SiC and sub-oxide complexes are expected.

The EL measurements reported in the literature were collected from a variety of device architectures, including *p-n* junction, Schottky diodes and other methods [74], [86]–[88]. Ghezzo *et al.* report a *p-n* junction diode fabricated from N^+ ion implanted α-SiC that have turn-on voltage $V_{on} \approx 1.5$ V [88]. Similarly, Rotem *et al.* produce *p-n* junction devices with $V_{on} \approx 1$ V and no reverse breakdown up to -5 V, using C:Si [86]. Li *et al*. present a Schottky diode with $V_{on} < 5$ V and no reverse breakdown up to -40 V [74]. Previous investigations of C:Si materials

for photonic applications include relatively few studies that produce or test electronic devices, such as the ones presented in this thesis.

1.4. Overview

Silicon photonics research aims to improve the processing speed and chip communication quality using optical interconnects in multi-core processors. The aim is to introduce optoelectronic materials that can be fabricated using existing infrastructure in semiconductor manufacturing facilities. Ion implantation and thermal annealing are common methods used in the semiconductor industry. The work presented in this thesis uses high fluence, low energy ion implantation followed by thermal annealing to synthesize C:Si. The material is studied using a range of characterization techniques (Raman, FTIR, XRD, TEM, EELS). The XRD, TEM and EELS measurements were carried out at facilities external to the University of Saskatchewan, and the measurement parameters were defined by the author. Fabricating LEDs and testing the *I-V* characteristics and EL spectra of the devices demonstrates the use of the material for electronic applications. There are four major goals for the research:

- Synthesis and materials characterization of C:Si,
- Investigate C:Si produced at low-energy for LED applications as a demonstration for photonic devices,
- Determine luminescence mechanisms,
- Investigate the effect of specific treatment parameters: fluence and *in situ* annealing on luminescence spectra.

The thesis is laid out as follows: Chapter 1 outlines the motivation and objectives of this project. Chapter 2 discusses the basic principles underlying the research done for this work: Schottky diodes and luminescence mechanisms. Chapter 3 briefly describes the characterization methods used for the materials and devices in this study. Chapter 4 presents and discusses the results of the experiments. Conclusions and future work are discussed in Chapter 5.

The results and analysis of the materials characterization and device fabrication that are discussed in this thesis are published: S. Purdy, A. P. Knights, M. P. Bradley, G-S. Chang, in the *Institute of Electrical and Electronics Engineers Transactions on Electron Devices*, "Light-Emitting Diodes Fabricated From Carbon Ions Implanted Into p-Type Silicon," **62**, 3, p.914-918 (2015) [89]. The author's contribution to this paper includes materials synthesis (simulation of processing treatment, thermal annealing); diode fabrication; data collection for FTIR, and Raman spectra, diode *I-V* curves, and EL spectra; data analysis and interpretation for all techniques; lead authorship on the paper, and leadership in the overall project design of all experiments.

Further investigation of the C:Si materials was conducted at the Canadian Light Source – Spherical Grating Monochomator (SGM) and Resonant Elastic and Inelastic X-Ray Scattering (REIXS) beam lines. X-Ray absorption spectroscopy measurements at the carbon *K*-edge, silicon *K*-edge, and Si $L_{2,3}$-edge, as well as X-Ray emission spectroscopy measurements at the Si $L_{2,3}$-edge were collected. The synchrotron techniques are used to more clearly examine the chemical bond environment of the C:Si materials. Measurement of the density of states at the band-edges can provide direct evidence of band-tails and defect states. This work is drafted for submission to the *Journal of Applied Physics* in December, 2015: S. Purdy, A. Hunt, P. Bazylewski, R. Bauer, G-S. Chang, M. P. Bradley, A. Knights, "A comprehensive spectroscopic investigation of SiC nanoparticles prepared by low energy plasma ion implantation." The author's contribution to this

paper includes the materials synthesis; sample preparation; data collection, analysis and interpretation; authorship of the paper; and leadership and design of the project. The work for this paper is based on the successful CLS beam-time proposal: "XANES[2] and XEOL[3] of electroluminescent diode material fabricated by carbon ion implantation and annealing in p-type Si," S. Purdy, Jan. 2013 (accepted Sep. 2013).

[2] X-Ray absorption near edge spectroscopy (XANES)

[3] X-Ray excited optical luminescence (XEOL)

CHAPTER 2

LIGHT-EMITTING DIODES

The implementation of Si materials for photonic applications enables the use of currently existing processing technologies that rely on Si, with the added benefit of the use of SiO_2 light conducting pathways that can be used to transmit information. In a functional photonic device, information must be transmitted from the part of the device that performs the calculations, to the communication layer and other parts of the device. Light-emitting diodes present a solution for the transmission aspect of this application.

2.1. Schottky Diodes

The construction of test LEDs is a low-cost, simple approach to designing materials for photonic applications. The diode used in the present work has a simple metal-semiconductor (Schottky) architecture, consisting of two metal contacts on the C:Si material as a sandwich. The Al contact serves as an Ohmic contact, where charge carrier injection is driven by externally

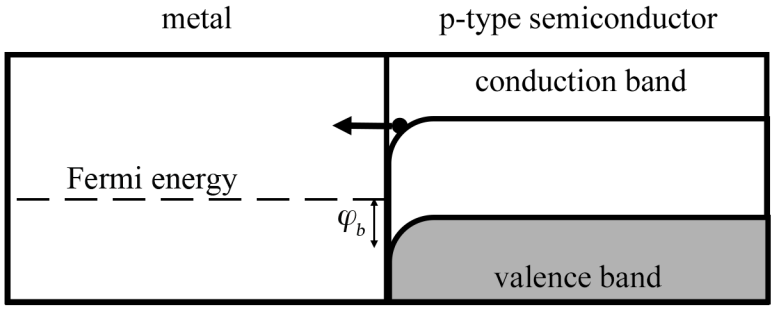

Figure 2.1 Schematic of a Schottky barrier: interface of metal and semiconductor. results in "band bending" where electrons in the semiconductor that are thermally excited in the conduction band of the semiconductor can tunnel into the available (lower energy) states in the metal conduction band until equilibrium is reached. A forward bias applied electric field increased the number of available states in the metal conduction band, allowing current to flow. The barrier height, φ_b is indicated.

applied voltage, and current increases linearly with applied potential. The Au contact is a metal-semiconductor contact with the C:Si. This method is shown to be successful in producing Schottky diodes from ion-implanted silicon, even when p-type Si is used. The application of the metal contact on the p-type Si results in electron diffusion (before the presentation of an applied potential on the device). The electrons are attracted to the p-type dopant atoms, and contribute to the buildup of an electron deficient region on the metallic side of the interface (positively charged), and an electron-rich region on the semiconductor side of the interface (negatively charged) in a net-neutral device. At equilibrium, this charge distribution generates an electric field that opposes further electron migration [90]–[94].

In the case where voltage is applied across the diode in a forward bias configuration, carriers are thermally excited from the conduction band of the semiconductor into the metal, shown in Figure 2.1 [95]. Under reverse breakdown conditions the Fermi energy of the metal is equal to or larger than the energy of the conduction band ($E_F \geq E_C$) and there are no available states to allow current flow. These contacts, of course, come with a plethora of interface effects

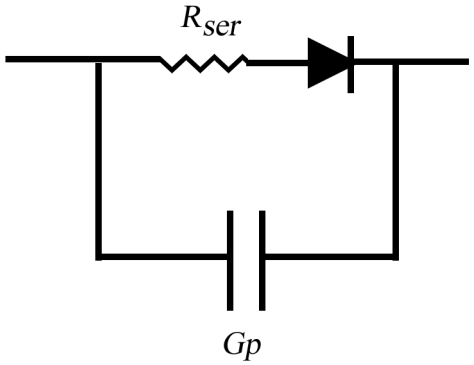

Figure 2.2 Schematic of an equivalent circuit for the Shockley equation consisting of an ideal diode in series with a resistor that represents the real resistance of the material, and a capacitor representing the parallel metal plates of the physical diode architecture.

and impurities that impede current flow, therefore contact firing to reduce physical defects at the contact is necessary [91], [96]. The surface oxide layer of the C:Si material is not etched away since oxygen defects and SiO_2/Si interfaces are known to contribute to luminescence [52], [97]. The Au contact is also made thin, to be semi-transparent to allow for light transmission and measurement of the EL spectrum [74], [91], [98].

The turn-on voltage (V_{on}) is determined using a piece-wise-linear model of the diode, where linear fit is applied to the "off" and "on" regions of the *I-V* curve, and the value of the voltage at the intersection of these two lines is taken as V_{on} [91].

A model for the current through the diode is constructed of an ideal diode, a series resistor and a parallel capacitor shown in Figure 2.2 [96], [99], [100]. The Shockley equation for current through an ideal diode is written as:

$$I = I_{sat}\left[\exp\left(\frac{q}{nkT}V_d\right) - 1\right] + G_p V_d \tag{2.1}$$

The current, I, is given by the voltage drop across the diode, V_d, device temperature, T, and capacitance G_p. The remaining constants in Equation 2.1: I_{sat} is the saturation current, q is the

charge of the electron, n is the ideality factor (how closely the diode resembles an ideal diode), and k is the Boltzmann constant.

The parallel capacitance in this idealized circuit is negligible when the barrier height φ_b of the Schottky contact is large (0.830 eV).

$$I = I_{sat}\left[\exp\left(\frac{q}{nkT}V_d\right) - 1\right] \tag{2.2}$$

In the real system, the diode has a resistance to current flow in forward bias mode that is modeled as a resistor in series, so the voltage drop across the device is that of the applied potential, V, and the drop due to the series resistance, R_{ser}:

$$V_d = V - IR_{ser} \tag{2.3}$$

The inverse slope of the *I-V* curve gives the order of magnitude of the series resistance:

$$R_{ser} = \frac{dV_d}{dI} \tag{2.4}$$

One method of modeling diodes is to set a value for R_{ser}, informed by Equation 2.4, and generate a model using the Shockley Equation 2.1, using the line of best fit in the forward-bias region to extract the ideality factor, n, and the saturation current, I_{sat}. The model is compared to the data, and the process is reiterated to achieve the best agreement.

The Shockley equation for a non-ideal diode, with a series resistance, and small barrier height, is also expressed as a combination of Equations 2.1 and 2.3 [99]:

$$I = I_{sat}\left[\exp\left[\frac{q}{nkT}(V - IR_{ser})\right] - 1\right] \tag{2.5}$$

This equation is also expressed as

$$J = a[exp(bV) - 1\,] \tag{2.6}$$

where R_{ser} is taken to be small, and I is normalized by the diode area to give the current density, J; a and b are fitting parameters. This equation is used in Origin 8.5 to calculate an exponential line of best fit of the forward-bias J-V curve where:

$$a = I_{sat} \tag{2.7}$$

$$b = \frac{q}{nkT} \tag{2.8}$$

to determine n, Equation 2.8 is rearranged as.

$$n = \frac{q}{bkT} \tag{2.9}$$

The saturation current is also written as

$$I_{sat} = AA^{*}T^{2}\exp\left(\frac{\varphi_b}{kT}\right) \tag{2.10}$$

where A is the area of the diode contact, A^{*} is Richardson's constant 32 A/cm^{2}K^2 [92], [101], and φ_b is the barrier height. The barrier height is defined as the difference between the Fermi energy, E_F, in the metal and E_C, the energy of the conduction band in the semiconductor. Note that current and current density (J) are interchangeable, since Equation 2.10 includes an area factor. Rearranging Equation 2.10:

$$\varphi_b = \log[I_{sat}(AA^{*}T^{2})^{-1}]kT \tag{2.11}$$

This is the typical method for modeling devices, especially for diodes with low ideality factors not much larger than n = 1. For high ideality factors, other methods have been developed, using forward-bias I-V measurements [99]. These methods include using the first derivative of the I-V data plotted against the current. In the work reported in this thesis, the measurement intervals are incompatible with these methods: the I-V measurements were done before calculation of device area, the I values were taken at regular intervals, not necessarily regular intervals of J, and the

derivative of the *J-V* data is skewed. Future work on ion-implanted diodes should be designed for use of these methods for high-ideality factor cases.

The measurements reported in Chapter 4 also include the reverse-bias *I-V* curve, and the current in the reverse bias region is equivalent to the saturation current $I = I_{sat}$. The barrier height may be calculated from the reverse-bias measurements and compared to the result for the forward bias results.

2.2. Electroluminescence and Emission Mechanisms

The LEDs fabricated for this work are used to investigate the performance of the C:Si material for photonic applications. The ability to tune the color of the light-emission, especially in the visible region is most desirable [102], [103]. The electrical contacts of the diode are used to inject charge carriers into the sample for device operation, the sample charge remains neutral which is to say that the same number of electrons and holes are injected. The injection of charge carriers is dependent on the quality of the electrical contact, Therefore the diodes are fired after the metal contacts are applied [91]. Within the diode material the charge carriers lose energy in radiative and non-radiative processes which are discussed in this chapter [104].

The low energy of the implantation process is expected to produce a thin film of carbon-rich silicon. The dose of carbon is not enough to saturate the implanted region, therefore SiC formation is expected to be complete, and no carbon clusters should remain after annealing. The implanted region is expected to be composed of amorphous and porous SiC and Si [73].

It is worth mentioning that in some cases researchers use photons from an external light source to drive luminescence in materials that are under study for photonic application [59], [68], [75], [105]–[110]. A light source with energy above the optical gap of the material is used to

excite the electrons in the material for photon-induced luminescence [104]. The PL and EL spectra are reported to be similar or identical [74], [111], [112]. The commonly cited luminescence mechanisms are reviewed below. Literature to date presents EL and PL in the visible region for C:Si, and attributes the luminescence bands to quantum confinement in nanocrystalline (nc-Si), porous and amorphous Si and SiC [52], [68], [72], [73], [113].

2.2.1. Non-radiative Recombination

The luminescence of the C:Si LEDs is generated by the radiative decay of charge carriers in the diode material. These mechanisms compete with non-radiative decay processes such as Auger recombination and phonon processes. In Auger recombination, an electron combines with a hole without photon emission, the energy lost by the electron is absorbed by another electron, which then has a higher energy than its initial state [104], [114]. Another non-radiative decay process is described as electron-phonon interactions. Excitation of electrons results in a change in electron momentum, which is then lost as heat [27]. The Shockley-Read-Hall effect explains that if an impurity is introduced to the crystal lattice, there can be a corresponding defect state, such as a lattice impurity (substitutional or interstitial), or an unsaturated valence state: “dangling bond,” within the band gap of the material, and this state serves as a center for inelastic electron-phonon interactions [115]. This process is observed in indirect band gap materials like Si and SiC, and it limits the efficiency of light emission from devices made using bulk crystals.

2.2.2. Luminescence in Amorphous Silicon and Silicon Alloys

One of the mechanisms that is cited as a source for luminescence in C:Si materials is amorphous Si and SiC, which is compiled and reviewed in *Properties of Amorphous Silicon and its Alloys* [116]; this section relies heavily on these review articles unless otherwise cited [72], [73], [113]. The difference between the a-Si and p-Si materials is related to density and structure. For a-Si, the material is disordered, but closely packed, and although Si is likely to be bonded to other Si atoms, it may not necessarily have long-range crystalline ordered components. The luminescence in a-Si materials is described as having two bands: 0.9 eV "*D*-band" and 1.3 to 1.4 eV "*M*-band" at 10 K (1.1 eV at room temperature). The *D*-band is associated with recombination between an electron energy band and a defect state. This recombination process appears to be enhanced by doping, and is associated with the quantity of dangling bonds in the material. An abundance of dangling bonds results in quenching of PL (and likely EL). For example: doping a-Si with boron reduces the contribution of the *M*-band, and enhances the *D*-band luminescence. The *M*-band is consistent with recombination in band tails that would be analogous to that in doped materials. The band tails are regions of the conduction and valence bands that extend into the band gap due to a high density of defect states, a visualization of this is shown in **Error! Reference source not found.**.

2.2.2.1. Quantum Confinement

Additional work on C:Si reports emission from direct band-band recombination with quantum confinement [117], [118].The confinement effect is cited as the source of luminescence

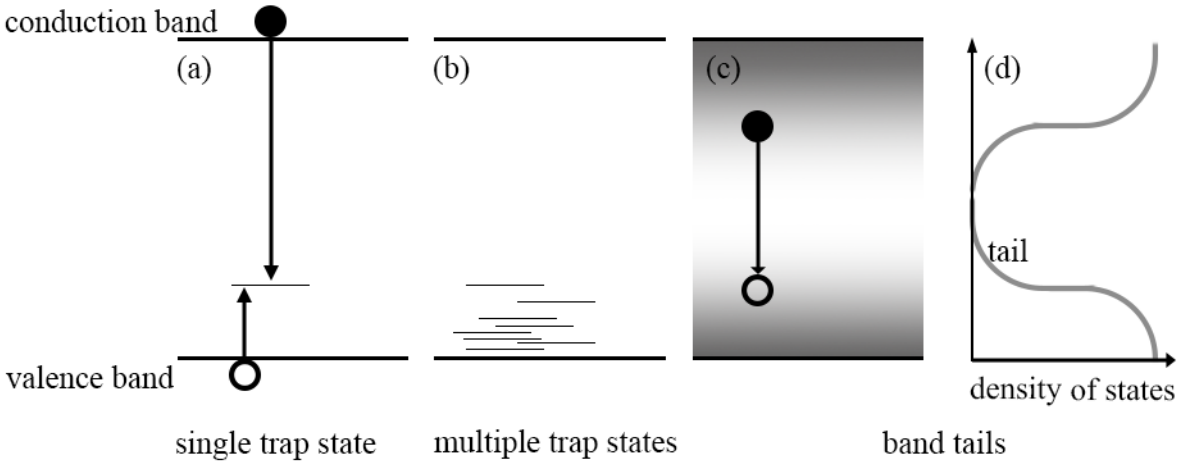

Figure 2.3 (a) Trap states are caused by a crystal impurity such as a crystal defect or a dopant atom. A trap such as this can facilitate electron-hole recombination. (b) It is possible for there to be multiple impurities and their associated trap states. (c) In some cases there may be enough trap states, closely-packed together, and they are indistinguishable, this is referred to as a "band tail" as illustrated in the density of states (d) [119].

in p-Si, which is made up of nanoscale crystalline Si (c-Si) clusters or crystallites of Si[120]. The principles of quantum mechanics apply to this system, and are used here in a simplified form to conceptualize the emission from materials with quantum confinement. The basic concepts of quantum confinement are frequently discussed, for a discussion on quantum mechanics see R. Dick[121], and for quantum confinement in semiconductors see C. Kittel [122]. Within the crystallites in a porous material, an excited electron is close enough in real space to a hole that the Coulomb force is relevant. This bound exciton is described as a Rydberg atom made of two particles of opposite charge, the (Bohr) radius, r_B, is:

$$r_B = \frac{\hbar^2 \mathcal{E}}{e^2}\left(\frac{1}{m_h} + \frac{1}{m_e}\right) \tag{2.12}$$

The exciton Bohr radius for silicon is 4.3 nm, and for β-SiC is 2.7 nm [123], [124]. This is a Frenkel type exciton where an electron is excited, and tightly bound by Coulomb force to the positive ion; any atom in the material may be excited in this way, and excited electrons may

excite neighboring atoms and the pair of excited electron and positive ion (electron-hole) pairs has mobility as a particle referred to as an "exciton" [27]. By contrast, there exist weakly bound excitons where the excited electron is separated by several primitive cell widths from the hole state on a fixed ion; this is a Wannier-Mott exciton [27].

A small particle in colloidal solution or embedded in a solid may be treated as having a defined potential well with defined boundaries. If the particle size of a cluster (diameter, $D = 2r$, radius) is less than the Bohr radius for the material ($D < r_B$) then the particle is analogous to a "particle in a box." This confined particle has an effective mass, m^*, depending on the mass of the charge carriers in the conduction (m_c) and valence (m_v) bands:

$$\frac{1}{m^*} = \frac{1}{m_c} + \frac{1}{m_v}. \tag{2.13}$$

The three-dimensional (3-D), time-independent Schrödinger equation is stated as

$$E_{ex}\psi(\boldsymbol{x}) = -\frac{\hbar^2}{2m^*}\Delta\psi(\boldsymbol{x}). \tag{2.14}$$

The potential energy of the excited state, E_{ex}, is an eigenvalue of the 3-D wave function $\psi(\boldsymbol{x})$, and $\hbar$ is Planck's constant divided by 2π. The wave function for a particle confined in a sphere with radius, r, is

$$\psi(\boldsymbol{x}) = \sqrt{\frac{2^3}{L_1 L_2 L_3}}\sin(k_{n_x}x)\sin\left(k_{n_y}y\right)\sin(k_{n_z}z), \tag{2.15}$$

where k_{n_i} are the wavenumbers describing the energy state in direction $i = x, y, z,$ and $n \geq 0$ are integers. The energy eigenvalues of the excited state are

$$E_{ex} = \frac{\hbar^2\pi^2}{2m^*}\left(\frac{n_x^2}{L_1^2} + \frac{n_y^2}{L_2^2} + \frac{n_z^2}{L_3^2}\right). \tag{2.16}$$

This is the energy contribution of the confined charge carrier, for example an exciton in a nanoscale particle. The important point about this basic derivation is that the energy of the

exciton is proportional to the inverse-square of the dimension of the nanoparticle. This L^{-2} relation has been used to calculate the energy gap of Si nanostructures [123], [125], [126].

One further step for dielectric materials is to account for the shielding generated by the other electrons in the material that repel the excited electron by Coulomb force. The electron is treated as a new charge being added to the collection of charges in the quantum dot, and the charging energy associated with this action is

$$U = \frac{e^2}{4\pi\varepsilon_0\varepsilon r}, \tag{2.17}$$

where e is the charge of the electron, ε_0 is the permittivity of free space, and ε is the relative permittivity of the material in a spherical quantum dot with radius r [122]. The total exciton energy, E, that includes the energy of the band gap, E_g is combined with $E_{ex}(n=1)$ and U [127]–[129]:

$$E = E_g + E_{ex} - U, \tag{2.18}$$

$$E = E_g + \frac{\hbar^2\pi^2}{2m^*r^2} - \frac{e^2}{4\pi\varepsilon_0\varepsilon r}. \tag{2.19}$$

This model for total exciton energy has been successfully applied to quantum dots made from β-SiC, with particle diameter d = 3.9 nm having a corresponding exciton total energy E = 2.7 eV (460 nm), and d = 8.8 nm showing E = 2.3 eV (540 nm) [128].

This simplified presentation of the principles of quantum confinement does not include things like band anisotropy or non-spherical dimensions that appear in physical systems. It serves to illustrate that a particle with fixed momentum (i.e. confined in space) has discrete allowed energies that depend on the dimension of the spatial confinement, and the total exciton energies must be larger than the band gap of the bulk material. Luminescence attributed to quantum

confinement effects are reported in semiconductor materials both in colloidal solution and in solid state [127], [129], [130].

2.2.2.2. Porous Silicon

Porous silicon is reported to have PL and EL between 700 and 850 nm, which is attributed to quantum confinement by both measurements and modeled systems [68], [131]–[133]. In p-Si, the crystallites are arranged in an array, and have increased surface area that may be passivated by hydrogen, oxygen, carbon or other impurities. The luminescence from p-Si is vulnerable to degradation and aging as the surface passivation changes over time. The degradation is enhanced by device use, where electrical or luminescent excitation results in Joule heating of the material and encourages changes to the surface chemistry of the p-Si [131].

In the case of p-Si, the PL is comparable to that of Si nanoparticles. For example, samples of p-Si grown by etching followed by implantation of carbon ions produce PL where the peak measured for un-implanted p-Si is observed from the implanted sample alongside a peak attributed to quantum confined electron-hole recombination in SiC [52]. Similar experiments including anodization of Si and SiC, demonstrate the same result: the luminescence of the p-Si is seen to contribute to the luminescence of the modified SiC [68], [72].

2.2.2.3. Amorphous Si Alloys

Different alloys of Si are seen to have different luminescent spectra. Amorphous Si with oxygen (a-SiO_x, $x < 2$) presents a luminescent band between 1.8 and 9 eV for $0 < x < 2$. The

oxygen acts to passivate the dangling bonds in the a-Si, and reduces the *D*-band contribution in PL measurements [116].

Amorphous sub-stoichiometric SiC (a-$Si_{(1-y)}C_y$) films produce PL spectra with the peak energy dependent on carbon content and the synthesis method. The PL peak is reported at 1.3 eV to 2.0 eV at 77 K for stoichiometric concentrations of carbon up to y = 0.87 [116]. Photoluminescence from a-$Si_{(1-y)}C_y$ materials sometimes included the a-Si "*M*-band." Studies on C:Si synthesis of a-SiC films report PL and EL near 480 nm (2.5-2.6 eV) [68], [74]. The mechanism in such cases is more complex; the carbon concentration does not necessarily affect the band gap at low concentrations ($y < 0.5$), and the luminescence may be attributed to planar (sp^2) "graphitic" carbon states [113], [116].

Radiative decay in C:Si materials may happen via a variety of channels, which are dependent on the physical composition of the wafers. The ion implantation process leaves amorphous and porous material, and the annealing process helps to agglomerate the Si, C and O atoms into clusters or crystalline inclusions. Luminescence results reported in the literature are frequently attributed to p-Si, and Si alloys with O and C. Over-stoichiometric C:Si samples may also produce luminescence from carbon clusters.

In the work presented in this thesis, the theory outlined in this chapter is used to analyze the LEDs fabricated from C:Si. The *I-V* behavior of the LEDs are be modeled using the Shockley equation, and the series resistance, ideality factor, and barrier height are determined. The EL may also be analyzed by Gaussian fitting of the spectra, and the possible luminescence mechanisms are a-Si, a-SiC, p-Si, p-SiC, SiC, and carbon sp^2 states, based on previous work discussed in this and the previous chapter.

CHAPTER 3

SYNTHESIS AND CHARACTERIZATION METHODS

For this study, C:Si samples are synthesized using ion beam treatment of boron doped (*p*-type) silicon wafers, with *in situ* and post-implant annealing treatments. This chapter summarizes the techniques and methods used in the synthesis and characterization of the C:Si material and LEDs. Several characterization methods are used to identify the chemical and physical properties of the C:Si. Raman and FTIR spectroscopy are used to identify the chemical composition of the implanted carbon, specifically Si—C and C—C bonds. X-ray diffraction is used examine the physical structure of the C:Si, looking for the possible formation of crystalline inclusions. Scanning TEM is used to complete the picture of the physical structure of the C:Si looking for amorphous and porous structures that are common in materials treated with ion implantation. In tandem with scanning TEM, EELS is used to determine the distribution of carbon by depth into the Si substrate. In this way, the most basic properties of the C:Si material are examined.

LEDs are fabricated using physical vapor deposition (PVD) of metal contacts onto the front and back faces of the C:Si wafers to create large-area diodes. Contact firing after deposition improves the quality of the interface between the metal coating and the C:Si wafer [91]. A water-cooled test-bed is used as a platform for *I-V* and EL measurements. The test-bed also allows for collection of the emission spectra of the diodes [91].

3.1. Ion Implantation

Ion implantation is a widely used technique in semiconductor research and manufacturing for doping and modifying materials, for CMOS and silicon-on-insulator (SOI) applications [24], [63], [134]–[138]. Using this technique for experimental materials synthesis is appealing because it is scalable for mass production and the facilities already exist on an industrial scale [63], [138]. The cost of integrating a new technology, like the proposed C:Si LEDs is reduced by using techniques familiar to the industry. Ion implantation techniques employ electric or magnetic fields to accelerate ionized material towards a target with sufficient energy to be embedded into the target. The depth and distribution of the ions into the target depends on the ion implantation energy, the mass of the implanted ion, and the density and composition of the target [64], [139]. An overview of ion implantation theory and techniques is given in this section. For more in depth presentations of ion implantation there are a number of useful sources for fabrication engineering (including discussion of diffusion and annealing) [63], ion implantation in general [64], [137], and plasma processing [138].

One of the goals for this project is to lead into using PIII to prototype devices for fabrication in larger scale facilities. The Bradley lab plasma reactor, with implantation energy rated to -20 kV, is used to inform the design decisions for the IBS treatments [140].

During the ion implantation process, ions penetrate the surface of a target, where the average depth travelled by the ions is the projected range (R_p). The implanted ions lose energy and come to rest in the target due to nuclear and electronic interactions, which depend on the nature of the target and the implanted ion. The energy loss per unit length (the work done by the ion to move through the sample) in the target is referred to as the "stopping power" (S)

$$S = S_e + S_n. \tag{3.1}$$

The stopping power has contributions from the electronic (S_e) and nuclear (S_n) interactions with the implanted ions [63].

The electrons in the target material are described as a viscous fluid that exerts a drag force, F_{drag}, on the implanted ions. This force is assumed to be proportional to the ion velocity, v_{ion}, with is associate kinetic energy, E_{ion}.

$$F_{drag} \propto v_{ion} \propto \sqrt{E_{ion}}. \tag{3.2}$$

The stopping power of the material only due to the electron-ion interaction is a depth (x) dependent gradient.

$$S_e = \frac{dE_{ion}}{dx} = k_e\sqrt{E_{ion}}. \tag{3.3}$$

The proportionality constant (k_e) depends on the charge number (Z), and the atomic masses (M) of the implanted ion and target.

$$k_e \propto \sqrt{\frac{Z_{ion}Z_{target}}{M_{ion}^3 M_{target}}}\frac{\left(M_{ion}+M_{target}\right)^{3/2}}{\left(Z_{ion}^{2/3}+Z_{target}^{2/3}\right)}. \tag{3.4}$$

This treatment breaks down at very high implantation energies, where the stopping power reaches a maximum and then decreases for higher implantation energy [63].

In addition to the stopping power of the electrons, the implanted ions undergo inelastic scattering by the nuclei in the target and travel randomized paths. The implanted ion path length is the projected range (R_p), and the "longitudinal" straggle (σ) is the standard deviation of R_p, as shown in Figure 3.1. The random scattering also induces a lateral straggle (Ω), the deviation of the ion position from the axis of the incident ion velocity. In addition to S_e, the projected range is dependent on the stopping power of the nuclei in the target, i.e. the energy lost during inelastic collisions with other nuclei in the target. For low implantation energy, on the scale of the energy

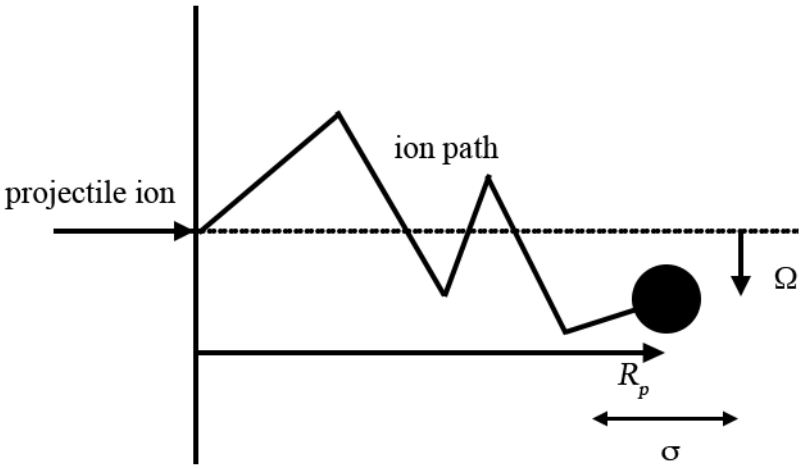

Figure 3.1 Illustration of ion path, projected range (R_p), longitudinal straggle (σ) and lateral straggle (Ω), which are simulated by SRIM software.

used for the implantation treatments discussed in this thesis, S_n increases with implantation energy. As the implantation energy increases, S_n increases to a maximum value, S_0 at energy E_0.

$$S_0 = 2.8\times10^{-15}\text{eV}\cdot\text{cm}^2\frac{Z_{ion}Z_{target}}{\sqrt{Z_{ion}^{2/3}+Z_{target}^{2/3}}}\frac{M_{ion}}{M_{ion}+M_{target}}. \tag{3.5}$$

At low ion implantation energies, $S_n > S_e$, and the ion path in the target is determined by the scattering from target nuclei, which can be predicted using Monte Carlo simulations. A Gaussian distribution describes the random nature of the ion paths in the target [63], [64].

The projected range is the average displacement of the implanted ions in the depth of the target, and using equation 3.3:

$$R_p = \int_0^{R_p} dx = \int_{E_0}^{0}\frac{dE_{ion}}{dE_{ion}/dx} = \int_{E_0}^{0}\frac{dE_{ion}}{(S_e+S_n)}, \tag{3.6}$$

and the standard deviation of R_p within the target is

$$\sigma \cong \frac{2}{3}R_p\left(\frac{\sqrt{M_{ion}M_{target}}}{M_{ion}+M_{target}}\right). \tag{3.7}$$

This brief overview of ion implantation parameters is presented with the current treatment in mind – that is to say, low energy implantation. The use of higher energies for implantation presents complications that are beyond the scope of this thesis, but are discussed in more detail in sources like Ziegler's coverage of ion implantation and Campbell's book on micro- and nanoscale semiconductor fabrication [63], [64].

The stopping power, projected range, longitudinal and lateral straggle, are calculated by SRIM software discussed in further detail in Section 3.1.2. The "quick range" table for carbon ions implanted into silicon at 20 kV is presented in Figure 3.2 and shows the calculated estimates for the parameters discussed in this section. The simulations are used to inform decisions on the implantation parameters (energy and fluence).

3.1.1. Implantation Effects and Considerations

The process of ion implantation results in a variety of physical and chemical modifications of the target, as shown in Figure 3.3. Implanted ions can break apart bonds in the target material, which may or may not re-combine or be rearranged. The damage to a target lattice is to be mitigated by post-implant and *in situ* annealing [63], discussed further in Section 3.2. Some broken bonds may combine with nearby hydrogen or oxygen impurities. Re-formed bonds may not satisfy available atomic valence states, resulting in a "dangling" bond. Native atoms of the target may be scattered or sputtered, leaving pores and vacancies in the target crystal lattice. The implanted ions may replace some of the native atoms in the lattice structure, remaining as a substitutional impurity. In the case of a relatively high dose of ions into the target, the implanted ions may bond with each other and form an embedded cluster. This has the added

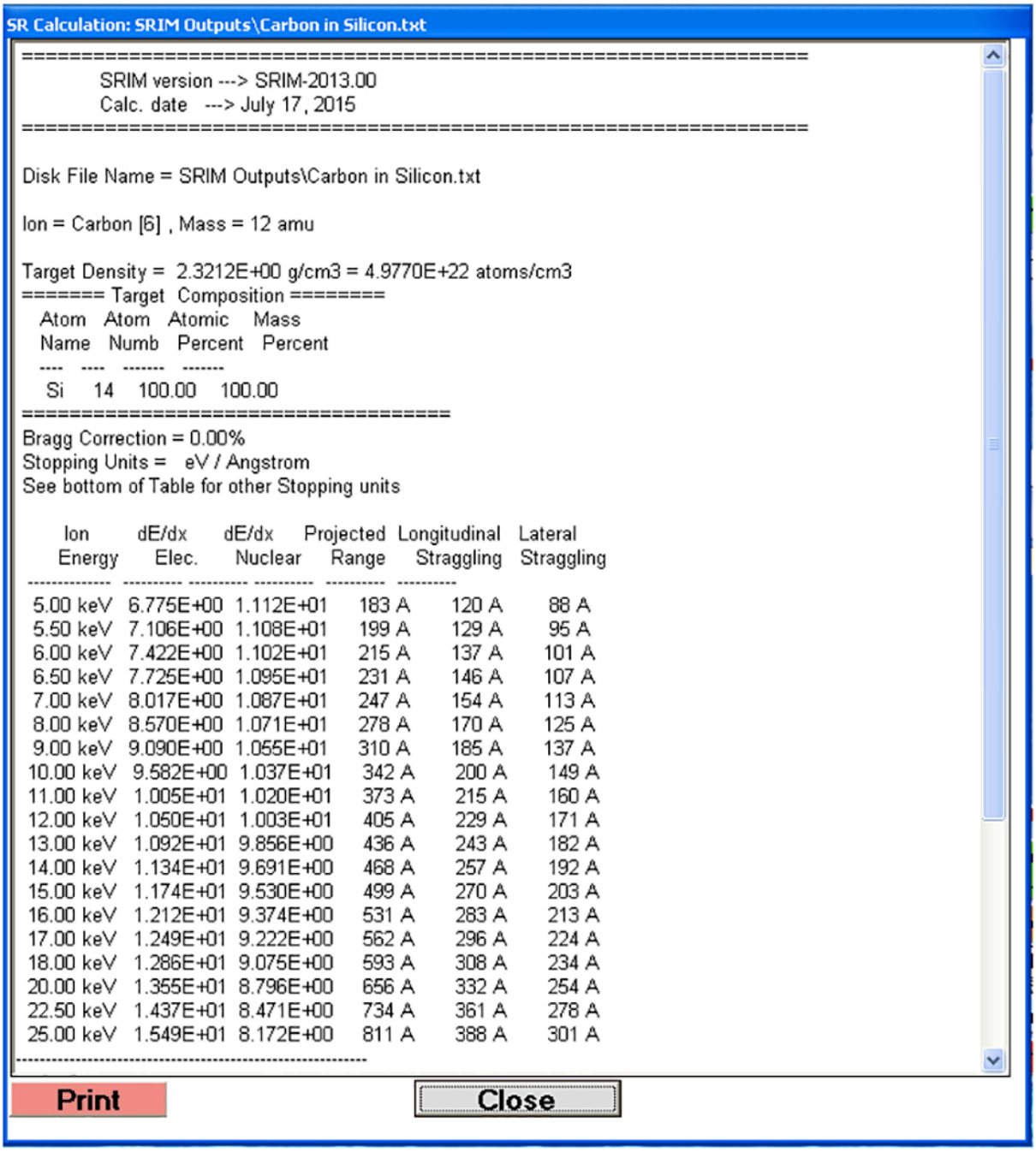

Figure 3.2 SRIM range table calculated for C:Si from 5 to 25 keV at normal Si density, without target heating. The projected range of C^+ ions at 20 keV is approximately 660 Å.

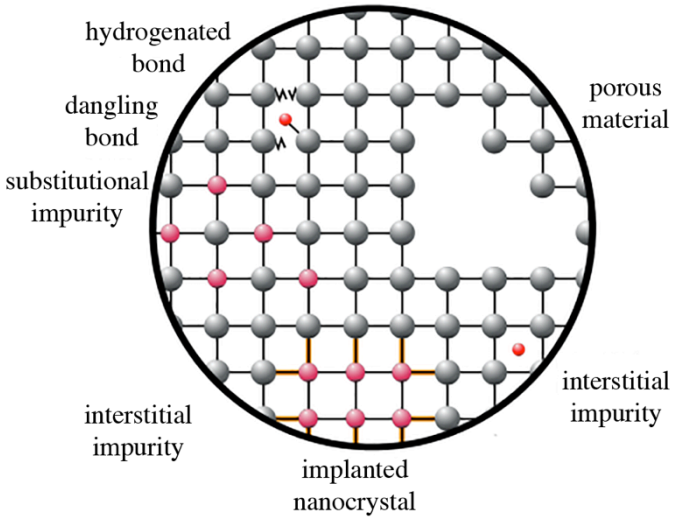

Figure 3.3 Cartoon picture of changes induced by implantation of ions into a crystalline target.

effect of induced lattice strain between the cluster and surrounding matrix. Some ions may fit into the space between native atoms, and remain as an interstitial impurity.

In addition to stoichiometric changes, the implanted ion causes damage to the physical target crystal lattice structure. If the energy transferred to a nucleus during a collision is larger than the lattice binding energy, then nucleus will be ejected from its position, leaving a lattice vacancy. The dislodged nucleus then has energy to collide with other nuclei in the target, which in turn may become dislodged. Interstitial impurities are formed when nuclei come to rest in positions that are not lattice points in the target structure. This type of physical defect can lead to extended defects and lattice dislocations in the material after annealing. Annealing treatments that reduce these defects require high temperature (~1000 °C) [63], [71]. An added advantage of annealing is the repositioning of implanted ions onto crystal lattice sites.

The orientation of the target crystal lattice and the incident ion beam must be considered for ion implantation treatments, shown in Figure 3.4. When the target is oriented in such a way

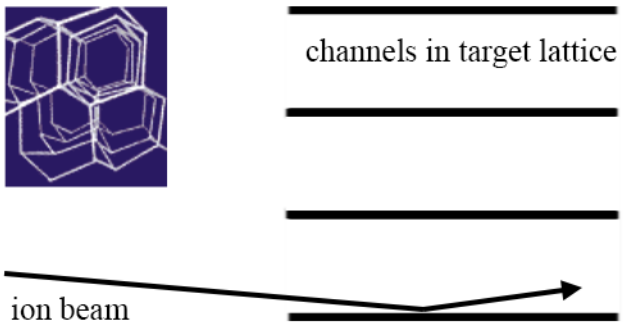

Figure 3.4 Ion channeling. Insert by Vincent Herr, 2001, GNU free documentation license [141].

that there is a clear path (channel) that is free of native target nuclei, and having low electron density, an ion may travel with diminished stopping power from what would be expected. The result is disagreement between simulation and treatment, an impurity in an undesired location in the target. The critical angle (Ψ) between the incident ion velocity and the crystal plane orientation for channeling to occur depends on the charge number of the ion and target (Z), the incident energy of the ion beam (E_{inc}), and the atomic spacing of the target (d) [63].

$$\Psi = 9.73° \sqrt{\frac{Z_{ion} Z_{target}}{E_{inc} d}}. \tag{3.8}$$

For the current exercise, the implanted ion is carbon, $Z_{ion} = 6$, the target is Si(100) with $Z_{target} = 14$, and $d = 1.8$ Å, and the implant energy $E_{inc} = 20$ keV. The critical angle is $\Psi = 15°$.

In order to eliminate unwanted effects due to ion channeling, ion implantation treatments are carried out off-axis, or the native lattice structure is amorphized by a pre-treatment of heavy ion implantation, or the implantation is executed with a surface oxide in place to randomize the incident ion paths into the target. When the implantation is done off-axis, the ion is more likely to collide with a target nucleus, and will not "see" any channels. For all intents and purposes the

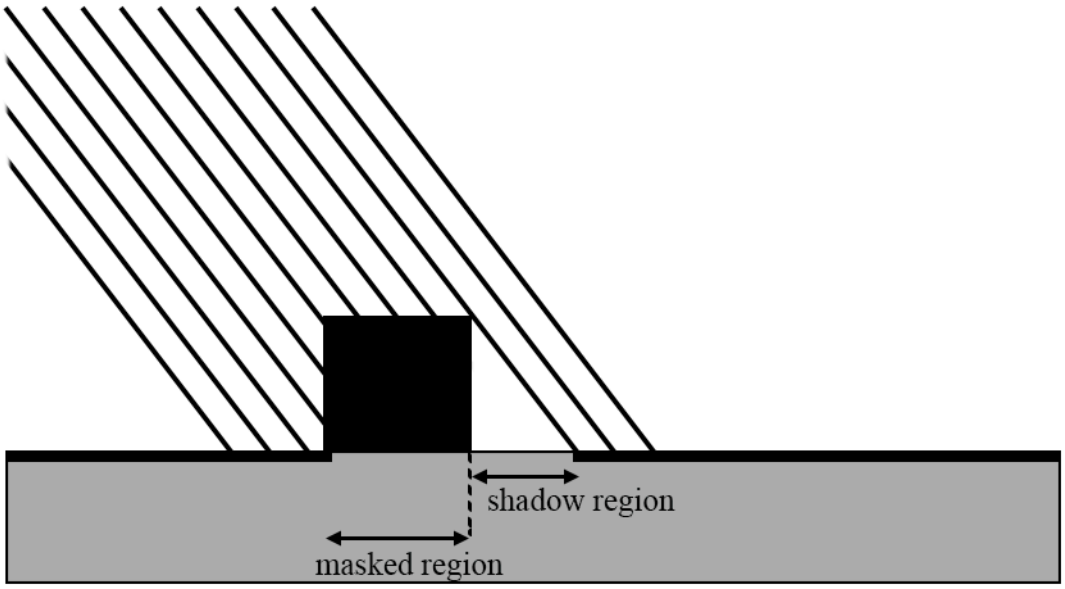

Figure 3.5 Illustration of ion implantation shadow: implantation with a mask, at an angle creates a region of non-uniform coverage.

ion does not see a lattice structure, and its behavior is based on the probability of collision. Since this is the case, the simulation of ion implantation can rely on an amorphous distribution of target atoms with the same density as the crystalline target [63], [64].

In addition to the defects caused by ion implantation, there are other concerns with ion implantation that should be discussed. When the ion implantation treatment involves a mask, if the implantation is done at an angle, the mask will create an ion beam shadow on the target, shown in Figure 3.5. This region will be neglected in the ion implantation treatment, and ion coverage will not be uniform. Unintentional masking may also occur with surface contaminants, which leaves an ion implant shadow on the target that can go unseen. Surface particles can come from improper wafer handling, improper vacuum equipment handling, use of unfiltered gas sources for venting vacuum chambers, and from the clamps used to hold the sample in place.

Care should be taken to avoid these issues by following proper procedures, and by using a clamp-less sample holder [63].

3.1.2. Simulations of Ion Implantation

The effects of ion implantation, including ion distribution and damage effects are simulated using the SRIM software package [65], [142]. The program uses Monte Carlo simulations to calculate individual ion trajectories into simulated amorphous material that has the same density as the implantation target. The ion paths (energy, direction, position) are calculated sequentially, until the ion kinetic energy falls beneath a threshold (the lattice binding energy of the target), or if the ion leaves the target. The ion trajectories within the target are calculated based on inelastic nuclear collisions, shown in Figure 3.6. The ion range vs. energy plots for both AT and HT Si targets are shown in Figure 3.7. The simulation of the final ion distribution includes a variety of useful parameters, including Rp and σ of the ions, shown in Figure 3.8. A more detailed simulation of the implantation at a specified energy provides the number of vacancies and number of sputtered ions (ions and target nuclei that leave the target) per implanted ion. For this project, the implantation energy is limited by consideration for the limits of the experimental equipment: fluences that can reasonably be achieved using IBS at 20 keV. The input parameters used for the simulations used for this work are shown in Table 3.1.

The use of target heating is included in this study for enhancement of SiC formation in Si. A target-holding plate with an electrical heater is installed in the target chamber to heat the Si wafer to 400 °C during ion implantation treatments, shown in Figure 3.9.

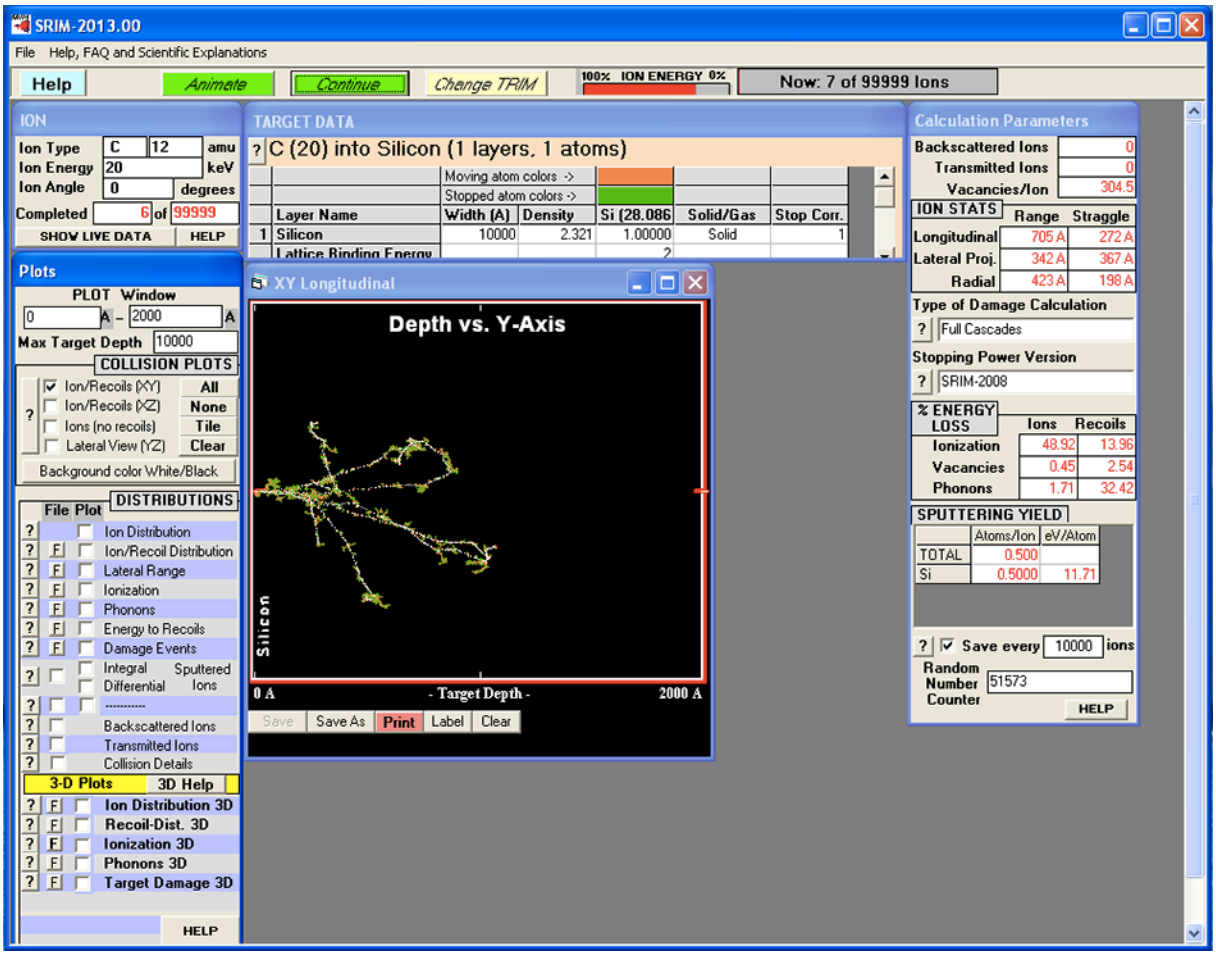

Figure 3.6 SRIM simulation of C:Si at 20 keV in AT target shows each ion path and collisions as the calculation progresses.

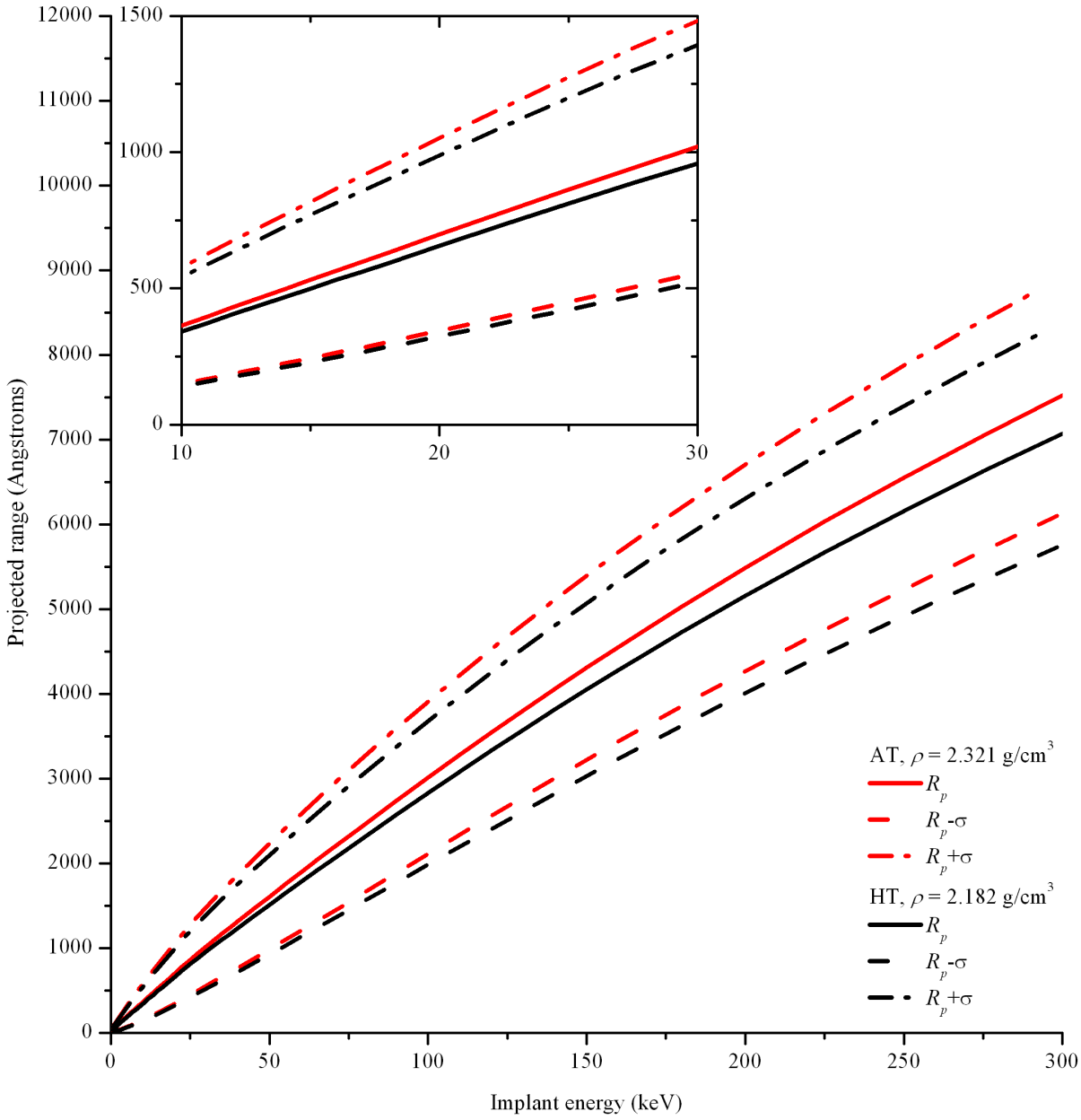

Figure 3.7 Projected range and longitudinal straggle for AT and HT Si.

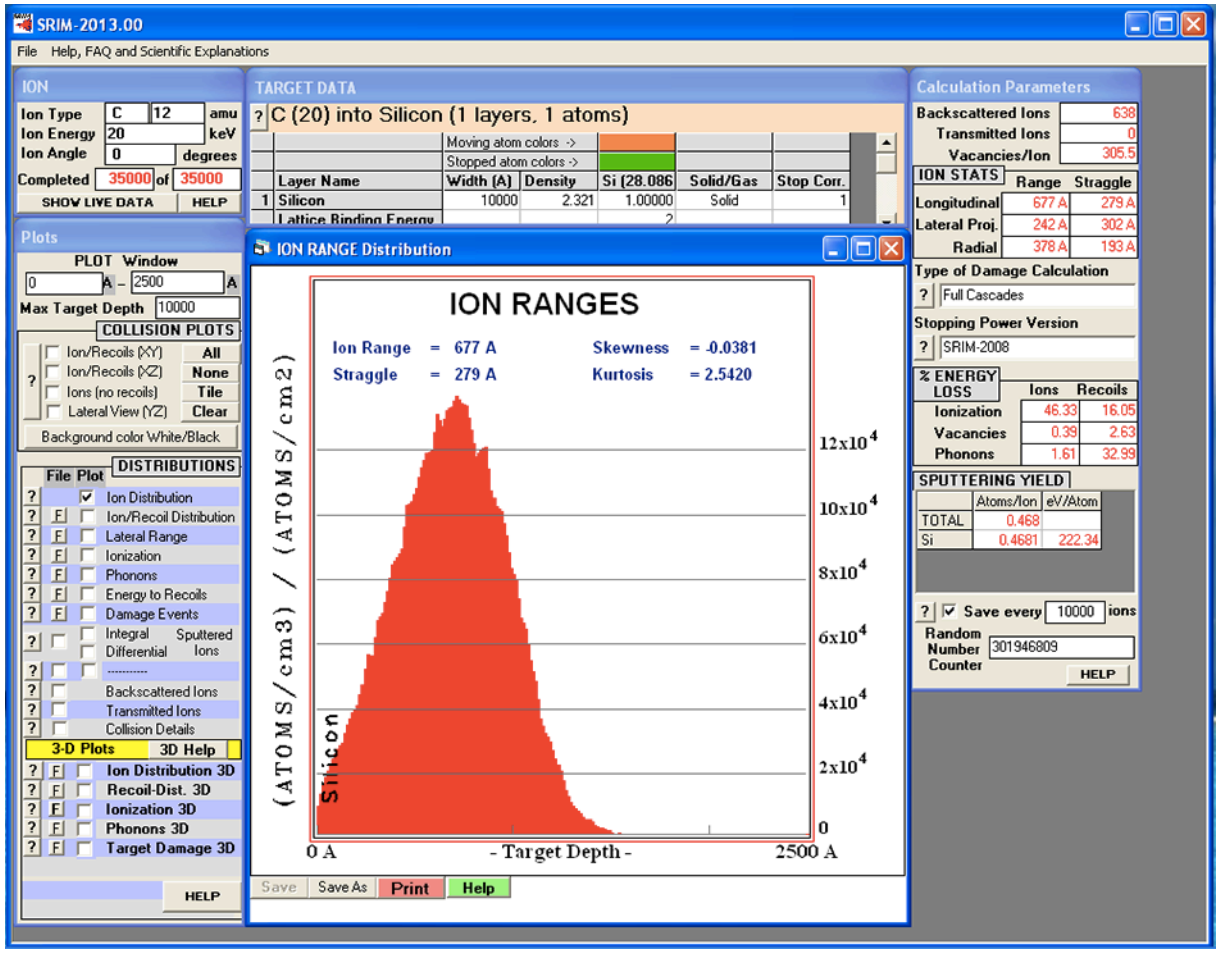

Figure 3.8 SRIM simulation of ion distribution results for AT C:Si at 20 keV. Shortened simulation is shown here, using 35,000 ions.

Table 3.1 SRIM simulation input parameters

Ion species	**Target layer**	**Ion energy (keV)**	**Target density (g/cm^3)**	
C^+	Si	5 to 60 keV (range table)		2.32
C^+	Si	20 keV	AT	2.321
			HT	2.182

Figure 3.9 The electrical target heating stage with Si target, installed in the ion implantation chamber in the CEDT IBS system at McMaster University.

The HT implant at 400 °C (673 K) is expected to induce a change in density of the target, and therefore the calculated ion distribution and target damage/sputtering. A model of Si density as a function of temperature is reported by Endo *et al*. [77]. The model is based on molecular dynamics simulations from 100 to 3000 K. The potential of the atoms in the material (solid or liquid) is complex, but a reasonable representation of the potential energy for Si is reported by Stillinger and Weber [143], and used by Endo *et al.* in their calculations [143]. The details of this simulation are beyond the scope of this thesis. The model for density (ρ) of Si as a function of temperature (T), in degrees Kelvin, is determined using the equation presented by Endo *et al.* [77]:

$$\rho = 2.33 - 2.19\times10^{-5}T \text{ g/cm}^2, \tag{3.9}$$

which yields a value of 2.182 g/cm^2 at 400 °C.

The SRIM simulation of C:Si at 20 keV for AT samples results in R_p = 677 Å, σ = 279 Å, 0.472 target atoms sputtered by implanted ions, and 305 vacancies/ion. For the HT target with reduced density, the simulation yields R_p = 720 Å, σ = 257 Å, 0.445 target atoms sputtered by implanted ions, and 159 vacancies/ion.

3.1.3. Ion Implantation Parameters: Fluence, Dose, Time

The implanted ion distribution in a target is described, to first order, by the Gaussian distribution, where the concentration of implanted ions, $N(x)$, changes with target depth (x):

$$N(x) = \frac{f}{\sqrt{2\pi}\sigma}\exp\left[\frac{-(x-R_p)^2}{2\sigma^2}\right]. \tag{3.10}$$

Note again, the difference between fluence, the number of ions implanted to the target area (ions/cm^2), and concentration, the number of implanted ions in a unit volume of the implanted

region (ions/cm^3). The application for the implanted material is used to select the desired N (and f), and implant energy. Range tables are used to estimate R_p and σ. The concentration is related to the fluence, f, and the width of the implanted region, w,

$$N = \frac{f}{w}. \tag{3.11}$$

For a Gaussian distribution of ions the width of the implanted region can be estimated by applying a Gaussian approximation, with width

$$w = \sqrt{2\pi}\sigma. \tag{3.12}$$

The fluence required for the desired concentration is

$$f = \sqrt{2\pi}N\sigma. \tag{3.13}$$

The desired fluence for an ion implantation treatment is reached by applying the implantation for an amount of time determined by

$$t = \frac{q_{ion}Af}{I_{beam}}. \tag{3.14}$$

The time, t, required for a desired f is dependent on the charge of the ion species, q_{ion}, the area of the implantation, A, and the ion beam current, I_{beam}.

The fluence values for this study are chosen to be 3, 5 and 10×10^{16} ions/cm^2 onto targets 3×3 cm^2. The high fluence is based on a C:Si fluence study [47], but is limited by the length of time that is reasonable to maintain a stable ion beam in the IBS system at 20 keV. The implantation times for the treatments used in this thesis are shown in Table 3.2 with I_{beam}, f, and t for the same implant using the PIII technique.

Table 3.2 Ion Implantation Parameters

Total fluence (ions/cm^2)	**Carbon concentration (ions/cm^3)**	**Beam current (μA)**	**Actual IBS implantation time (min.)**	**Predicted PIII implantation time (min.)**
Ambient Temperature				
3×10^{16}	3.6×10^{21}	~14	71	15
5×10^{16}	6.0×10^{21}	15 to 14	126	24
10×10^{16}	12×10^{21}	10 to 14	239	50
High Temperature				
3×10^{16}	3.4×10^{21}	7 to 10	60	15
5×10^{16}	5.7×10^{21}	15 to 20	96	24
10×10^{16}	11×10^{21}	13 to 22	178	50

3.1.4. Ion Beam Synthesis

Ion beam synthesis is used as the implantation method to prototype the C:Si material used for LED fabrication. A schematic of the ion implanter used at the CEDT is shown in Figure 3.10. The ion source is a hot cathode arc source that ejects electrons into a neutral gas [63], [144], [145]. The plasma reactor is maintained at a vacuum of 10^{-5} to 10^{-7} Torr in order to maintain a stable arc. The electrons excite the source gas, causing the molecules in the gas to lose any electrons with lower binding energy than the energy of the free electrons. For these experiments, CO_2 is excited to form plasma containing many ion species (CO^+, C^+, O^+). The positive ions are then extracted into the beam line by a magnetic field. The beam line is typically maintained at 10^{-6} Torr to avoid contamination of other ion species form the beam line and maintain beam integrity. A second magnetic field is used to separate the ions based on the charge, q, and mass, m, as shown in Figure 3.11. In this way the user can select a particular ion species for implantation, such as C^+ ions to be implanted to silicon. The force, $\boldsymbol{F}$, exerted on the ions by the

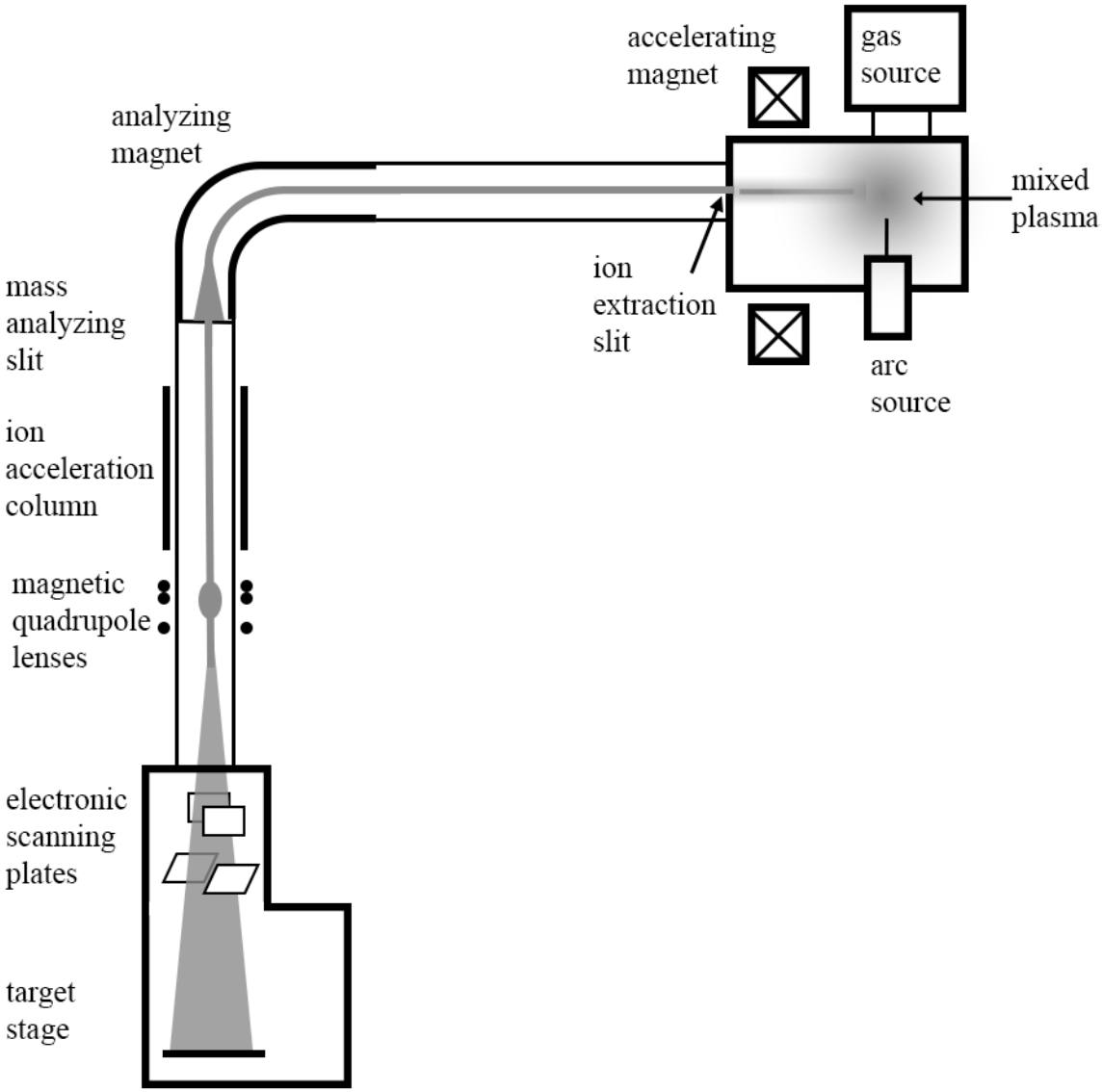

Figure 3.10 Schematic of ion beam implantation system.

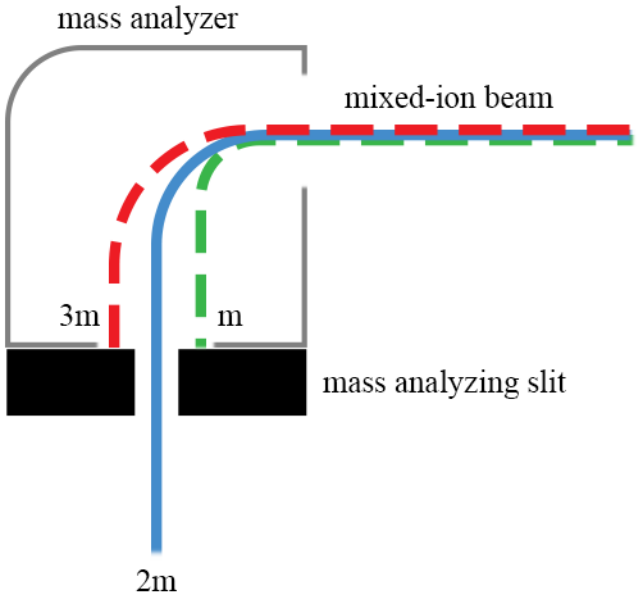

Figure 3.11 Schematic of mass analyzer section of ion beam line.

analyzer magnet is

$$\boldsymbol{F} = q|\boldsymbol{v}\times\boldsymbol{B}| = \frac{mv^2}{R}. \tag{3.15}$$

The force exerted by an applied magnetic field, $\boldsymbol{B}$ applied perpendicular to the ion velocity ($\boldsymbol{v}$) results in a curved ion path with radius, R. The analyzing magnet is used to apply $\boldsymbol{B}$, that bends the paths of ions with the desired m/q. Undesired ions hit the beam chamber walls, or the surface of the analyzing slit. The m/q selected ions pass into the beam line. The ion beam is accelerated by an applied electric field, to the desired energy, and quadrupole magnets are used to set the beam dimensions. Electrostatic scanning plates direct the C^+ ion beam onto the target area in a rastered scan. A Faraday cup measures I_{beam} incident on the sample without removing ions from the beam. For high fluences of ions into a sample, and large target areas, the length of time required to execute the implant may be longer than is reasonable to maintain a stable beam

for a specific dose. The beam current may drift or become disrupted; this is a limiting factor in deciding the fluence for these experiments [63].

When using IBS for ion implantation treatments is it important to remember that ions from previous implants may exist in the beam line, heavy ions especially. Industrial facilities have two implanters for applications where treatments with heavy, then light ions are required (such as pre-amorphization of a target). Another issue is with large implant areas that require a wide range of angles with rater scanning, which present problems with masked implantation (ion beam shadows) [63].

3.1.5. Plasma Ion Immersion Implantation

The process of PIII uses ions from a plasma reservoir as the ions source. An applied potential attracts and accelerates ions from the plasma towards the target. There are several advantages to using PIII: large and complex structures can be implanted with a uniform impurity layer, as long as the features of the target are smaller than the plasma sheath (discussed in this section). Objects or arrays of objects can be implanted without the need to control or focus an ion beam. Since the ion source is uniform and surrounds the target, the amount of time to implant a surface does not depend on its area. By using a pulsed bias to apply a high voltage to the target, the target is able to neutralize in between pulses, eliminating charge build-up that obscures ion beam implantation [146].

The limitations of PIII include the difficulty of direct fluence measurement, where PIII operators rely on secondary measurement systems such as current probes and assumptions of plasma parameters. The uniformity of the implant layer is determined by the plasma sheath size, and is affected by any inhomogeneity in the applied potential. PIII is best applied to conductive

targets; insulating targets require special treatment to mediate surface charging effects since the insulating material will not drain the charge induced by ion implantation as effectively as other materials [138], [146]. Another, possibly undesirable, effect of using PIII is the introduction of multiple ion species, where the source gas is a molecule such as methane (CH_4) and the plasma consists of multiple ion species, for example CH_4^+. The molecule breaks apart on contact impact with the target and both C^+ and H^+ are implanted to the target; if the molecule is implanted at 20 keV, the C^+ is implanted with (12 amu/16 amu * 20 keV) 15 keV and the H^+ implant energy is (1 amu/16 amu * 20 keV) 1.3 keV. The implantation models that have been developed are successful in determining the amount and distribution of impurities as a result of both PIII and IBS[63]. It is important to remember that additional post-processing treatment like annealing may cause additional diffusion of the implanted impurities and defects in a sample [63].

The Bradley Lab PIII equipment, shown in Figure 3.12, is the Plasmionique ICPIII-600 Radio-Frequency Inductively Coupled Plasma (RF-ICP) reactor [91], [147]. The target bias is applied using a stackable Marx generator and a high voltage pulse 10x step-up transformer. The Marx stages operate based on Insulated-Gate-Bipolar-Transistors (IGBTs) that are capable of high pulse, high power applications; 500 V to 2kV. The Marx stages provide fast rise and fall times, and less than 1% drop across the pulse peaks. They can be stacked to achieve higher voltages, the U of S system has used up to four 500 V stages in the past. The maximum voltage (~20kV) that can be applied to the platen is limited by the HV feed-through that connects the target platform in the plasma reactor to the HV electronics. The PIII implantation process is presented schematically in Figure 3.13 and described in more detail in [138]. The general principles are outlined in this section.

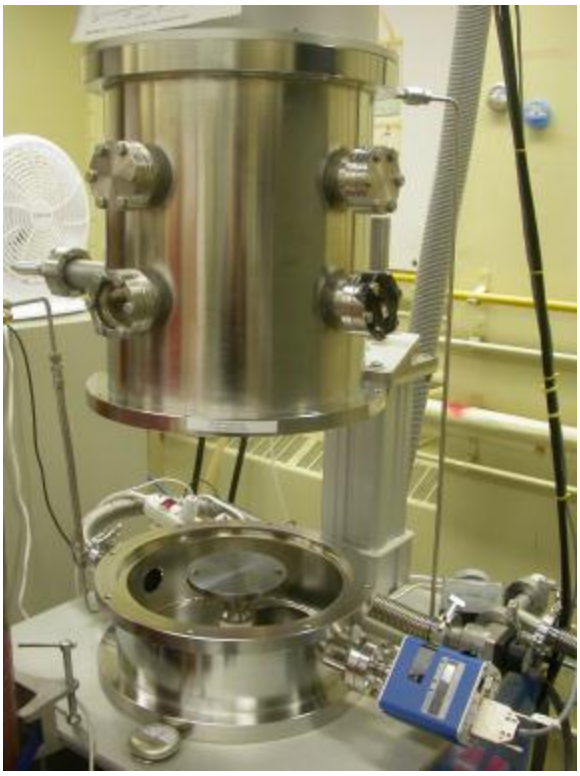

Figure 3.12 Plasma reactor (open) showing high voltage platform in the plasma reactor used for PIII processing.

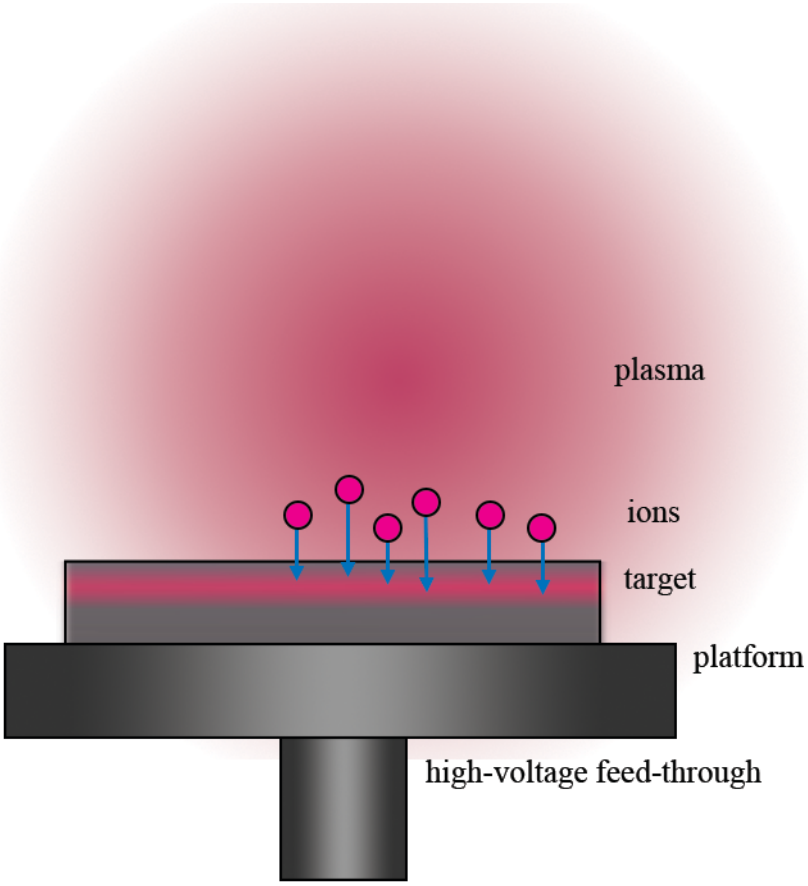

Figure 3.13 Illustration of PIII processing: the target is immersed in plasma, and rests on a conductive platform. A high-voltage pulsed potential is applied to the platform, producing a high electric field that accelerates ions from the plasma sheath towards the target.

The plasma reactor is evacuated to ~10^{-6} Torr to reduce contaminants. When a feedstock gas is fed into the vacuum chamber, and the radiofrequency (RF) field is applied, the plasma forms within a few nanoseconds. The electrons in the plasma return to ground through the chamber walls and any available surfaces to ground, leaving the plasma floating at a positive potential ~40 eV. The outer regions of the plasma develop an electron poor sheath region that attracts ions, however the ions are much slower than the electrons, and the sheath stabilizes with a steady average electric field. The ions left in the plasma are no longer shielded by the electrons and respond to the RF field to form a "matrix sheath" in a non-equilibrium state with uniform ion density. The PIII setup can be treated like parallel conducting plates in a vacuum since from an electronic point of view it doesn't matter if the charge carriers come from a metal plate (like the platen) or a plasma. The plasma reservoir is shielded by the collective charges of the ions being attracted towards the target platform, and electrons being repelled by the applied negative potential. The affected plasma is only a region on the same size scale as the target platform; the plasma reservoir acts like an electrode of a capacitor. The applied negative potential is pulsed to reduce charge-buildup on the sample and ensure uniform implantation. After a pulse, the ions move into the depleted sheath region with velocity

$$v_{Bohm} = \sqrt{\frac{eT_e}{m_{ion}}}. \tag{3.16}$$

The Bohm velocity is the minimum velocity that an ion has when leaving the plasma with no applied electric field. This is the velocity with which ions are dragged by electrons leaving the plasma towards the chamber walls. It is used as a baseline for implantation calculations, since it is impossible to measure the ion velocity in the sheath without perturbation caused by the probe.

Note that ions moving with the Bohm velocity do not have enough energy to be implanted into a sample – an external voltage is required to accelerate the ions to significant implant energies.

The ion current density, J_{ion}, that is associated with the Bohm velocity is given by the charge state, q = 1 in most cases, the charge value, e, and the ion current density, n_{ion}.

$$J_{ion} = qen_{ion}v_{Bohm}. \tag{3.17}$$

The current density of ions leaving the sheath during an applied pulse is determined by the potential applied across the electrodes, V, the permittivity of free space, ε_0, and d, the ion distance from the target,

$$J_{ion} = \frac{4\varepsilon_0}{9}\sqrt{\frac{2q_{ion}}{m_{ion}}}\frac{V^{3/2}}{d^2}. \tag{3.18}$$

This is the Child law for space-charge-limited flow of charged particles in a vacuum [138].

The quantity and distribution of ions implanted into a surface is determined by the ion fluence and the implantation time. The fluence depends on parameters determined by an ion implantation model provided by open source software, outlined in this section.

During the implantation process, the applied voltage is pulsed to allow the pre-sheath to replenish with ions to implant and to prevent charge buildup on the target. The pulse peak width, t_p, and the number of pulses, n_p, define the length of time that ions are being implanted to a target, so that the fluence of ions during each pulse is determined by the equation

$$F = \frac{J_{ion}n_p t_p}{q_{ion}}. \tag{3.19}$$

For a desired f, the number of required pulses is determined, for example with t_p = 13.8 μs at 202.8 Hz, set by the pulse generator [147]–[149].

$$n_p = \frac{Fq_{ion}}{J_{ion}t_p}. \tag{3.20}$$

The total time required for implantation treatment is the number of pulses multiplied by the period, T, of the applied pulse,

$$t = n_p T. \tag{3.21}$$

The total ion implantation time for PIII processing of C:Si, where $q_{ion}(C^+)$ = 1.6 × 10^{-19} C, $J_{ion} \approx 2 \times 10^{-3}$ A/cm^2 [148], is presented in Table 3.2. The time required for equivalent treatments of C:Si are significantly less for PIII than IBS processing.

3.2. Post-implant Treatment

The ion implantation process, especially at such high fluence, results in damage to the target lattice structure, which is mitigated by thermal annealing. Thermal processing is used to repair damage (vacancies) by promoting migration of displaced (interstitial) atoms to these vacancies, and to "activate" the implanted impurities by facilitating their migration to lattice sites in the implanted region. In silicon that has been amorphized by ion implantation, annealing temperatures of 500 to 600 °C results in diffusion and agglomeration of lattice vacancy defects, such that regions of extended lattice defects are formed. For higher annealing temperatures of > 850 °C these defects are reduced in number, with the possibility of void formation, depending on fluence and synthesis technique [63], [150]. The post-implant annealing process induces recrystallization by solid phase epitaxy, the amorphous material crystallizes onto the substrate, with the same crystal orientation [46], [63], [67], [151]. In C:Si materials, the precipitation of SiC crystallites in the implanted region, along with amorphous layers of carbon-rich silicon is discussed by Lindner *et al.* and Wang *et al.* [44], [57], [60]. The implantation of carbon results in formation of Si—C bonds, until the concentration of carbon reaches a maximum of 4.5 × 10^{17} cm^{-3}, after which carbon clusters are formed [57], [60]. For low fluence, or early in an

implantation treatment, the implanted carbon forms some SiC crystallites in the existing lattice structure of the c-Si target. The growth of these crystals is slow because of the low solubility of carbon in silicon, and the crystallites that form early in the implantation process are included in the structural damage caused by the continuing influx of ions. The Si—C bonds are destroyed by incident ions that scatter one of the atoms to an interstitial position in the implanted region. These interstitial atoms contribute to the amorphous carbon-rich silicon layers that are observed in C:Si materials [44]. The implanted carbon ions continue to form Si—C bonds or amorphous carbon clusters, and the C—Si dimers agglomerate on silicon interstitial sites. These become the nucleation sites for further SiC crystallization during post-implant annealing [44]. The growth of the SiC crystals in the C:Si layer is described as a phase transition between a-SiC and β-SiC using the Avrami equation [57], [58].

$$X_T = 1 - \exp\left[\left(-\frac{t-\tau_0}{\tau_c}\right)^{m+1}\right]. \tag{3.22}$$

The fraction of the volume of transformed material, X_T, is determined by the lag time for nucleation, τ_0, the characteristic growth rate for the crystal, τ_c, the dimensions of growth m = 1, 2, 3, and the annealing time, t [57].

In this study, in addition to the post-implant annealing treatment, a subset of targets are annealed *in situ* for comparative study of the AT and HT C:Si materials. A heated target stage is used heat the target to 400 °C during the implantation process. These HT targets are treated with the same fluence (3, 5, 10 × 10^{16} ions/cm^2) as the AT. The AT samples experience heating due to the energy imparted by the arriving ions, but the experimental apparatus is not equipped to measure this effect. After implantation, all samples are annealed in a tube furnace at 1000 °C for 1 h in a flowing nitrogen gas atmosphere. As discussed in 1.2.2, this temperature is selected

based on previous work on annealing treatment C:Si that demonstrated that this temperature is sufficient for the purpose of this work [71].

It should be noted here that the goal of these experiments is to produce C:Si LEDs, and it is known that oxygen enhances luminescence in similar devices [111], [152]. It is also known that oxygen plays a role in SiC formation in Si targets after ion implantation [43]. The native oxide layer on the Si wafers i.e. the native oxide layer is not removed before implantation or before application of electrodes for LED fabrication. Annealing in a nitrogen gas atmosphere reduces the enhancement of the oxide layer during post-implant annealing.

3.3. Diode Fabrication

The diodes are fabricated using physical vapor deposition (PVD) of metal onto a sample of semiconductor trial material [91]. The procedure uses small pellets of the metal to be used in the coating, placed in an Al boat. The metal is evaporated by resistive heating of the boat, and travels through a vacuum chamber (10^{-6} Torr) and lands on the target. The target is held on a rotating platform, which enhances uniformity of the coating layer. The thickness of the layer is measured by a quartz crystal microbalance. The depositions for this work are completed at the University of Saskatchewan Chang Lab using an Ångstrom Engineering Åmod PVD system.

The Schottky diode architecture is shown schematically in Figure 3.14. The device consists of a piece of the C:Si wafer with an Aluminum (Al) coating (600 nm) on the back, and a semi-transparent Gold (Au) contact (200 nm) on the implanted surface. After implantation, the wafer is cleaved to fit into a tube furnace, and annealed. The contacts are applied by PVD, followed by contact firing at 400 °C in flowing N_2. An additional processing step of cleaning (sonication) before the application of metal contacts is discussed in section 4.6.1.

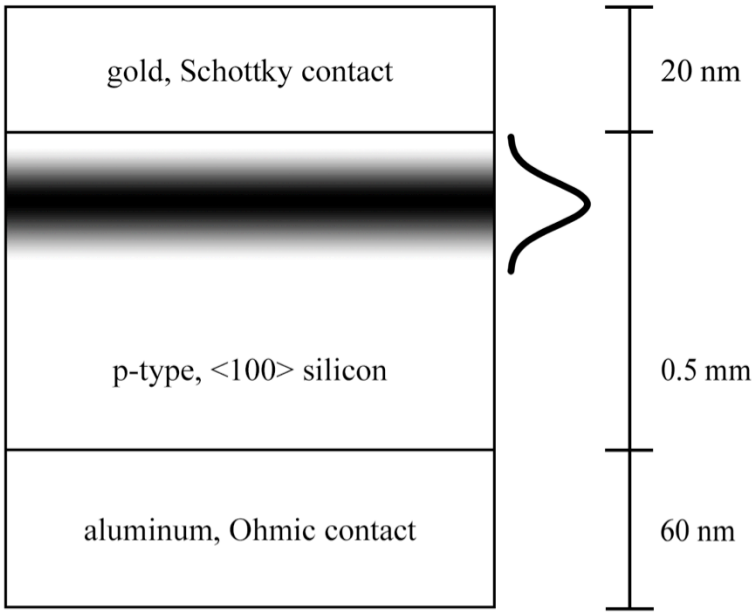

Figure 3.14 Schematic diagram of cross-section of the diodes fabricated for this study. The metal contacts are shown with sandwich architecture, the implanted ions are expected to have an approximately Gaussian distribution with depth into the sample. Adapted from Purdy *et al.* 2015, © 2015 IEEE [89].

3.4. Materials Synthesis Parameters

The ion implantation of Si is conducted at the CEDT at McMaster University in collaboration with Dr. Andrew Knights and Doris Stevanovic. The details of the synthesis are outlined in Table 3.3. The silicon targets used for the implantation are boron doped (*p*-type) to 1-10 Ω·cm, 500 μm thick <100> crystal orientation, grown using the Czochralski technique.

3.5. Raman and Infrared Spectroscopy

The C:Si material can be expected to contain some C—C and Si—C bonds, which can be quantified using IR and Raman spectroscopic techniques. These complimentary techniques are

Table 3.3: Parameters of ion implantation and post-implant processes.

Ion beam energy: 20 kV			
Sample designation	**Beam current ($\mu A/cm^2$)**	**Implantation time (min.)**	**Fluence ($ions/cm^2$)**
A1	10 to 14	239	10×10^{16}
A2	14	71	3×10^{16}
A3	15 to 14	126	5×10^{16}
Samples heated at 400 °C during implant			
H1	7 to 10	60	10×10^{16}
H2	15 to 20	96	3×10^{16}
H3	10 to 12	190	5×10^{16}
All samples annealed at 1000 °C in flowing N_2 after implant			

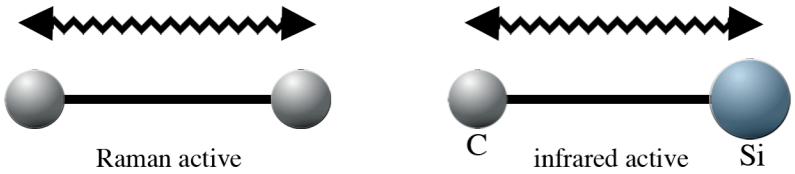

Figure 3.15 Raman and IR active vibrational modes. Vibrational modes in C—C bonds are Raman active and Si—C bonds are IR-active.

used to examine vibrational modes of molecules or crystals. Raman is used to measure vibrational modes that result in a change in polarization of the electron clouds in the bond; and IR is used to measure vibrations that exhibit a change in the dipole moment of the molecule, as shown in Figure 3.15 [153].

It is expected that the Raman results would show C—C bonds with Raman shift peaks near 1350 to 1580 cm^{-1}, being the disordered (or "glassy") carbon and highly ordered pyrolitic graphite (HOPG) states of carbon [154]. The post-implant annealing process is expected to enhance growth of SiC, and reduce the amount of C—C bonds in the C:Si, which would be observed as a reduction in peak height in the Raman spectra.

IR spectroscopy is used to identify the SiC bonds in the C:Si, which have a band near ~800 cm^{-1} [28]. The spectra are collected using a Michelson-Morley type spectrometer, which

directs light of varying frequency onto a sample, which absorbs and reflects some of the light. The reflected beam is recombined with the incident beam to form an interferogram. Fourier transform infrared spectroscopy relies on the symmetry of the interferogram, where one half of the interferogram is measured from the central peak. The spectral width that is measured is increased, and the Fourier transform yields higher resolution results because of the virtually extended data set. The as-implanted samples are expected to show SiC spectra with peaks at lower wavenumbers (~740 cm^{-1}), and these peaks would appear at ~800 cm^{-1} with higher intensity in the post-annealed samples [47], [56]. It is also expected that the as-implanted HT samples would have higher SiC peaks than the AT samples, since the annealing process is expected to facilitate SiC bond formation. The *in-situ* annealing during implantation is expected to be incomplete, and post-implant annealing should enhance the SiC quality.

The Raman and FTIR measurements are conducted at the Saskatchewan Structural Sciences Centre (SSSC) at the University of Saskatchewan (U of S), using the inVia Raman microscope with Smiths Detection IlluminatIR II microspectroscopy accessory. The Raman measurements were collected using a 514.5 nm laser, from 100 to 3200 cm^{-1}. The FTIR measurements are collected using an all-reflective objective (ARO) lens, from 650 to 4000 cm^{-1}.

3.6. Grazing-incidence X-ray Diffraction

X-ray diffraction is used to determine the structure of the implanted samples [155]. The basic principle of this measurement is described as Bragg scattering of X-rays from planes of ordered atoms within a crystal, applied to determine surface or thin-film characteristics. Variations on the technique may be used to determine surface, or thin-film characteristics. The grazing-incidence X-ray diffraction (G-XRD) technique uses low angles of incidence that

promote evanescent waves to propagate on the surface of the sample, increasing the sensitivity to the surface and subsurface structure. This study makes use of G-XRD to investigate C:Si, and to compare with results from previous studies [47], [71]. The G-XRD measurements are collected by the McMaster Analytical X-ray (MAX) Diffraction Facility, with measurement parameters specified by the author [156]. The data are collected using the Bruker D8 Davinci diffractometer with a Vantec500 area detector, 3-circle goniometer, and parallel beam optics. The 2-dimensional data are integrated into 1-dimensional plots. The X-ray source is a Cu rotating anode generator ($K\alpha$ = 1.54 Å), the data are collected with a 2° angle of incidence, and 2θ range from 23.5° to 79.2°.

In the classification of XRD analysis, Mercury software is used to calculate the diffraction pattern of a specific material (i.e. ß-SiC, Si), and experimental results are compared to this in order to identify crystalline structure [157]. For this work, Si (516688-ICSD) and ß-SiC (182362-ICSD) are modeled using Mercury and the Cambridge Crystallographic Data Centre database.

3.7. Transmission Electron Microscopy and Electron Energy Loss Spectroscopy

Transmission electron microscopy uses a beam of electrons, projected onto and through a sample to generate high-resolution images and diffraction patterns. This requires the sample to be thin enough for electron beam transmission (less than 500 nm). Two of the approaches to TEM imaging are bright field (BF) and dark field (DF) imaging: BF imaging makes use of the un-scattered transmitted electron beam, while DF imaging uses on of the diffracted electron

beam. The un-scattered transmitted electron beam may also be used for EELS, where the electron beam undergoes inelastic scattering with the target, and the scattered beam is used to identify elements in the scattering source. This method is especially sensitive for elements with lower atomic numbers, like carbon. The TEM and EELS techniques are used to examine effects that depend on bonding or crystal order, which are ideal for observation of ion implanted materials composed of amorphous and porous material.

These techniques use an electron beam transmitted through the sample, which requires sample preparation using a focused ion beam (FIB) cross-sectional lift-out technique to etch or remove part of the surface, leaving a raised cross-section to be measured.

In BF TEM, measuring the transmitted electron beam after it has passed through the sample, sometimes can be distorted due to diffraction effects from Bragg scattering. This is avoided by using high-angle annular dark field (HAADF) technique, shown schematically in Figure 3.16 [158], [159]. Measurement of incoherently scattered electrons using an annular dark field detector is useful in multiple ways. The diffraction effects seen in traditional scanning TEM measurements are eliminated, and the scattered electrons have different energies based on the atomic number of the scattering atoms in the sample. This results in a map of the sample with contrast dependent on the elemental composition. Use of an annular detector allows the main body of the beam to pass through to an EELS detector; scanning TEM and EELS measurements may be collected simultaneously [160].

As this measurement technique is expensive, and thus only the highest fluence samples are measured and presented in this thesis. The measurements are collected at the Canadian Centre for Electron Microscopy (CCEM) using a FEI Titan 80-300 HB microscope [161].

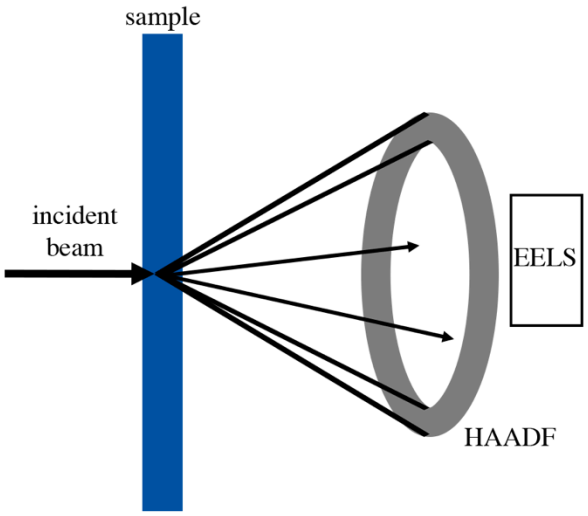

Figure 3.16 Schematic of HAADF and EELS detector setup. Adapted from [160].

3.8. Diode Characterization

The diodes are characterized using a water-cooled *I-V* testing bed, shown in Figure 3.17. Temperature measurements are collected using a thermocouple attached to the top plate of the test-bed, through ~5 mm of Al from the sample surface. Two multimeters are used to measure *I* and *V* in the driving circuit. A collimating lens and fiber-optic cable is attached to the top Al plate to allow luminescence measurements to be collected with a bias voltage applied to the sample. A measurement of the diode area is required for current density calculation, and normalization of the samples to each other. This is measured by taking an image of the diodes with a known length for calibrating the scale of the image (like a Vernier scale). The number of pixels in the image corresponds to a chosen calibration length in the image, and the number of pixels in the diode image corresponds to the area of the diode, a sample of this is shown in Figure 3.18.

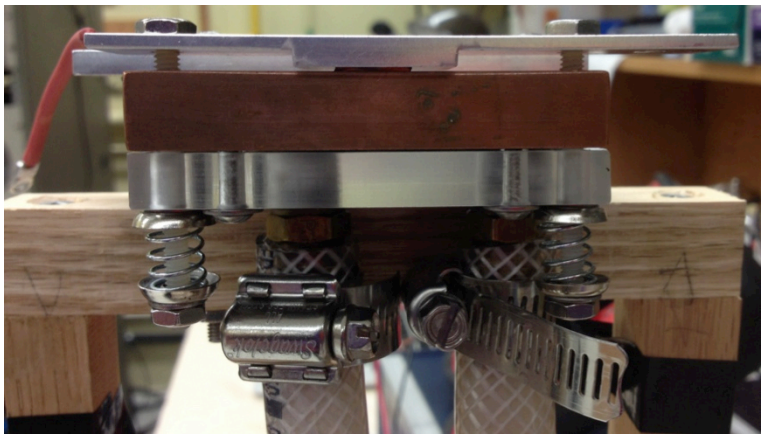

Figure 3.17 Photograph of water-cooled *I-V* testing platform with sample diode in place.

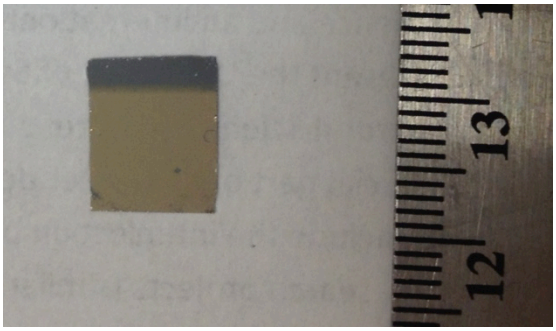

Figure 3.18 Example image of diode used for measuring diode size (HT 10×10^{16} ions/cm^2 seen here). The length of pixels and length on the ruler in the image are used to determine the scaling factor for the diode dimensions. Irregularities in the sample edges, and in the portion of the sample masked by clips used to secure the sample during coating application complicate the "pixel counting" method. The area is used to calculate the current density of the sample diode curve.

CHAPTER 4

RESULTS AND DISCUSSION

The results of the material characterization and device testing experiments are reported in this chapter. The first section, regarding materials characterization, includes the results from Raman and FTIR experiments, used to identify the chemical composition of the C:Si before and after annealing. The distribution of implanted ions is observed using EELS, combined with TEM and G-XRD measurements to form a picture of the physical structure of the C:Si. The results of the diode testing: *I-V* curve and diode parameters using the Shockley diode equation are discussed here.

4.1. Raman Spectra

Raman spectra collected for the C:Si at all doses, before and after annealing, are shown in Figure 4.1 where the expected bulk crystalline Si Raman shift is 525 cm^{-1}, and carbon *D*-band and *G*-band are 1366 cm^{-1} and 1563 cm^{-1}, respectively. The spectra of the as-implanted AT C:Si shown in Figure 4.1 (a) has a broad peak at 466 cm^{-1}, which is associated with a-Si [162]. The c-Si peak is observed at 518.7 cm^{-1}, and it is understood that the Raman spectrum peak frequency decreases for smaller Si crystallites [162]. The second-order Si band at ~960 cm^{-1} is not observed in these samples due to the amorphous nature of the material resulting in low-intensity, broad Si bond peaks. A broad peak at 800 cm^{-1} is observed, which has been observed in Raman spectra of other C:Si materials, and corresponds to Si—C bond vibration [45], [50]. The probability of measuring Si—C vibration using Raman excitation is low compared to the Raman excitation and detection of Si—Si. However due to the amorphous nature of the samples, the SiC peak appears

in the Raman spectra obtained for this study. The expected carbon peaks between 1300 cm^{-1} and 1600 cm^{-1} appear broad and weak, shown in Figure 4.2. The low fluence C:Si samples have smaller carbon bands, and therefore less C—C bonding than the higher fluence samples. This is consistent with previous work that indicates that carbon concentration increases with fluence and there is a threshold above which Si is saturated and the implanted carbon forms clusters [47], [56]. Annealing of the AT C:Si results in Si crystal formation, and the c-Si peak is observed at 520.4 cm^{-1} in the annealed samples, as shown in Figure 4.1 (b). This indicates that the Si re-crystallizes and the crystallites grow in size during the annealing process. The second-order c-Si band is observed for these samples, and the carbon bands disappear, as expected. The SiC band is also lost, where the probability of Si-Si Raman excitation is higher in the more crystalline material. The Raman spectra show that the annealing process for AT C:Si recrystallizes the implanted Si, and the carbon clusters are absent in the annealed samples.

The as-implanted HT C:Si results shown in Figure 4.1 (c) have a stronger, more well defined c-Si peak at 518.7 cm^{-1}, where the target heating enhances bond formation during the implant process. The Raman spectra for the carbon peak region shown in Figure 4.2 has a diminished response from the carbon peaks, compared to those in the AT as-implanted samples. The peak height of the carbon peaks corresponds to the fluence of the implant, but less so than in the AT samples. The post-anneal HT measurements seen in Figure 4.1 (d) again show that post implant annealing improves c-Si structure, eliminates C—C bonds in the C:Si. The changes produced by post–implantation thermal annealing show that the partial anneal that occurs during implantation with or without applied heat is incomplete without post-implant annealing.

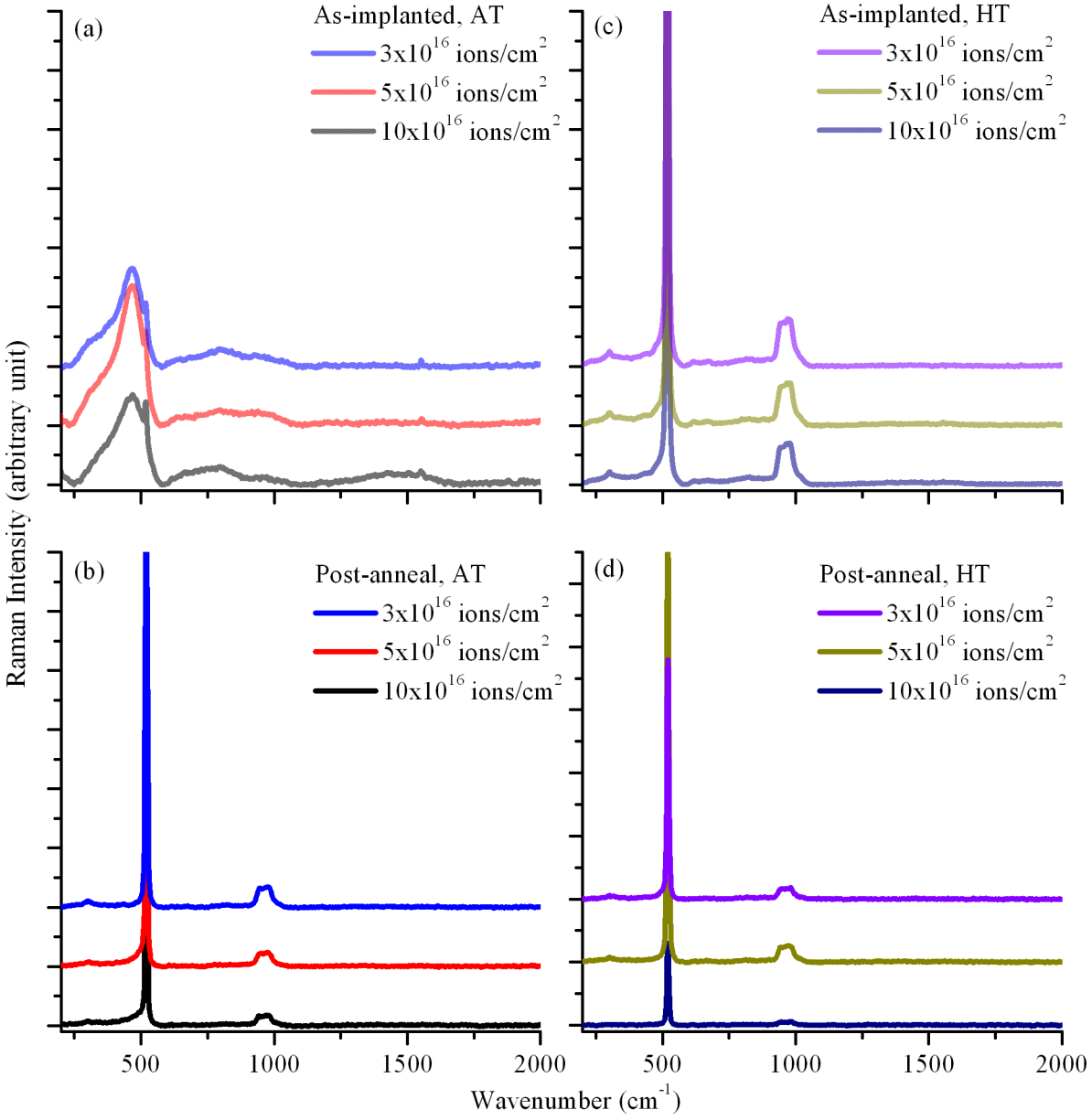

Figure 4.1 Raman spectra, offset for clarity, of as-implanted (a) AT as-implanted, (b) AT post-anneal, (c) HT as-implanted, and (d) HT post-anneal C:Si. In (a) the band at 466 cm^{-1} is attributed to a-Si. In all panels, the bands near 520 cm^{-1} and 960 cm^{-1} are first- and second-order c-Si. A broad peak associated with C—C bonds (1300-1600 cm^{-1}) is observed for the as-implanted samples (a) and (c) (refer to Figure 4.2), and not the post-anneal samples (b) and (d).

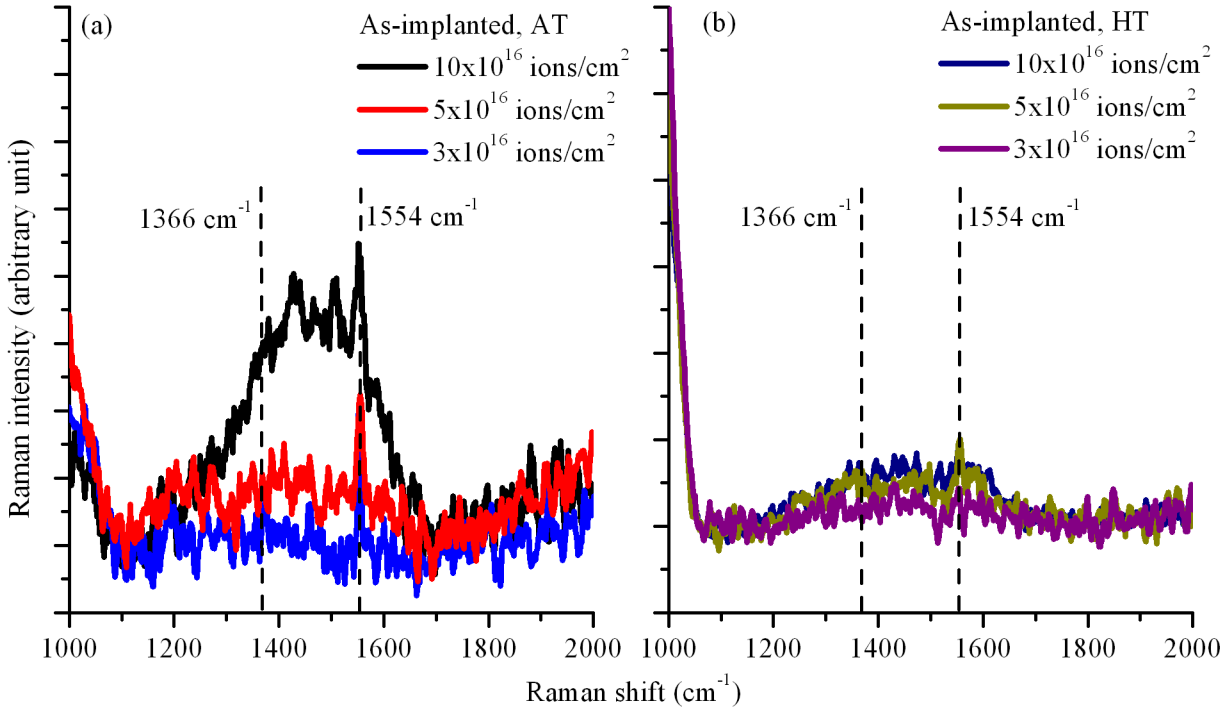

Figure 4.2 Raman spectra for as-implanted (a) AT and (b) HT C:Si, showing the carbon *D*- and *G*-bands between 1300 cm^{-1} and 1600 cm^{-1}. The reduced intensity of the carbon bands in the spectra for the HT samples shows more integration of C^+ after implantation, but the integration is not complete and further annealing is required to eliminate the carbon clusters. The elimination of the carbon clusters by post-implant annealing is shown in Figure 4.1.

4.2. Fourier-Transform Infrared Spectra

The FTIR spectra for the as-implanted and post-anneal C:Si samples are shown in Figure 4.3. Based on previous work, the SiC peak is expected at ~800 cm^{-1}. The peak height should increase with fluence until SiC saturation is reached, and the peak frequency may decrease with higher fluence as SiC crystallites grow in size due to more readily available carbon.

The SiC phonon peak is observed for all samples; in the AT C:Si samples the peak is weak and broad after implantation, and is shifted to lower energy due to the amorphous state of the material [71]. In the post-anneal C:Si, the SiC peak is sharpened and shifted to higher energy, as shown in Figure 4.4. This confirms that annealing enhances SiC crystal formation in the C:Si materials. A second peak appears after annealing, at ~1100 cm^{-1}, from the formation of a SiO_2 during the annealing process since the annealing environment is not entirely oxygen-free [55]. The FTIR measurements for the as-implanted HT samples have broadened, lower energy peaks than the post annealed samples. The peaks in the as-implanted HT C:Si are not as broad as for the AT samples. The change in SiC peak energy and sharpness after annealing is less pronounced in the HT samples as well; the *in situ* annealing treatment of the C:Si is an effective way to enhance SiC formation. The fluence of the implants is reflected by the peak intensity with smallest to largest peaks corresponding to lowest to highest fluence. The HT samples show smaller peak intensity than the AT samples since the carbon ions have a broadened distribution in the implanted region and the implanted ion concentration is lower.

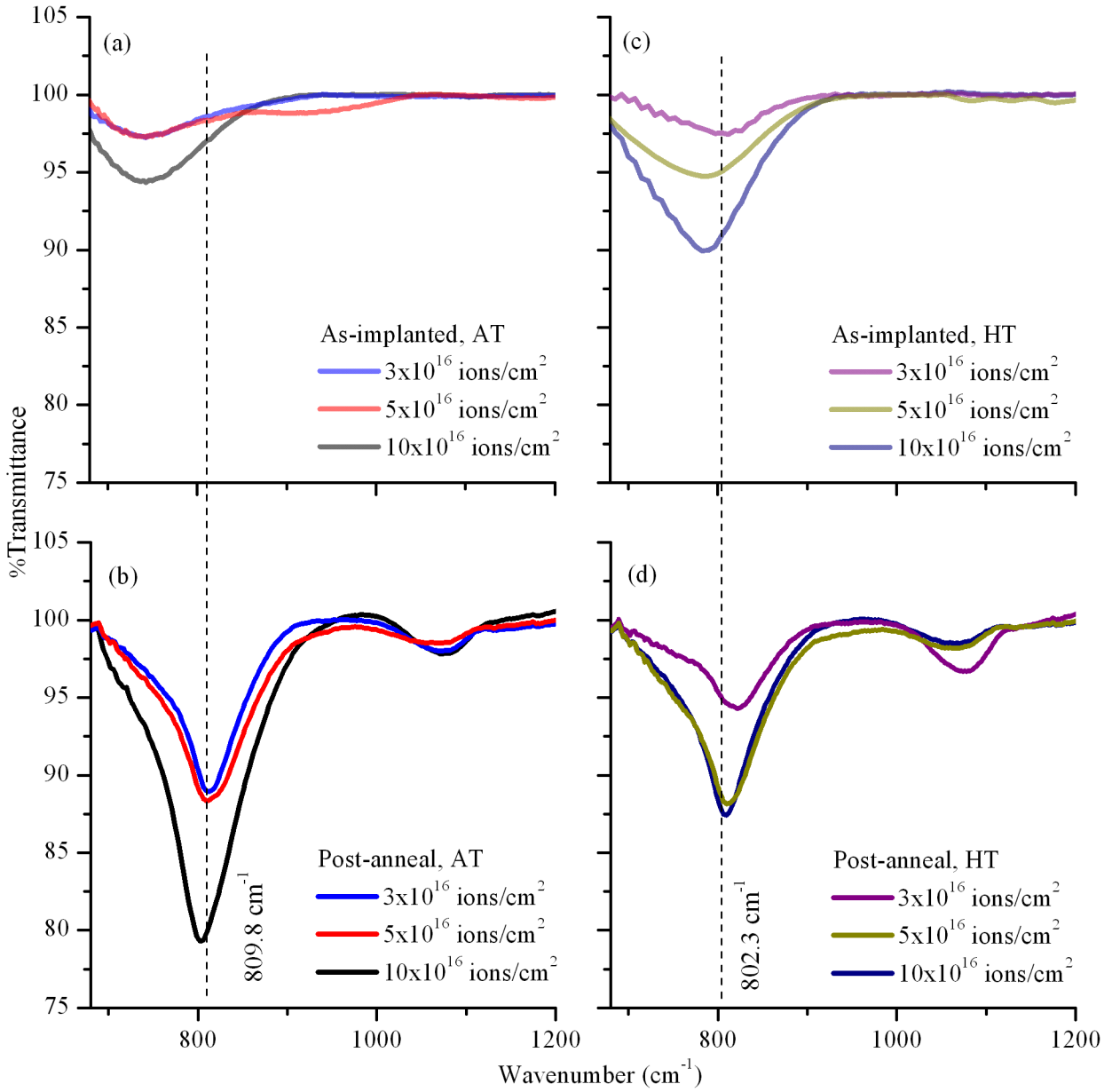

Figure 4.3 FTIR spectra of (a) as-implanted and (b) post-anneal AT C:Si, and of (c) as-implanted and (d) post-annealed HT C:Si. The SiC phonon is seen around 800 cm^{-1} and increases with ion fluence.

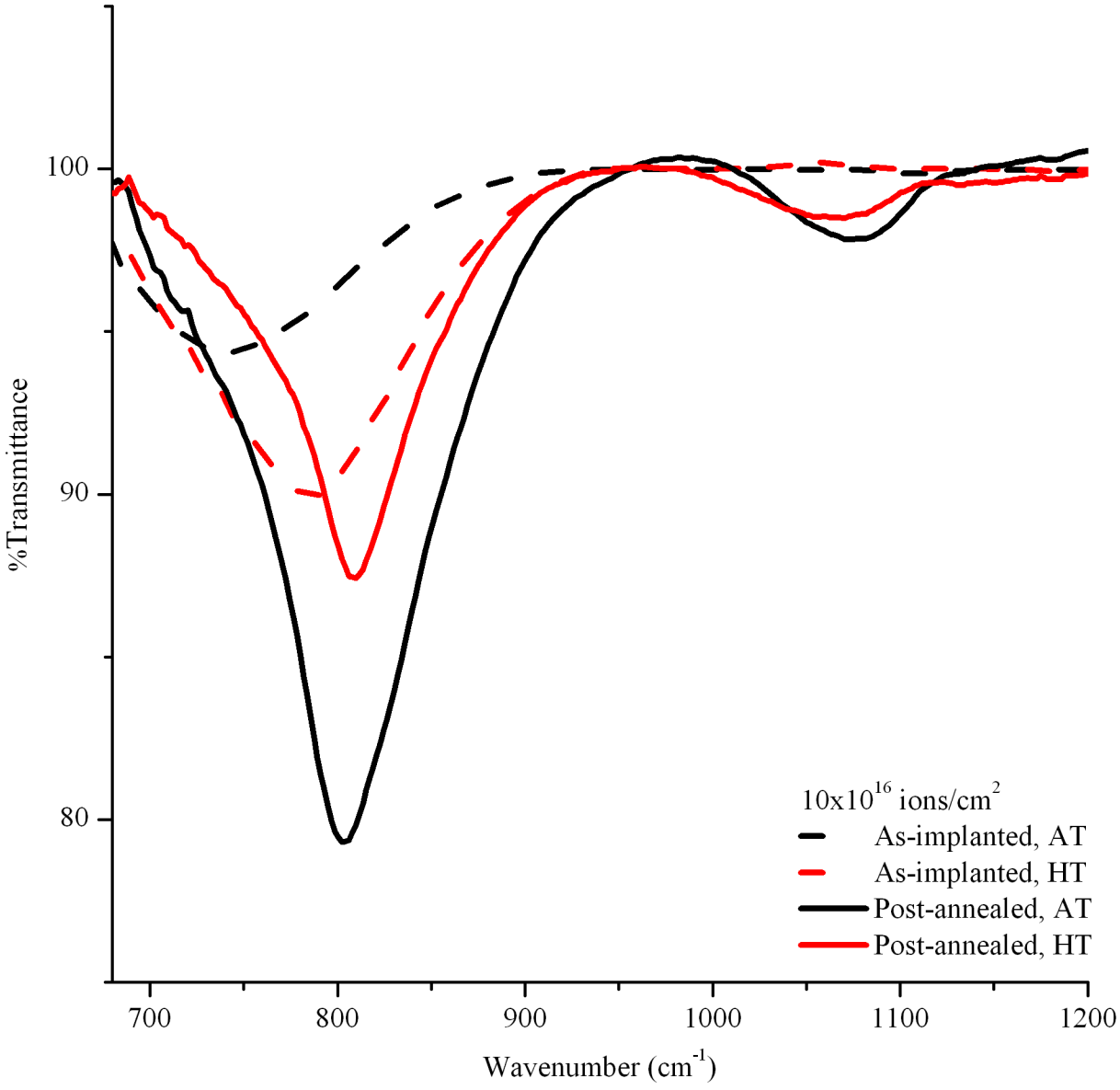

Figure 4.4 A comparison of FTIR data for as-implanted and annealed AT and HT C:Si. All samples are ion-implanted with ion fluence of 10×10^{16} ions/cm^2.

4.3. Grazing X-ray Diffraction

The crystal structure of the SiC within the C:Si samples is investigated using G-XRD. The low angle of incidence for the measurements makes it more sensitive to the thin implanted region. The G-XRD patterns are shown in Figure 4.5 for the highest fluence sample before and after annealing. Mercury software is used to simulate the XRD patterns for Si (516688-ICSD), 3C- (cubic) (1011031-ICSD) and 6H-SiC (hexagonal) (182362-ICSD) [157].

Due to the high cost of the TEM measurements, only two samples are measured: the post-anneal AT and HT highest fluence samples 10×10^{16} ions/cm^2. The lower fluence samples are expected to demonstrate similar structure. In the low fluence C:Si the concentration of C, and the amount and size of SiC inclusions is too low to be measured in a reasonable amount of time. The G-XRD pattern for as-implanted, AT C:Si show crystalline Si (111), (220) and (311) at $2\theta = 28°$, 47°, and 56°, and some hexagonal SiC (111) at 36°. The as-implanted HT C:Si shows little crystal structure, either because the reduced density of the heated target allows more complete amorphization or because the recrystallized regions are sputtered away at the high fluence. Annealing the C:Si results in recrystallization of the targets, the diffraction patterns for the AT targets have c-Si(111) at 36°, and 3C-SiC (111), (200), (220) and (311) at 39°, 45°, 65° and 78°, respectively. The HT targets show only polycrystalline 3C-SiC (111), (200), (220) and (311). The relative peak heights of the G-XRD measurements not the same as those predicted by the XRD model; this indicated preferential orientation of the crystal growth of the SiC and Si. The G-XRD results indicate that the annealing process enhances the formation of SiC and is necessary to reduce the damage caused by the implantation process. Heating the target during implantation enhances the formation of SiC.

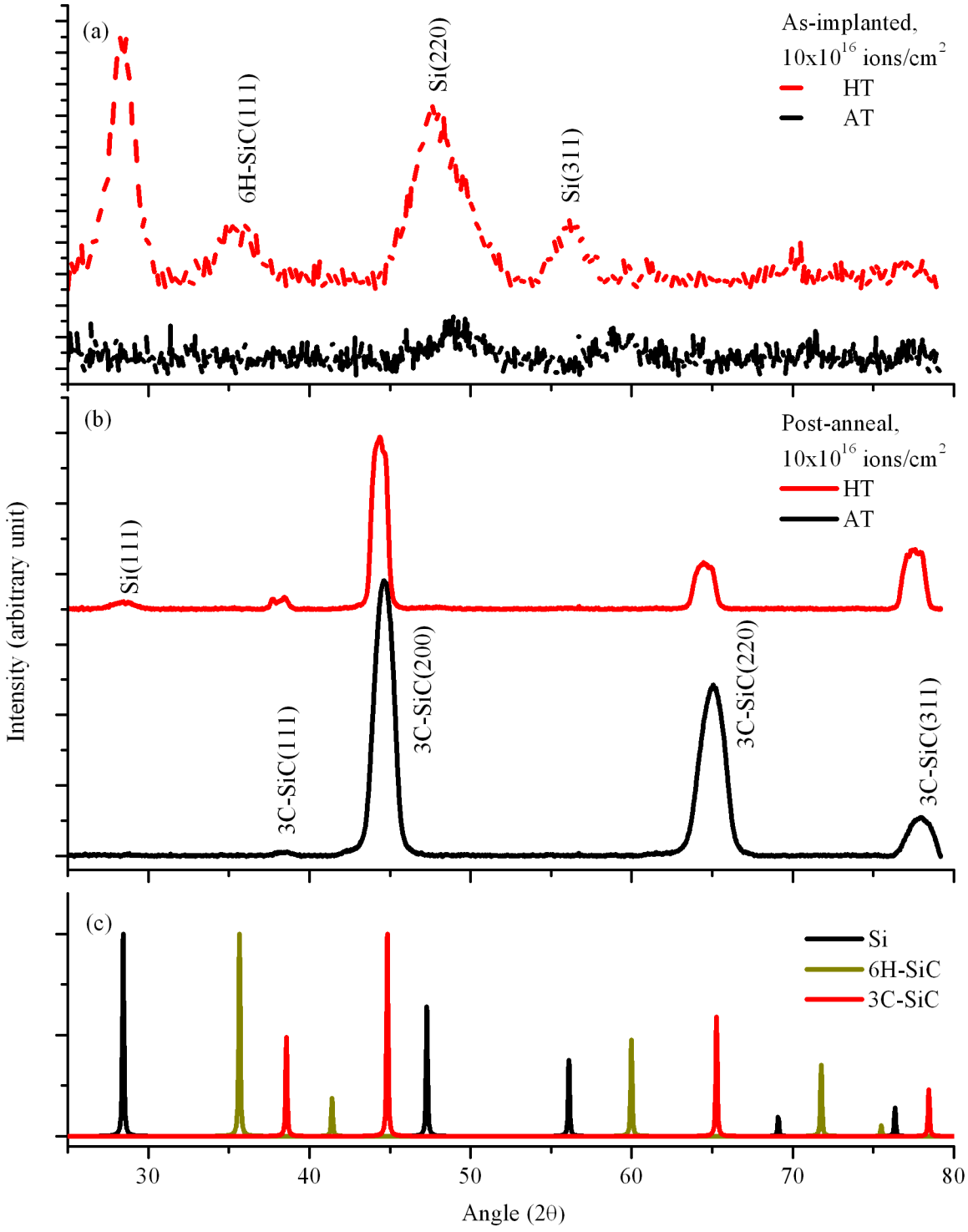

Figure 4.5 G-XRD for C:Si with 10×10^{16} ions/cm^2 before (a) and after (b) annealing treatment. The simulated diffraction patterns for Si, hexagonal and cubic SiC are shown in panel (c). Figure adapted from Purdy *et al.* 2015 , © 2015 IEEE [89].

4.4. Electron Energy Loss Spectra

The distribution of implanted carbon is measured alongside TEM imaging, using EELS. The EELS measurements for post-anneal AT and HT C:Si for 10×10^{16} ions/cm^2 are shown in Figure 4.6. These measurements show only the distribution of the carbon ions implanted into the sample, a measurement of the absolute concentration of carbon requires measurements of Si and O. The SRIM calculation for C^+ implanted into Si is shown here as well, the simulations do not include the annealing process, the comparison here is purely qualitative.

In the ion implant simulations, the density of the target is included in the calculations. For the AT samples the target density of Si is input as 2.33 g/cm^3, and for the HT samples is calculated using equation 3.9 to be 2.18 g/cm^3 [77]. The ion distribution for the AT samples yields a projected range (R_p) = 677 Å, and straggle Ω_R = 279 Å, for the HT samples, R_P = 720 Å and Ω_R= 257 Å. The damage to the target is calculated as the number of sputtered atoms, and the number of vacancies created in the target lattice for each implanted ion. For the AT samples these values are 0.472 sputtered ions/ion, and 305 vacancies/ion, and for the HT samples: 0.445 sputtered ions/ion and 159 vacancies/ion. The SRIM simulation indicates that the HT samples suffer less damage, the ions have a larger implantation depth, and wider distribution within the material. The EELS measurements for the post-anneal, AT sample shows agreement with the simulation; however the carbon distribution measured in the post-anneal HT samples is closer to the surface than predicted by the SRIM simulation. This is explained by the fact that the SRIM simulation does not include the recrystallization of Si (seen in TEM results) at the substrate interface during the high temperature implantation process. The broadened distribution of a fixed number of implanted ions in the HT samples is necessarily related to a reduction in the peak

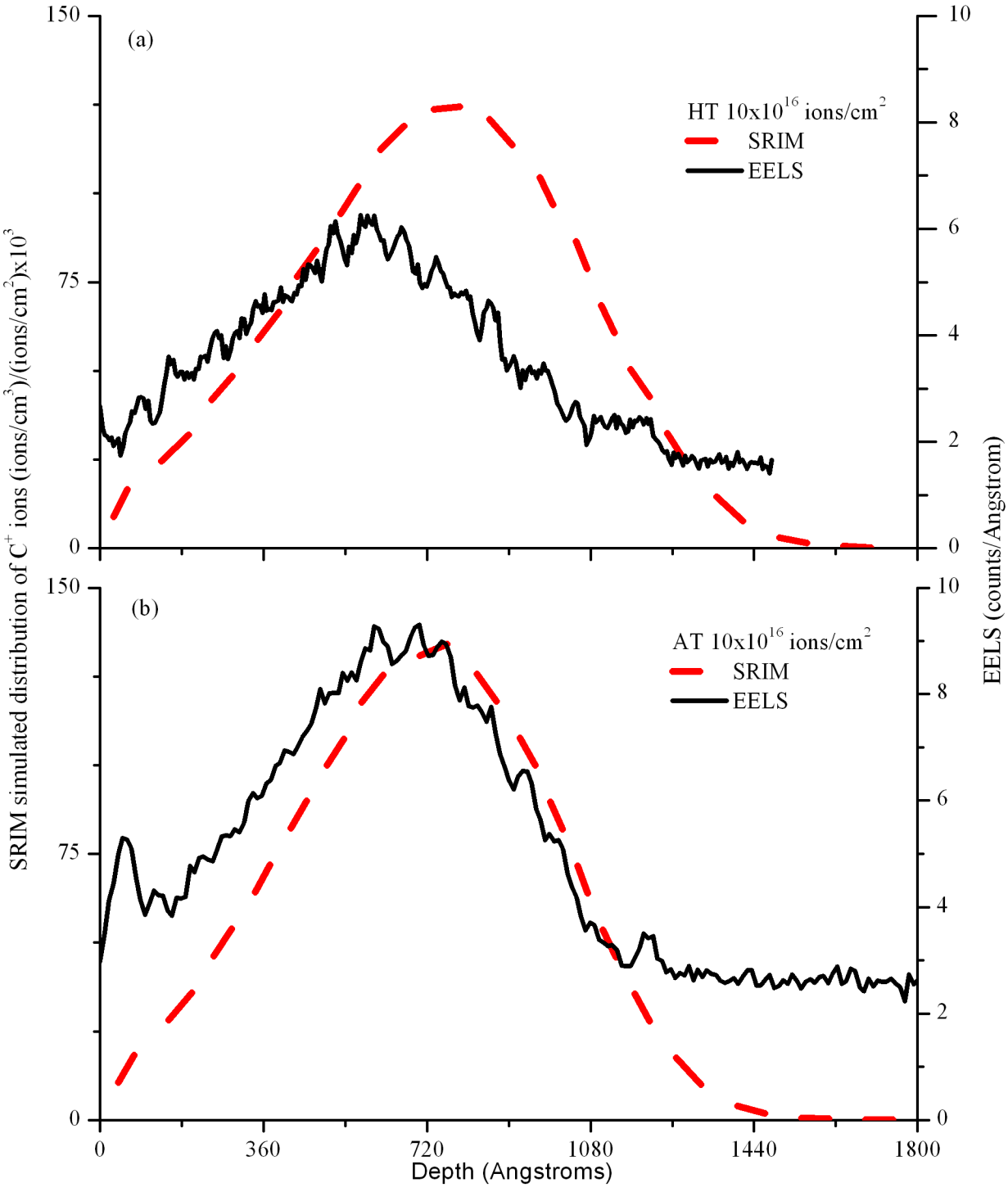

Figure 4.6 EELS measurement for post-annealed 10×10^{16} ions/cm^2 samples, compared to SRIM simulations for (a) HT and (b) AT C:Si. The y-axis scales are arbitrary, without EELS measurement of other elements the absolute relative concentration of carbon in the sample cannot be shown. Adapted from Purdy *et al.* 2015 , © 2015 IEEE [89].

concentration of the implanted carbon (broadened Gaussian curves with fixed area have reduced peak height). This results in a reduced SiC phonon peak compared to that of the AT samples.

4.5. Transmission Electron Microscopy Using High-Angle Annular Dark Field Imaging

The highest fluence AT and HT samples are chosen for TEM measurement of the C:Si materials, to mitigate the high cost of TEM measurements. The selection of samples was done before completion of the other analysis techniques, which indicate that the three fluence values should be expected to have varied physical features. The cross section of the implanted material is observed using HAADF-TEM, the high fluence AT and HT samples are compared in this section. The HAADF-TEM images of the 10×10^{16} ions/cm^2 post-anneal AT and HT samples after annealing are shown in Figure 4.7 and Figure 4.8. The image for the AT sample shows an amorphous layer containing a-Si, and nanoscale carbon-rich inclusions are observed in this region. Combined with the FTIR, Raman and G-XRD observations, we conclude that these inclusions are composed of SiC, with some crystalline order. The images for the HT samples show a similar layer, in addition to a polycrystalline layer of Si between the carbon-rich region and the substrate that does not appear in the AT samples [89]. Had TEM measurements been done on the other samples, the physical structure could be expected to be similar, where the low fluence samples would exhibit more c-Si with less complete amorphization of the target, and the mid-fluence samples might have fewer or smaller SiC inclusions.

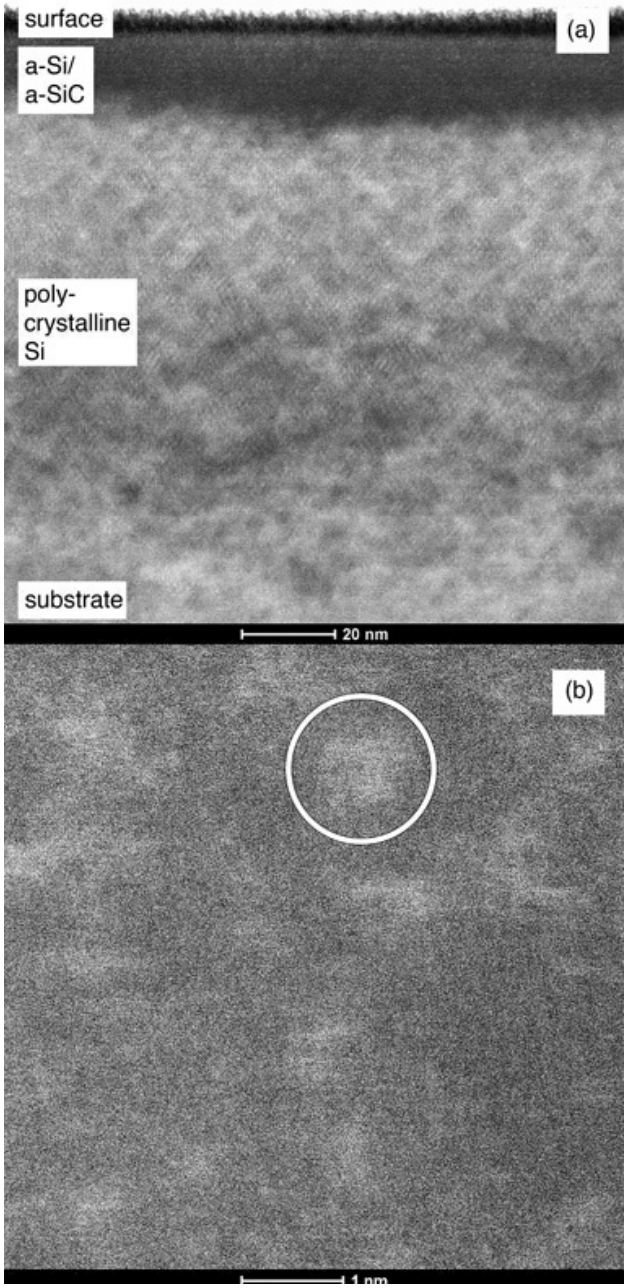

Figure 4.7 HAADF-TEM images of post-anneal HT C:Si implanted with 10×10^{16} ions/cm^2: (a) a multilayer structure with the same a-Si/a-SiC layer seen in the AT samples, as well as a polycrystalline Si layer on the c-Si substrate and a magnified portion of the a-Si/a-SiC layer, with carbon-rich Si inclusions (highlighted) ,© 2015 IEEE [89].

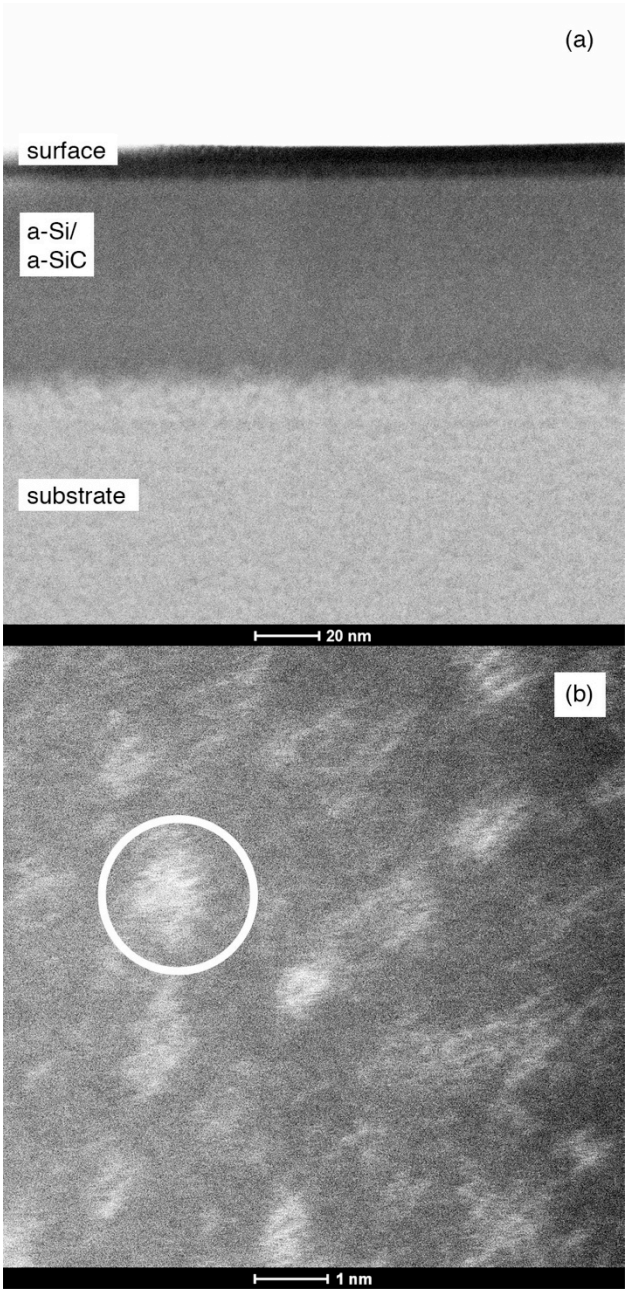

Figure 4.8 HAADF-TEM images of 10×10^{16} ions/cm^2 AT C:Si after annealing: (a) multilayer structure made up of a carbon-rich a-Si layer and the c-Si substrate and (b) a magnified section of the a-Si layer with carbon-rich Si inclusions (highlighted). The FTIR and G-XRD results indicate that the inclusions are made up of SiC, with some crystalline order. © 2015 IEEE [89].

4.6. Diode Characterization

The annealed C:Si is used to produce Schottky diodes by applying metal contacts onto the front and back surfaces of the processed wafer. The results of the diode characterization and analysis of the diode curves are presented in this section. The *I-V* curves for the diodes are collected between -12 to 15 V, and temperatures during diode testing are measured to vary from <20 to >60 °C despite the use of water cooling and refrigerated water circulation systems, seen in Figure 4.9.

4.6.1. Application of the Shockley Diode Model

The Shockley equation is applied to the forward bias *J-V* data, assuming that $V >> IR_{ser}$. The *J-V* curves for the HT and AT samples are shown in Figure 4.10. The reverse bias region shows no reverse breakdown of the diodes to -12 V. The slope of the AT samples decreases at high current (~3.5 A/cm^2), which might prove interesting to observe at higher current (beyond the capability of the power supply used in these measurements). The turn-on voltage, V_{on}, is determined by linear fit to the "off" and "on" regions of the forward-bias *J-V* curve, where these regions are chosen to be the largest subset of data points that yield the best linear fit. The ideality factor, n, and the saturation current, I_{sat}, are determined by applying an exponential best-fit of the form of the Shockley equation 2.5, simplified to equation 2.6. In cases where the diode exhibited non-linear behavior at high-current, a subset of the *J-V* data for each diode is used to obtain the diode parameters.

The Shockley equation shows acceptable fit with the data, and formally verifies the diode behavior of the devices. The lines of best-fit (of the form of equation 2.6) have coefficients of

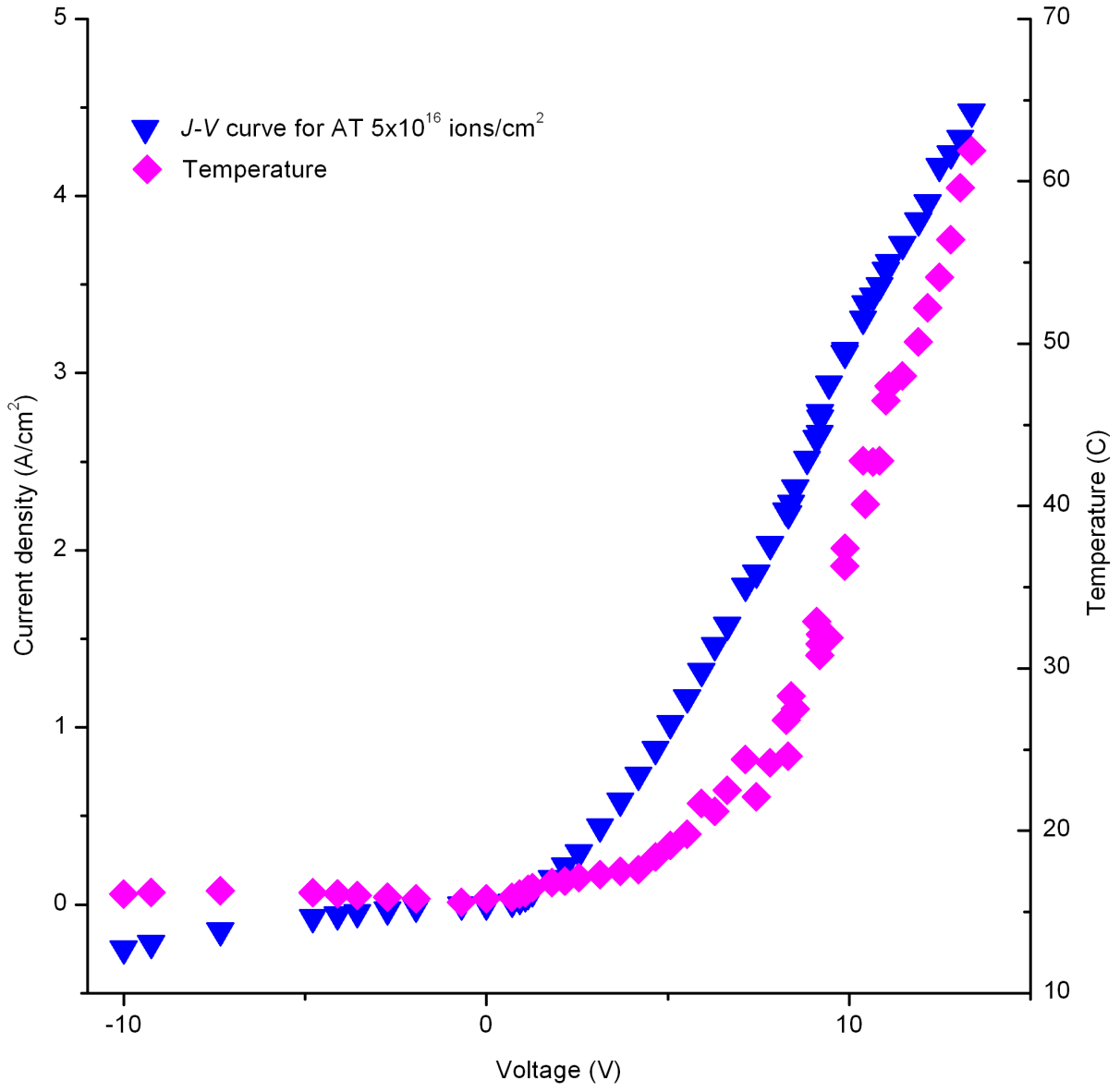

Figure 4.9 Current density – voltage curve for diode with coinciding temperature measurements during operation with water-cooling.

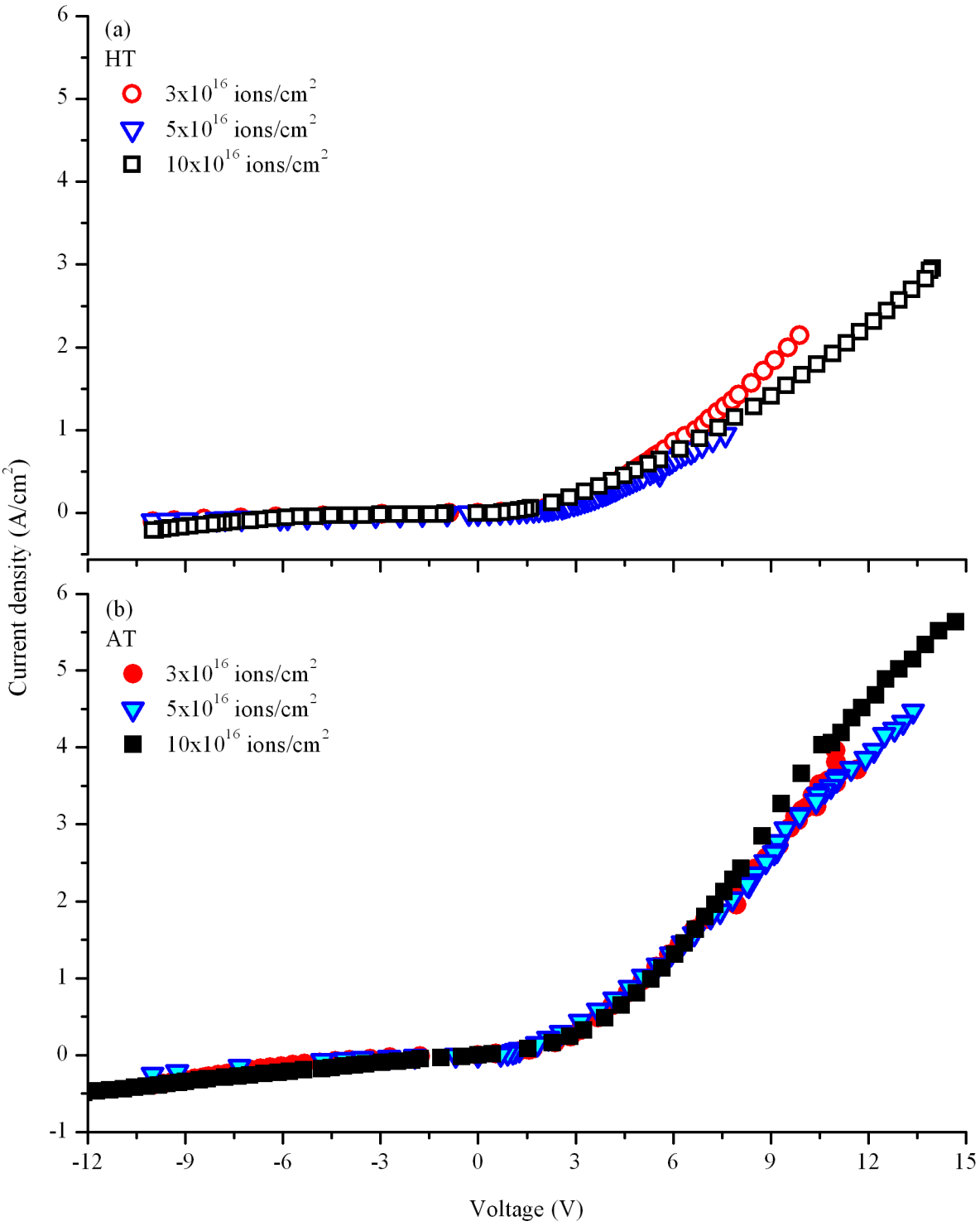

Figure 4.10 *J-V* curves for (a) HT and (b) AT diodes. No reverse-breakdown is observed to -12V.

determination (R^2) values of 0.971 to 0.996. The diode parameters are summarized in Table 4.1.Entering the diode parameters to equation 2.5 and taking the residual sum of squares (RSS) of the simulated and measured J-V curves serves to check the fit of the Shockley model: the RSS values range from 0.015 to 0.25. The large contact area, and the presence of the surface oxide layer are known to produce large ideality factors in diodes, such as those seen in the data presented in this thesis [99]. On the other hand, oxygen enhances luminescence, it affects device performance by contributing to non-ideal diode behavior [59]. The defect-rich implanted region and the non-uniform nature of the interface between the implanted layer and the substrate also contribute to high ideality factors [70], [99], [131].

Table 4.1: Diode parameters extracted from forward bias *J-V* data

Sample	**Turn-on voltage (V)**	**Ideality factor**	**Saturation current (A)**	**Barrier height (eV)**	**Goodness of fit,** R^2, RSS
Ambient temperature					
3×10^{16}	2.8 ± 0.6	188 ± 16	0.50 ± 0.09	0.3961 ± 0.0043	0.985, 0.24
5×10^{16}	2.6 ± 0.1	224.5 ± 5.8	0.72 ± 0.07	0.3981 ± 0.0025	0.996, 0.12
10×10^{16}	3.9 ± 0.1	185.4 ± 9.2	0.52 ± 0.06	0.3973 ± 0.0028	0.990, 0.015
High temperature					
3×10^{16}	3.2 ± 0.1	163.6 ± 6.3	0.23 ± 0.02	0.4137 ± 0.0022	0.983, 0.25
5×10^{16}	2.7 ± 0.1	124.3 ± 5.3	0.10 ± 0.01	0.4313 ± 0.0024	0.978, 0.082
10×10^{16}	2.9 ± 0.4	202.8 ± 8.7	0.23 ± 0.02	0.4296 ± 0.0026	0.971, 0.11

4.6.2. Diode Modeling Techniques for High Ideality Factor and Series Resistance

The application of the traditional method for fitting the Shockley equation to diode curves presents high ideality factors. Given the non-ideal behavior of the diodes seen in Figure 4.11, the accuracy of the exponential fitting of the J-V curve is reduced; a subset of the data with the highest coefficient of determination (R^2) is used. It is worth investigating diode fitting methods specifically for diodes with high ideality factors and series resistance [99]. A comparison of the application of the traditional and "optimal" methods of diode fitting for the samples under study is shown in Figure 4.12. Other methods have been developed in order to model diodes with high *n*, and are attempted with little success. The best approach, based on simplicity and sensitivity, according to Aubry *et al.* [99], is the Werner method where the differential conductance $G = dI/dV$ applied to the Shockley equation which yields:

$$\frac{dI}{dV} = \frac{q}{nkT}\left(1 - \frac{dI}{dV}R_{ser}\right) * I, \tag{4.1}$$

which is expressed as:

$$\frac{G}{I} = \frac{q}{nkT}(1 - GR_{ser}). \tag{4.2}$$

The data for a forward bias *I-V* data may be plotted as *G/I* vs. *G* where the slope and *y*-intercept yield values for R_{ser} and *n*. The application of this method to the current data does not present a plot with any reasonably linear behavior, future work may be designed for more effective application of this approach.

A second commonly used method uses the forward bias *J-V* measurements, where the series resistance (R_{ser}) is not neglected. The Shockley equation is then in its transcendental form,

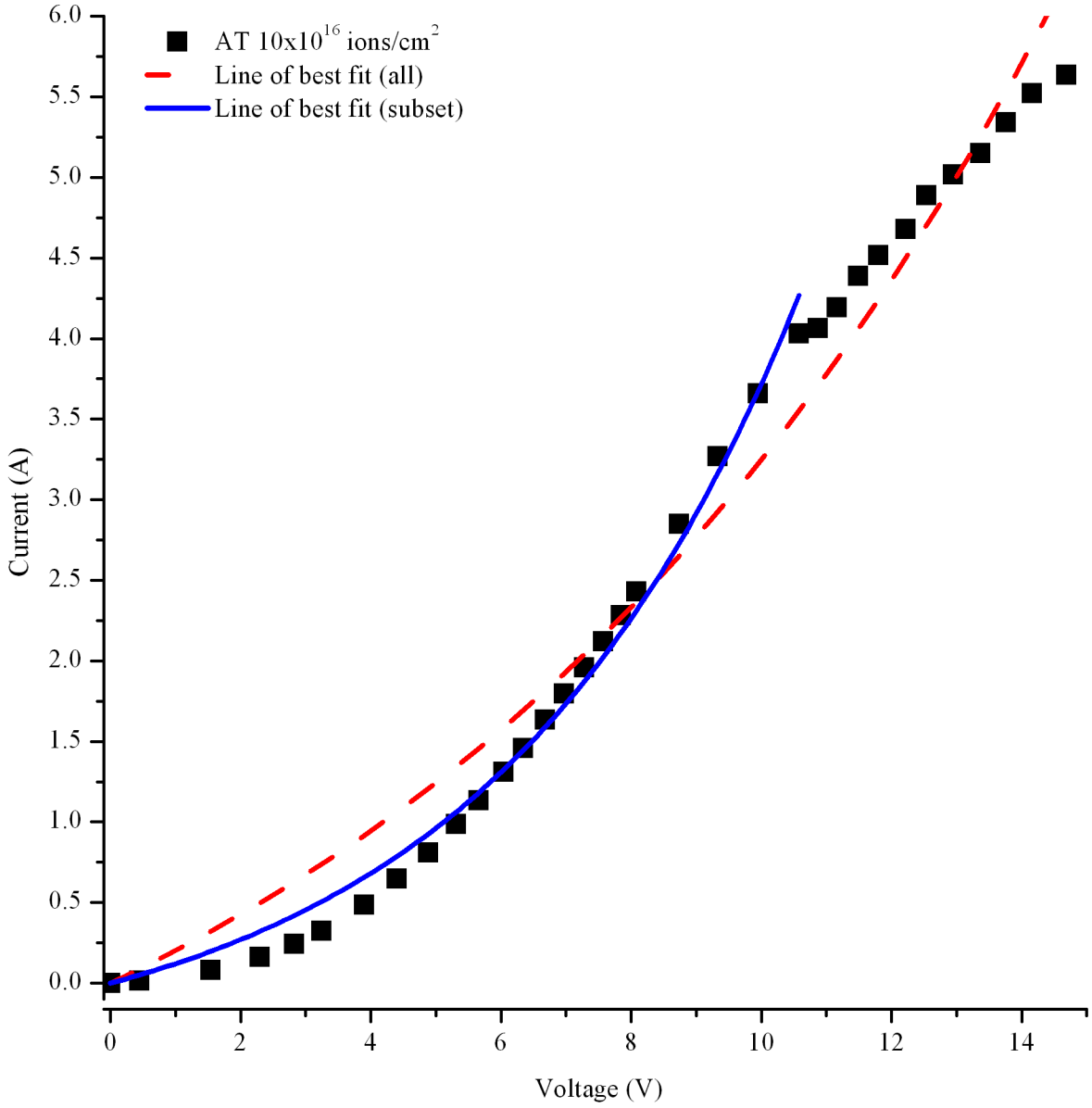

Figure 4.11 An exponential fit for a subset of *I-V* data presents a better model than a fit for the full data set that includes a change of slope in the high-power region of the *I-V* curve.

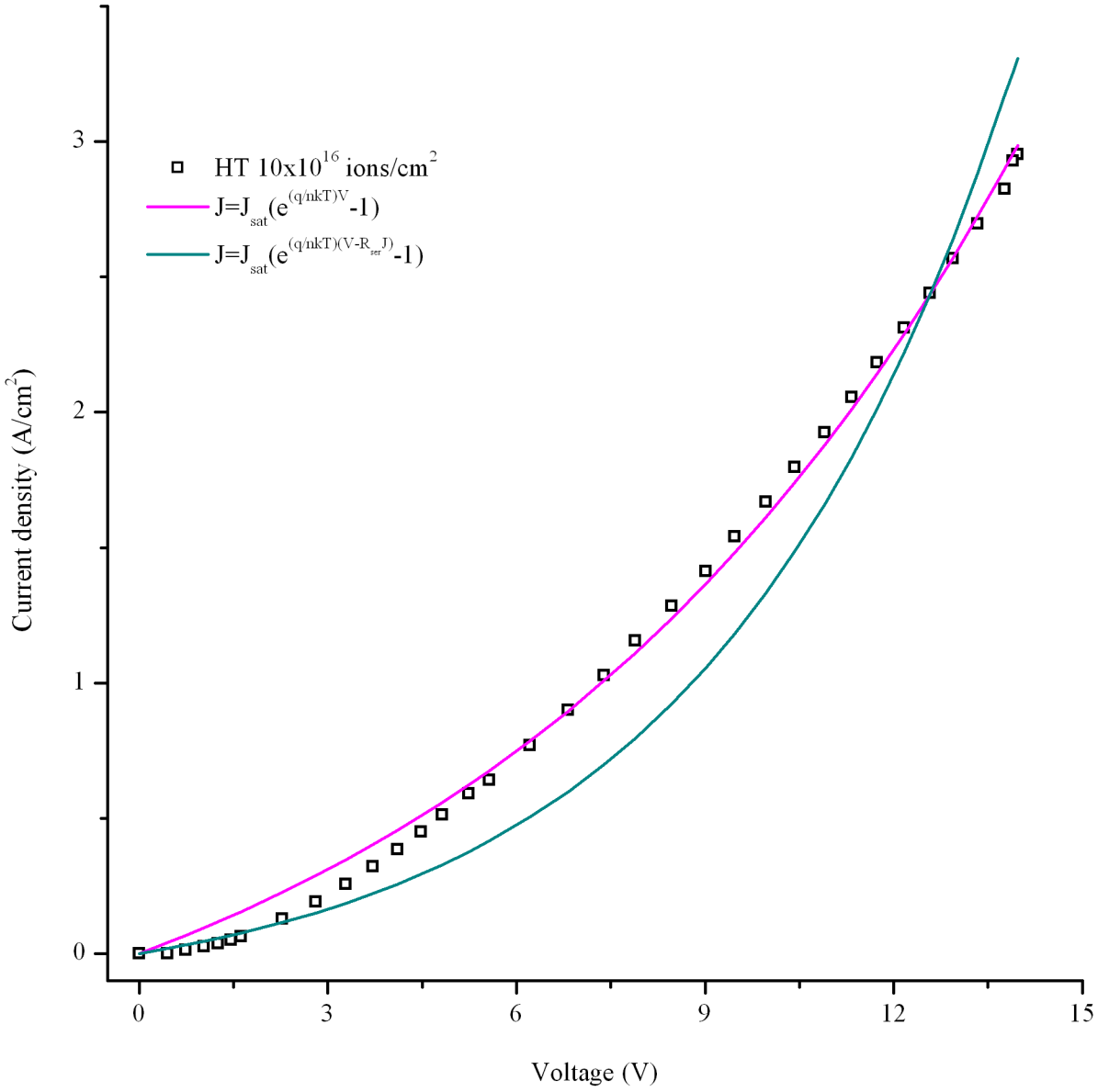

Figure 4.12 Comparison of diode fitting methods: exponential fit (pink) vs. including high ideality factor and series resistance (green).

and solutions may be found by iterative process: The ln$J$ vs. V_d (the voltage across the diode) plot is corrected for R_{ser} using $V_d = V - JR_{ser}$, and linear region is fit with a line that includes the largest number of data points with a "good fit." Attempts are made to maximize R_{ser}. The slope and y-intercept of the line of best-fit are used to calculate n and I_{sat}, respectively.

The application of this method to the measurements presented here is complicated by the large change in temperature during testing (<20 to >60 °C despite water cooling). The high

power used to drive the diodes results in Joule heating, with corresponding change in R_{ser}. Therefore guesses for the R_{ser} value are inaccurate for the complete data set. The method is modified to account for this. Assignment of a temperature threshold that could be considered "acceptable" would be arbitrary. Instead, the following is attempted:

1) A guess at R_{ser} is made using Ohm's law: $R_{ser} = dV/dI$, and this is used to form a plot ln$J$ vs. V-$R_{ser}J$.
2) A linear fit of a subset of the data is applied, the slope and y-intercept are used to calculate n and J_{sat}, as before.
3) The results for n and J_{sat} are used to generate a modeled curve, plotted against the J-V data.
4) The values of residual sum of squares (RSS) between the model and the data are calculated.
5) Repeat to find a minimum RSS value.

This procedure attempted for the HT 10×10^{16} ions/cm^2 diode yields n = 183 and J_{sat} = 0.20 A/cm^2 with RSS = 1.68. However, care must be taken with the modification discussed here. When using a finite set of data points, the line of best fit for similar subsets restricts the possible values for the slope and y-intercept, as demonstrated in Figure 4.13. Since smaller RSS values are achieved using an exponential fit to the traditional Shockley equation (ignoring R_{ser}), this method is applied to acquire the diode parameters for the diodes in this study. It is worth considering that the methods outlined by Aubry *et al.* for large values of n would be considered the preferable method in this case [99].

The use of the method outlined by Aubry *et al*. is useful in such devices where the series resistance is comparable to the voltage across the diode (i.e. in this particular device, V = 12 V, and JR_{ser} = 1.2 V, which does not satisfy the assumption to neglect R_{ser}) [99]. It is unsurprising that large-area diodes with an intact native oxide layer, fabricated from defect-rich material would have high R_{ser} and n. Any further study of such devices should include:

- Removing the native oxide layer and/or cleaning the surface of the diode before applying conductive contacts,
- More effective temperature monitoring and control. (Passive cooling is insufficient for the power and heat applied during these measurements).
- *J-T* and capacitance-voltage measurements in addition to *J-V* measurements for further analysis and verification.

Commercial, bench top diode testing platforms, and temperature control systems exist and may be used to enhance the collection of data and controlled study of devices fabricated from ion implanted materials.

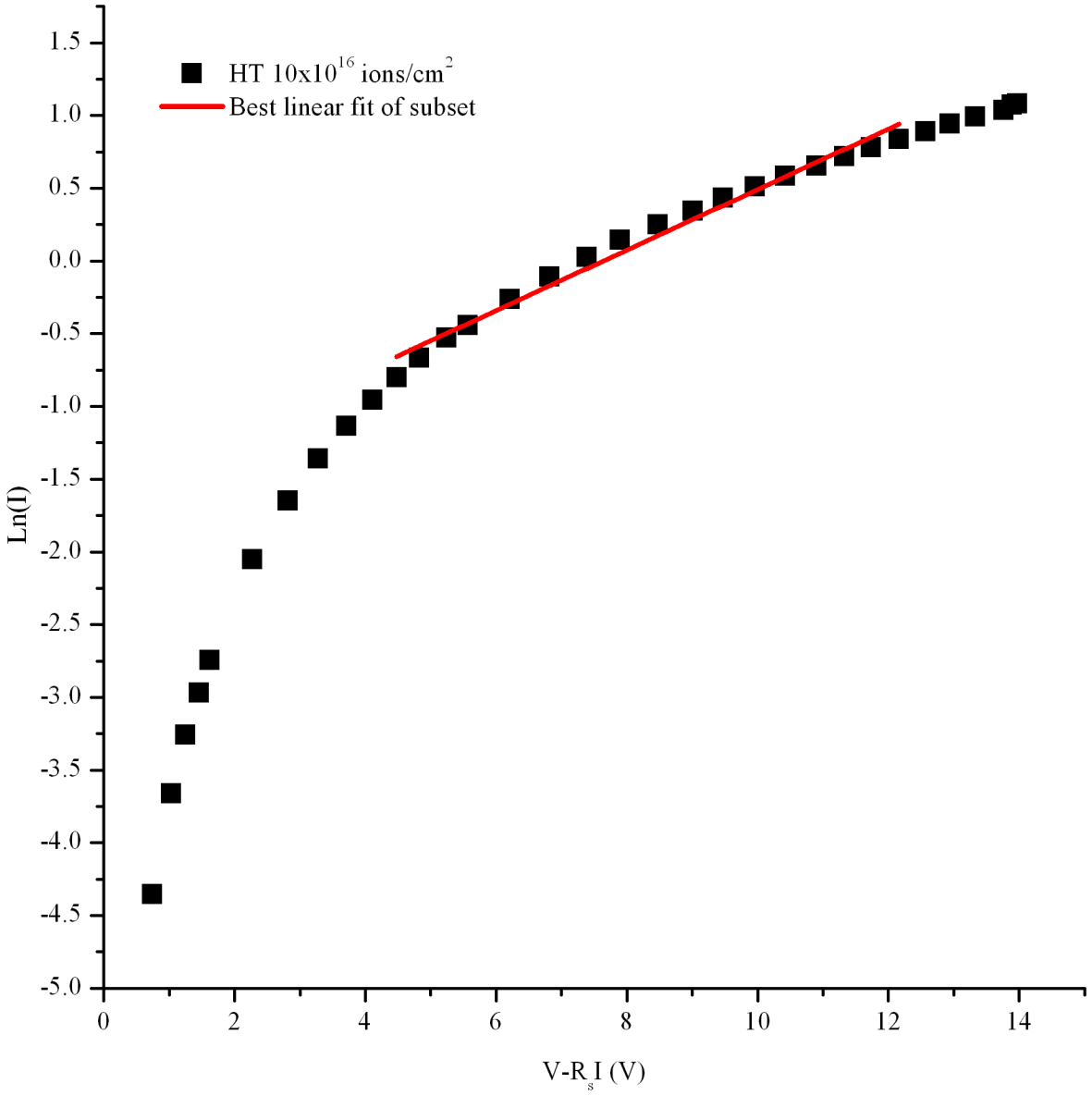

Figure 4.13 Demonstration of linear fit used to obtain n and ϕ_b, and fit to data resulting in the best RSS value. The intervals of the data points limit the possible slope and intercept values used for calculating the ideality factor and barrier height. If a different subset of data had been used, it would yield different results, but the accurate value might lie between the possible slope/intercept values from fitting to n number data points, or n+1 data points.

4.6.1. Added Sonication Step in Diode Fabrication

The diode fabrication and testing process reveals that the diodes exhibit non-ideal behavior, shown in Figure 4.14. It is believed that the inconsistent diode behavior is related to contact impurities due to surface contamination of the C:Si before coating, especially from debris related to the scoring and cleaving process. In order to remove possible surface contaminants, an additional processing step is investigated by *I-V* and FTIR measurement. After post-implant annealing, and before deposition of metal contacts, the treated wafers are cleaned in ethanol: acetone solution in a sonicator for 10 minutes. This is meant to remove debris from the cleaving process, and any contaminants from shipping, handling or exposure to atmosphere. The added step is shown to improve device performance with more stable *I-V* data shown in Figure 4.14. Further investigation by FTIR shows that there is no appreciable change in material composition after sonication, as seen in Figure 4.15. It is recommended that this practice be continued for future work. It is suggested that blowing with dry N_2 gas, removal of the oxide layer, or surface sputtering in vacuum before contact coating may also improve contact quality.

4.7. Electroluminescence Spectra

The light emitted from the samples under forward bias conditions is collected with varying current and is normalized for the area of the diode (assuming that the light emission is uniform on the surface covered by the testing platform). The red-orange luminescence is visible to the naked eye in a darkened room, and is bright enough to be captured with a handheld camera, shown in Figure 4.16. The luminescence spectra for the samples with increasing fluence

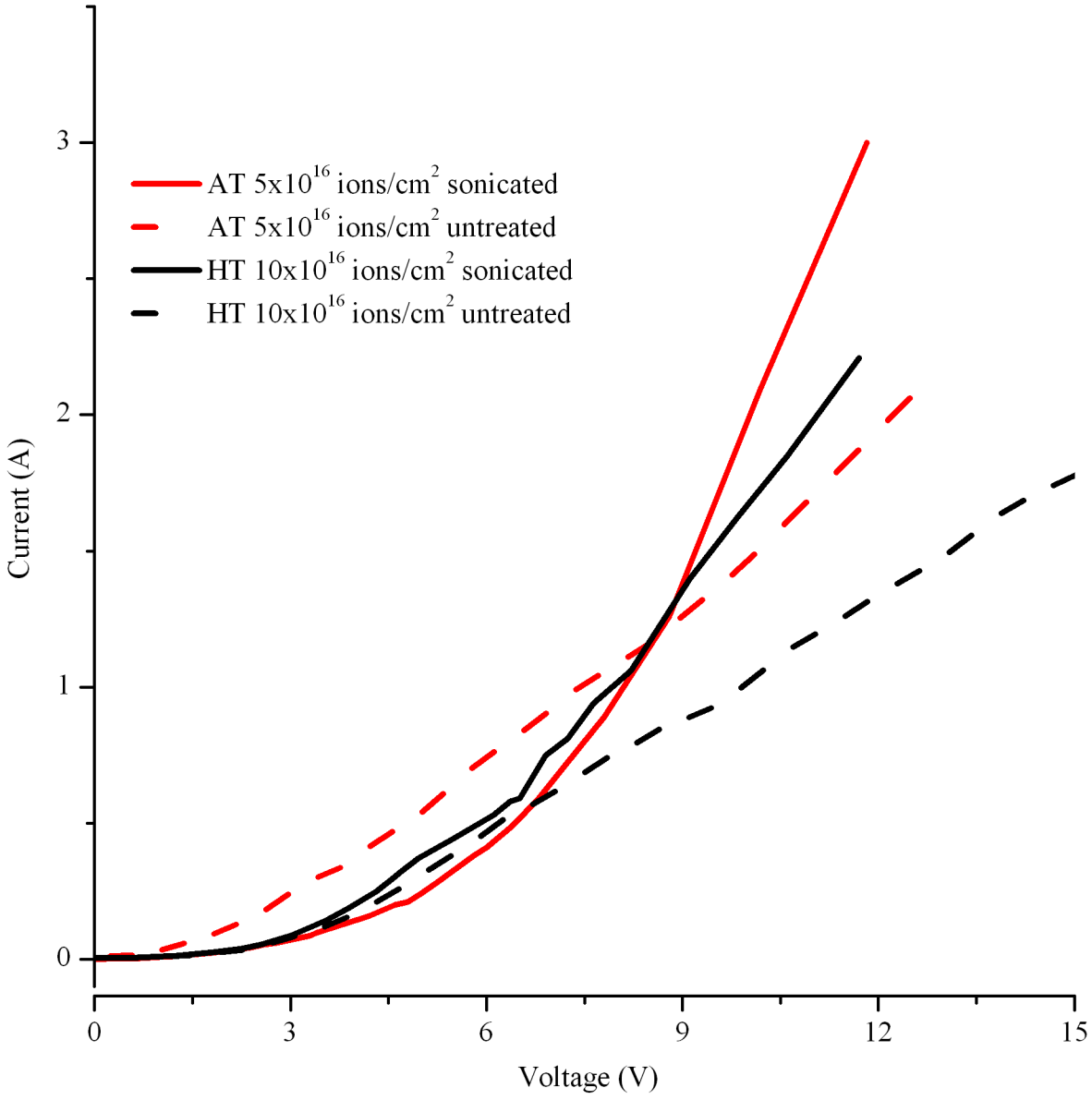

Figure 4.14 *I-V* curves for diodes with and without sonication before application of electrical contacts. The addition of the sonication process step results in the improvement of diode performance.

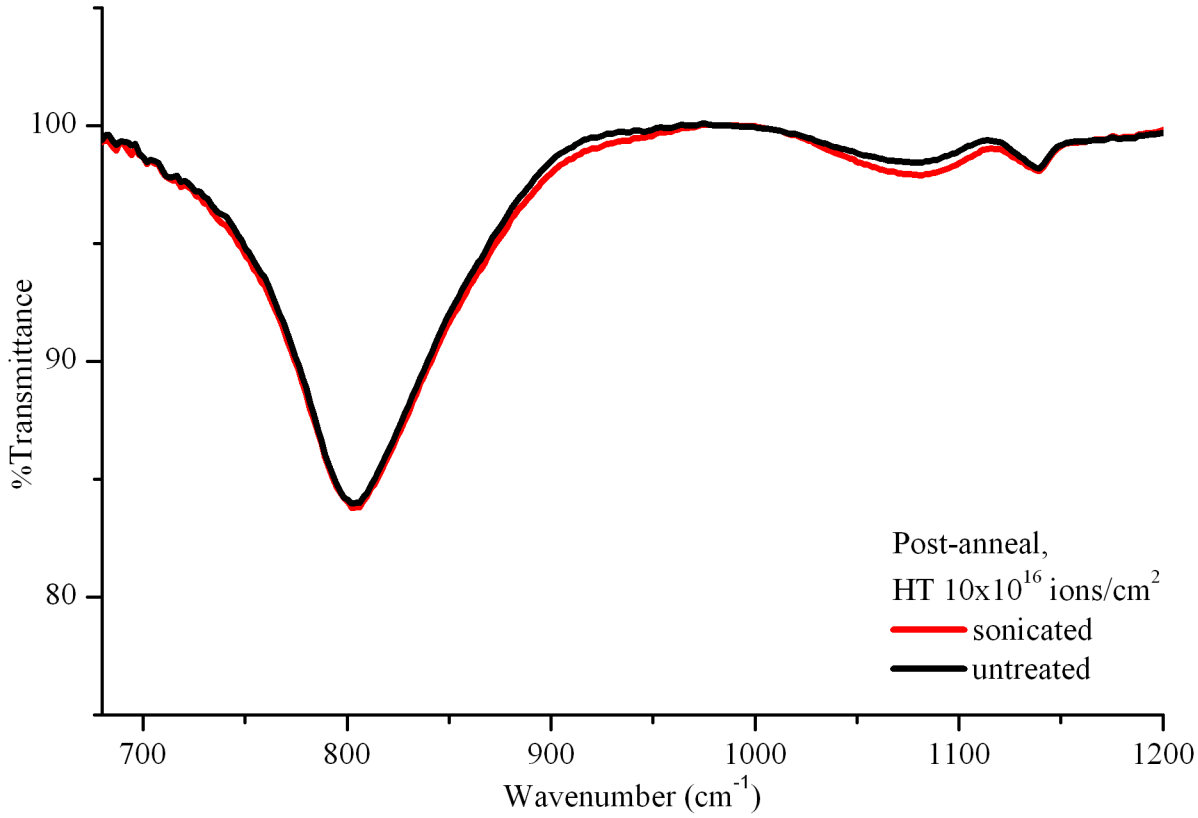

Figure 4.15 FTIR spectra for post-anneal HT 10×10^{16} ions/cm^2 C:Si material with and without sonication. The effect of sonication is negligible and does not change the composition of the sample.

Figure 4.16 A photograph of light emission from a diode fabricated from C:Si (AT 5×10^{16} ions/cm^2).

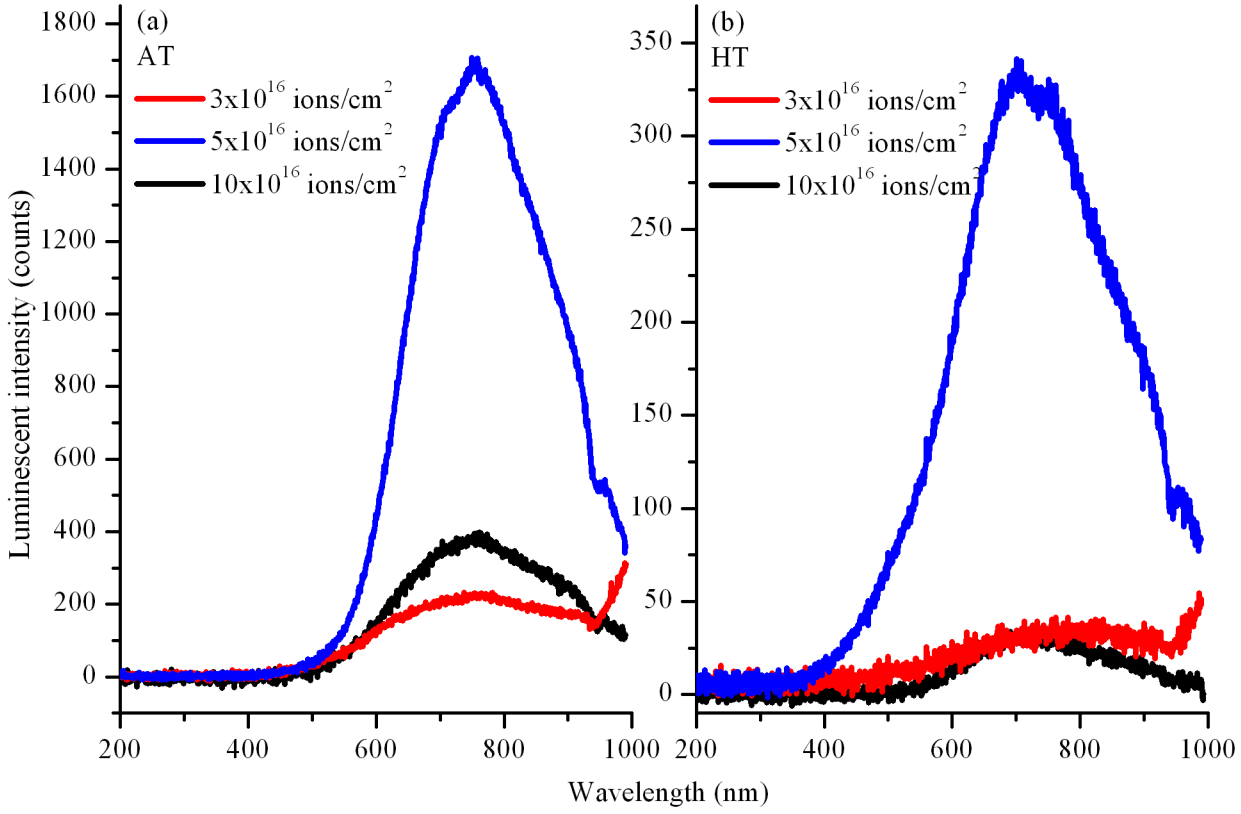

Figure 4.17 EL spectra of (a) AT and (b) HT samples at 3, 5, 10 × 10^{16} ions/cm^2 at 1.5 A/cm^2. The HT diodes have lower emission intensity than the AT diodes, the *in situ* annealing process reduces the amount of a-Si material that is the primary source of EL in these samples.

are presented in Figure 4.17. The luminescent intensity is taken as photons counted by the detector, which is not calibrated; however the measurements are taken at the same time (within a few hours) and may be used to indicate (not quantify) trends in the behavior of the devices.

In the EL spectra there appears to be some absorption at ~940 nm (1.32 eV), which is observed in other work using the same detector [90]. This behavior is taken to be a feature of the experiment system and not the samples; calibration of the detector is recommended, but is expensive and also affects other users. The luminescence of the C:Si LEDs increases with increasing applied current, as shown in Figure 4.18. The luminescence spectra are converted to energy units and fit with Gaussian peaks that correlate to luminescence bands seen in previous luminescence studies shown in Figure 4.19 and Figure 4.20. The Gaussian fit of the C:Si LED spectra shows several luminescent bands that are comparable to luminescence reported in literature on C:Si and p-Si materials, summarized in Table 4.2.

The most dominant luminescence feature appears to be p-Si, with contribution to the luminescence of all samples. The p-Si luminescence appears in the energy range from 1.39 to 1.77 eV. The luminescence peaks for the 3 and 5×10^{16} ions/cm^2 AT samples is fit with multiple peaks, and those attributed to p-Si are evenly spaced in energy. This has been observed in other ion-implanted Si materials, and is explained as a distribution in Si nanoparticle size [163]. An additional peak appears in the fit for the mid-fluence AT sample, at 1.84 eV, attributed to a-Si [164]. In the case of the lower fluence sample, the a-Si contribution is absent because the lower fluence does not amorphize the Si to the same degree as the mid-fluence sample. In fact, the low-fluence AT sample shows an additional luminescence peak at lower energy, which may be attributed to c-Si [89]. For the higher fluence sample, the amorphization is extended to such a

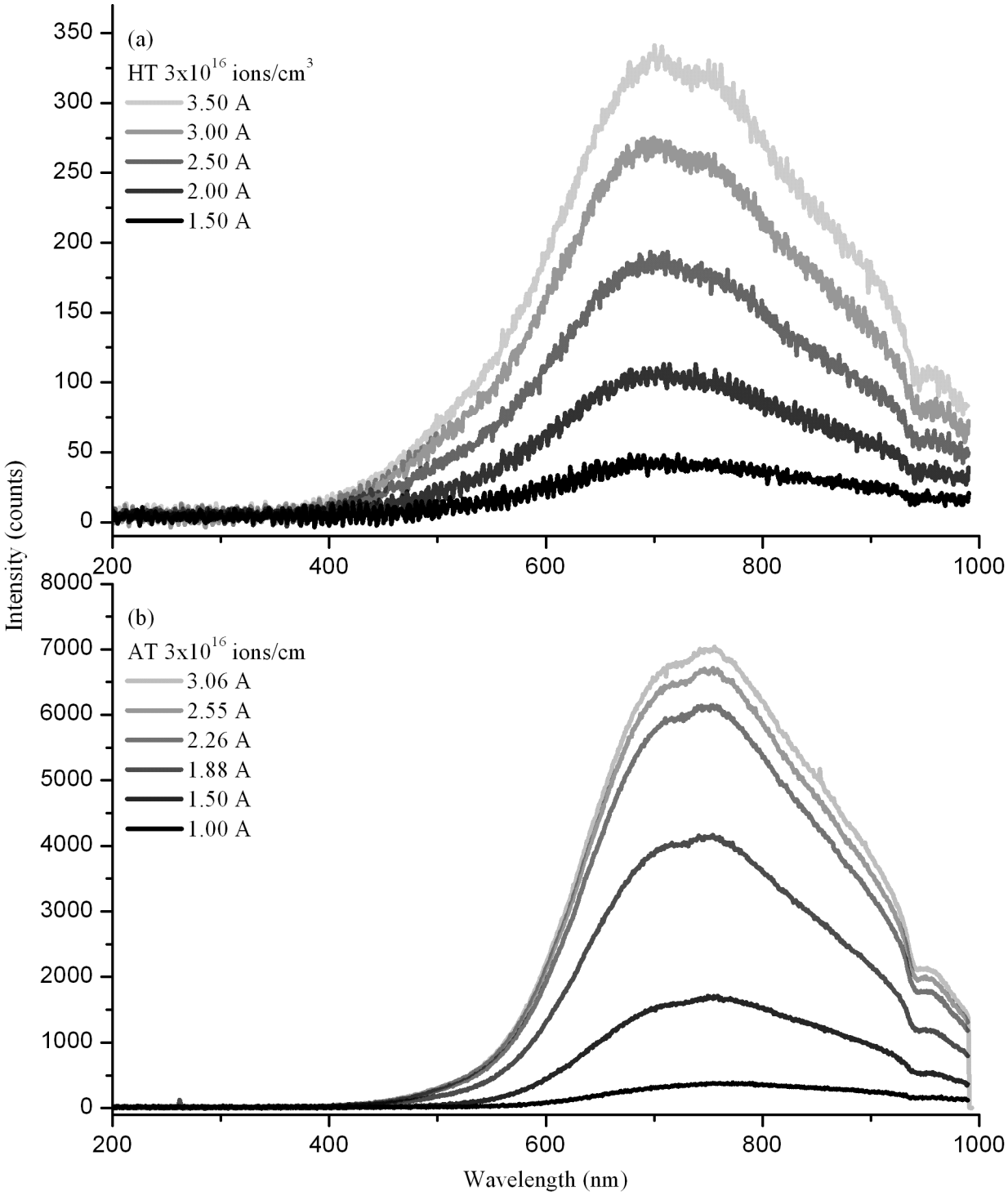

Figure 4.18 EL spectra for HT and AT samples shown with increasing applied current. The maximum luminescent intensity for the diode is beyond the output power limit of the power supply available for these experiments.

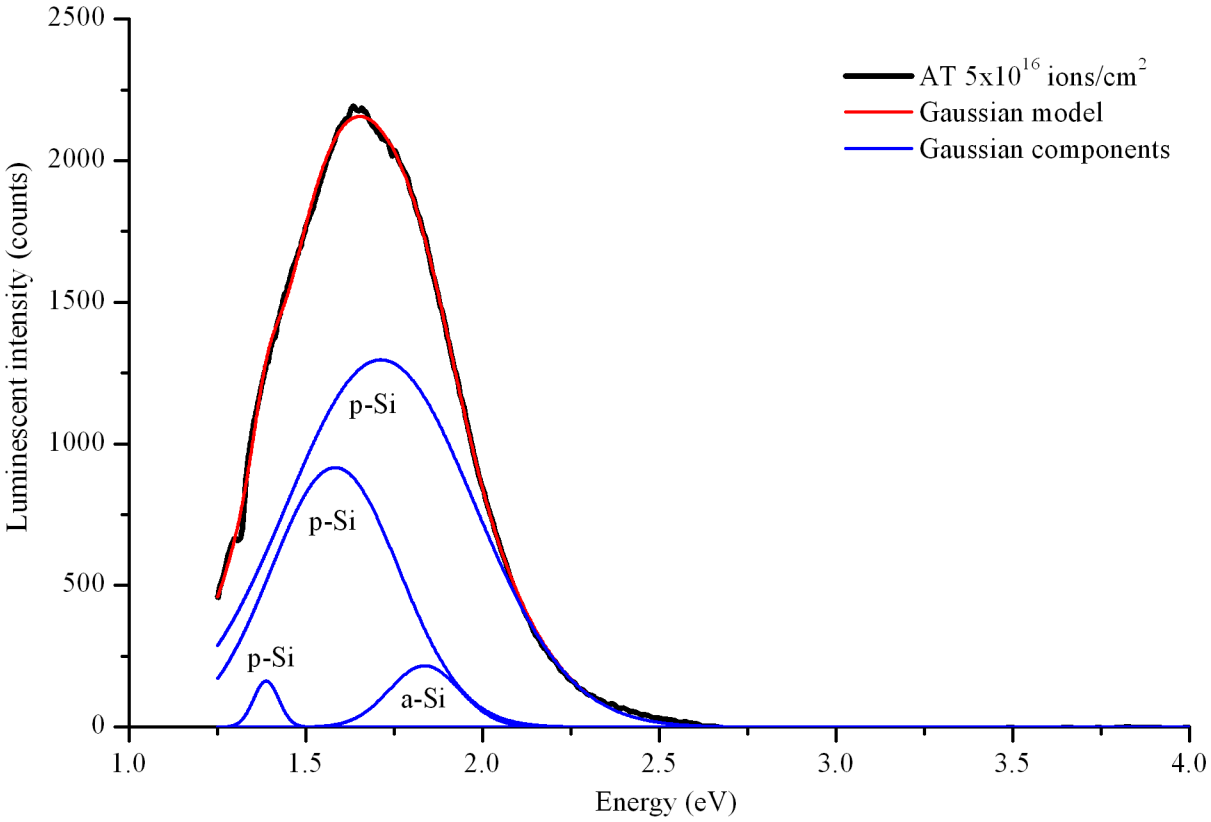

Figure 4.19 Gaussian fit of EL spectrum of AT 5 × 10^{16} ions/cm^2 diode at highest applied current. Luminescence is attributed to a-Si and a-Si.

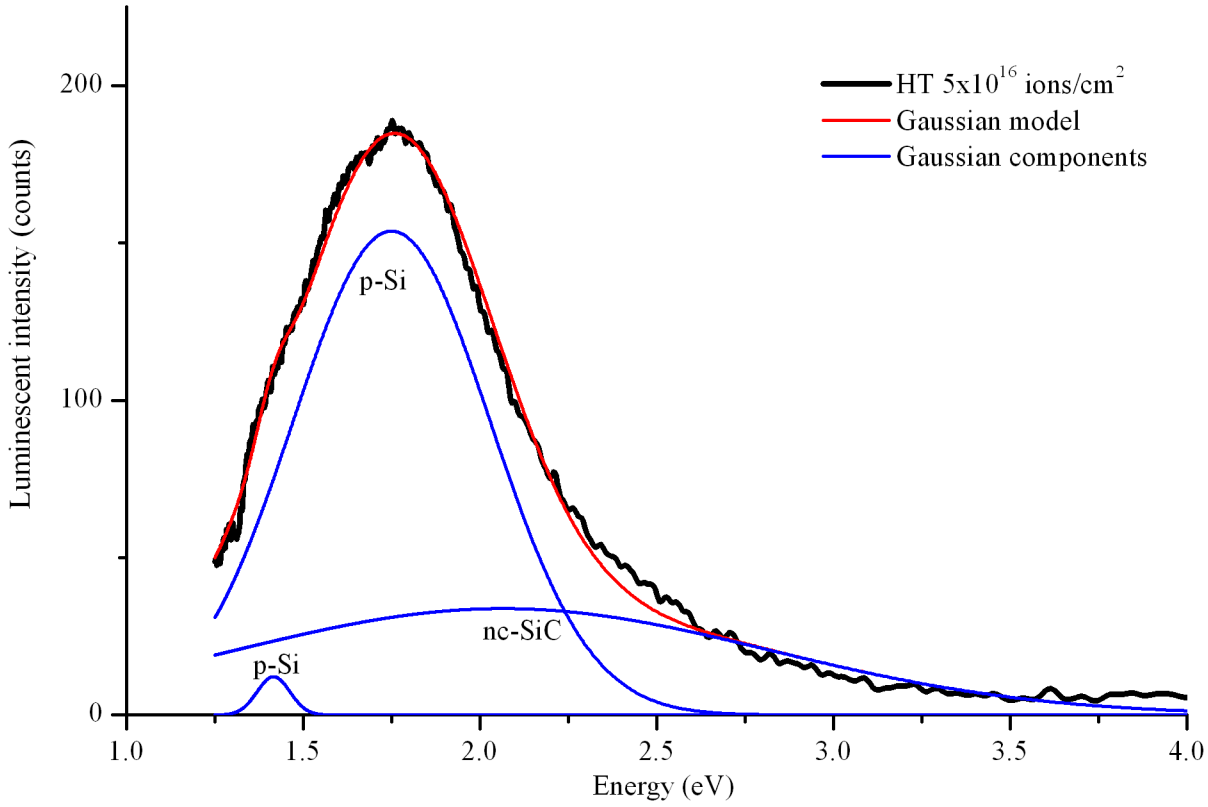

Figure 4.20 EL spectrum of HT 5 × 10^{16} ions/cm^2 diode with Gaussian fit. EL is attributed to a-Si, p-Si and p-SiC.

Table 4.2 EL peak fitting

Sample	EL peak eV (nm)	Mechanism	Reference
Ambient temperature			
3×10^{16}	1.56 (795)	p-Si	[75], [163]
	1.66 (747)	p-Si	[163]
5×10^{16}	1.39 (892)	p-Si	[75]
	1.59 (780)	p-Si	[163]
	1.70 (729)	p-Si	[113], [163]
	1.84 (674)	a-Si	[164]
10×10^{16}	1.67 (742)	p-Si	[163]
High temperature			
3×10^{16}	1.70 (729)	p-Si	[113], [163]
5×10^{16}	1.42 (873)	p-Si	[75], [163]
	1.75 (708)	p-Si	[113], [163]
	2.07 (599)	nc-SiC	[128], [165]
10×10^{16}	1.45 (855)	p-Si	[75], [163]
	1.77 (700)	p-Si	[113], [163], [165]
	1.93 (642)	defect states	[73], [166]

degree that little to no crystalline material remains to seed crystal growth. The recrystallization process during post-implant annealing produces a less of a distribution of nanoparticle size, resulting in the single p-Si peak observed. This is supported by the preferential crystallization observed in the G-XRD results, where the crystal orientation is not the same as the native target lattice, as had been observed in earlier work on C:Si [46].

The luminescence observed in the HT samples is also dominated by p-Si, and the same low energy peak (c-Si) is observed in the low-fluence sample. The mid-fluence HT sample demonstrates a luminescence band with peak at 2.07 eV, in the energy range of nano-crystalline SiC (nc-SiC) [128], [165]. The high-fluence HT samples has a peak at 1.93 eV, associated with defects in the implanted material [73], [166]. In the case of the HT implanted materials, the high fluence fully amorphizes the implanted region, including any SiC clusters that form during the implantation process, and the nc-SiC luminescence contribution is reduced with increasing fluence. Instead of nc-SiC luminescence, the luminescence in the high-fluence HT sample is related to defect states in the bad gap caused by the implanted impurities and remaining lattice damage from the implantation process.

The luminescence of the C:Si materials is dominated by p-Si, which is described by quantum confinement. For both AT and HT samples the EL peak height increases from low to mid fluence, and decreases with mid to high fluence. The low fluence C:Si produces EL with a c-Si component, demonstrating that there is less damage to the target, leaving some bulk c-Si intact. The high fluence C:Si also presents low EL peak height when compared with the mid-range fluence data. Using the SRIM calculations, the number of sputtered ions at HT is 0.445 sputtered atoms/implanted ion, for AT the value is 0.472 sputtered atoms/implanted ion [89]. The

medium fluence samples present the highest luminescent intensity. The optimal fluence for high luminescence at 20 kV C:Si must then be between 3 and 10×10^{16} ions/cm^2, which is consistent with previous work on fluence of C:Si and concentrations of implanted carbon [47], [56]. The FTIR results for the mid and high-fluence samples indicates a plateau in the SiC phonon peak height, however the high fluence implantation process has over-extended the amorphization of the C:Si, and this reduces the EL peak in the high fluence C:Si. The reduced EL peak height results from the competition between luminescence effects and non-radiative recombination with the higher population of defect sites.

The fabrication of LEDs from C:Si synthesized at low energy and high fluence is successful at both AT and HT implantation conditions. The AT implanted C:Si shows higher luminescent intensity, and the HT samples show luminescence at higher energy, with some contribution from SiC [89]. This work demonstrates that the luminescence of the C:Si material reaches a maximum and then decreases with increasing fluence. This indicates that competing mechanisms between luminescent recombination against non-luminescent recombination at defect sites limits the luminescent intensity. Comparing the EL data and TEM images, the Si nanoparticles that would contribute to luminescence are located in the amorphous region of the implanted layer. In the HT samples this layer is reduced in size, where Si recrystallization is enhanced by the HT implantation conditions; the luminescence from the Si nanoparticles is also reduced in these samples.

CHAPTER 5

CONCLUSIONS AND FUTURE WORK

The focus of the work presented here is on light-emitting devices fabricated with a synthesis technique

- That can be incorporated to large scale manufacturing using existing technologies.
- Using non-toxic materials.
- Without wafer bonding as with III-V semiconductors.

Carbon ion implantation into silicon is one method used to synthesize SiC, a known luminescent material and high-power semiconductor. Using ion implantation, the amount of carbon implanted into the target is well controlled, and the synthesis technique is already used in current manufacturing techniques. Previous work using C:Si demonstrated that the ion implantation technique results in damage to the treated wafer that both contributes to the luminescence and inhibits device performance because of the non-uniform interface between the implanted region and the substrate. The goals for the work presented here is to use low-energy implantation in order to mitigate this effect. Implantation into heated targets is investigated as a way to further mitigate the damage in the materials. Fabricating LEDs tests the application of the C:Si material for Si photonics. The material properties and luminescence mechanisms of the low-energy implanted C:Si is investigated and discussed in detail in Chapter 4.

5.1. Results of Characterization

Low-energy carbon ion implantation to silicon followed by thermal annealing yields thin, multi-layer a-Si films with carbon-rich inclusions and polycrystalline Si. Measurement of Raman

and FTIR spectra confirm complete formation of SiC in the C:Si. The inclusions are observed by TEM to be nanoscale in size, and have amorphous and some crystalline composition. The embedded SiC clusters, and the recrystallized Si have some crystalline order, confirmed by G-XRD; the orientation of these crystals is not necessarily aligned with the substrate. The ion implantation is well modeled by the SRIM suite of software, as confirmed by EELS measurement. The carbon ion distribution for the HT implantation is seen to be shifted towards the surface of the C:Si, with a re-crystallized layer of Si at the interface of the substrate. Heating the target during implantation is seen to enhance formation of SiC and recrystallization of Si in C:Si materials. Increasing fluence of C^+ results in C—C bond formation, which is reduced or eliminated by post-implant annealing. Post-implant annealing also promotes re-crystallization of the damaged Si material. The result of the C:Si synthesis after post-implant annealing is a polycrystalline Si layer, a polycrystalline/amorphous Si and SiC layer in both HT and AT samples, the HT sample has an additional re-crystallized Si layer beneath the carbon-rich region.

Light-emitting diodes are fabricated from the post-annealed C:Si material. The use of a sonication step to remove debris and impurities from the surface of the samples is shown to enhance the stability of the LED *I-V* curves. The LEDs function as Schottky diodes with visible orange-red luminescence. The EL mechanisms is primarily nanocrystalline silicon formed by the implantation and annealing process; it is the same luminescence as observed in pervious studies of p-Si luminescence. The luminescence spectra of the LEDs fabricated from the HT C:Si show some contribution from a-SiC. The AT LEDs demonstrate a change in the slope of the *I-V* curve at high power, which does not appear the HT LEDs up to 12 V. Higher doses of carbon into heated targets would enhance the luminescence from embedded SiC, however this is opposed by

the low-energy, high sputtering rate of the experiments discussed in this thesis. Implantation at higher energy implantation should be used for higher fluence C:Si.

5.2. Future Work

Target heating during implantation is attempted in this work in order to mitigate damage and defects in the synthesized material.. The practice of target heating may be realized by the use of an electric heater or by illumination of the target [167].

The use of sonication of the C:Si wafers, before application of the electrical contacts, is tested for effect on material characteristics and on LED performance. It is shown to produce more accurate *I-V* data. Surface cleaning such as this is recommended for future work on any coating on ion-implanted materials. In cases where the use of liquid is undesirable, surface sputtering or blowing with dry gas could prove effective. Furthermore, removing the native oxide layer before application of electrodes will reduce the LED ideality factor.

The *I-V* data that is presented in this thesis is limited by time, temperature control, and temperature measurement. The use of an automated *I-V* sweeping system would generate more data points in a shorter period of time. The testing bed may be enhanced by addition of a temperature sensor near the sample, and the use of a temperature controller to heat the sample at low driving power and cool the sample at high driving power instead of relying on passive cooling. The use of temperature control experiments would contribute current-temperature measurements that can be used to calculate and verify the ideality factor, saturation current and series resistance [99]. Researchers are encouraged to read Aubry *et al.* on modeling devices with high ideality factors when designing experiments on devices made with ion implanted materials [99].

5.3. Conclusion

Silicon-based LEDs are successfully fabricated with visible red-orange light. The brightness of the devices is associated with an optimal fluence, which is limited by the amount of defects induced by the synthesis process, and sputtering of the surface. The existence of an optimal dose for SiC formation is also observed by Poudel *et al.*, and Dibaji *et al.* [47], [56]. The luminescence is associated with p-Si, a-Si and a-SiC. The defects induced by the implantation technique interfere with device performance and are mitigated by target heating during the implantation process, and post-implant thermal annealing. Target heating of the HT samples to 400 °C, and post-annealing treatment at 1000 °C of both AT and HT samples results in enhancement of SiC formation and recrystallization of Si. The HT samples show reduced luminescent intensity, and a smaller a-Si/p-Si region, but the mid-fluence sample produces luminescence with a SiC contribution. A wider implant region with multiple energy implant, and implantation at higher energy will help to increase the amount of SiC in the C:Si that will increase the luminescence from SiC and modify the emission spectrum towards higher energy emission. The degree of crystallization of the C:Si is an important consideration for the fabrication of C:Si LEDs, a high concentration of nanoparticles in the implanted region, and the composition of those particles are governing factors in the luminescence wavelength and intensity. Oostra et al. also pointed out that the quality of the interface between the implanted region and the substrate affects the performance of diodes fabricated from C:Si [70].

REFERENCES

[1] J. M. Tendler, J. S. Dodson, J. S. Fields, H. Le, and B. Sinharoy, "System Microarchitecture," *IBM J. Res. Dev.*, vol. 46, no. 1, pp. 5–25, 2002.

[2] R. Merritt, "CPU designers debate multi-core future," *eetimes*, 2008. [Online]. Available: http://eetimes.com/General/PrintView/4076123.

[3] T. Baehr-jones, T. Pinguet, P. Lo Guo-qiang, S. Danziger, D. Prather, and M. Hochberg, "Myths and rumours of silicon photonics," *Nat. Photonics*, vol. 6, no. April, pp. 6–8, 2012.

[4] W. N. Ye and Y. Xiong, "Review of silicon photonics: history and recent advances," *J. Mod. Opt.*, vol. 60, no. 16, pp. 1299–1320, Sep. 2013.

[5] S. O. Nakagawa, D. M. Sylvester, J. G. Mcbride, and S.-Y. Oh, "On-Chip Cross Talk Noise Model for Deep-Submicrometer ULSI Interconnect," *Hewlett-Packard J.*, vol. 49, no. 3, pp. 39–45, 1998.

[6] S. Datta, *Quantum transport: Atom to transistor*. Cambridge: Cambridge University Press, 2006.

[7] T.-Y. Kim, N.-M. Park, K.-H. Kim, G. Y. Sung, Y.-W. Ok, T.-Y. Seong, and C.-J. Choi, "Quantum confinement effect of silicon nanocrystals in situ grown in silicon nitride films," *Appl. Phys. Lett.*, vol. 85, no. 22, p. 5355, 2004.

[8] F. Priolo, T. Gregorkiewicz, M. Galli, and T. F. Krauss, "Silicon nanostructures for photonics and photovoltaics.," *Nat. Nanotechnol.*, vol. 9, no. 1, pp. 19–32, Jan. 2014.

[9] A. E. Lim, J. Song, Q. Fang, C. Li, X. Tu, N. Duan, K. K. Chen, R. P. Tern, T. Liow, and A. F. S. Model, "Review of Silicon Photonics Foundry Efforts," *IEEE J. Sel. Top. Quantum Electron.*, vol. 20, no. 4, p. 8300112, 2014.

[10] G. T. Reed, G. Mashanovich, F. Y. Gardes, and D. J. Thomson, "Silicon optical modulators," *Nat. Photonics*, vol. 4, no. 8, pp. 518–526, Jul. 2010.

[11] K. Yamada, T. Tsuchizawa, H. Nishi, R. Kou, T. Hiraki, K. Takeda, H. Fukuda, Y. Ishikawa, K. Wada, and T. Yamamoto, "High-performance silicon photonics technology for telecommunications applications," *Sci. Technol. Adv. Mater.*, vol. 15, no. 2, p. 024603, Apr. 2014.

[12] Q. Xu, B. Schmidt, S. Pradhan, and M. Lipson, "Micrometre-scale silicon electro-optic modulator.," *Nature*, vol. 435, no. 7040, pp. 325–7, May 2005.

[13] M.-C. Tien, J. F. Bauters, M. J. R. Heck, D. J. Blumenthal, and J. E. Bowers, "Ultra-low loss Si3N4 waveguides with low nonlinearity and high power handling capability.," *Opt. Express*, vol. 18, no. 23, pp. 23562–8, Nov. 2010.

[14] Y. A. Vlasov and S. J. Mcnab, "Losses in single-mode silicon-on-insulator strip waveguides and bends," *Opt. Express*, vol. 12, no. 8, pp. 1622–1631, 2004.

[15] K. K. Lee, D. R. Lim, and L. C. Kimerling, "Fabrication of ultralow-loss Si ¯SiO 2 waveguides by roughness reduction," *Opt. Lett.*, vol. 26, no. 23, pp. 1888–1890, 2001.

[16] M. Ghioni, F. Zappa, V. P. Kesan, and J. Warnock, "A VLSI-Compatible High-speed Silicon Photodetector for Optical Data Link Applications," *IEEE Trans. Electron Devices*, vol. 43, no. 7, pp. 1054–1060, 1996.

[17] M. K. Emsley, O. Dosunmu, and M. S. Ünlü, "High-Speed Resonant-Cavity-Enhanced Silicon Photodetectors on Reflecting," *IEEE Photonics Technol. Lett.*, vol. 14, no. 4, pp. 519–521, 2002.

[18] J. Liu, J. Michel, W. Giziewicz, D. Pan, K. Wada, D. D. Cannon, S. Jongthammanurak, D. T. Danielson, L. C. Kimerling, J. Chen, F. O. Ilday, F. X. Kärtner, and J. Yasaitis, "High-performance, tensile-strained Ge p-i-n photodetectors on a Si platform," *Appl. Phys. Lett.*, vol. 87, no. 10, p. 103501, 2005.

[19] Z. Huang, N. Kong, X. Guo, M. Liu, N. Duan, A. L. Beck, S. K. Banerjee, J. C. Campbell, and A. Backside-illuminated, "Photodiode Using Thin SiGe Buffer Layers," *IEEE J. Sel. Top. Quantum Electron.*, vol. 12, no. 6, pp. 1450–1454, 2006.

[20] M. Oehme, J. Werner, E. Kasper, M. Jutzi, and M. Berroth, "High bandwidth Ge p-i-n photodetector integrated on Si," *Appl. Phys. Lett.*, vol. 89, no. 7, p. 071117, 2006.

[21] J. I. Pankove and D. E. Carlson, "Electroluminescence in amorphous silicon," *Appl. Phys. Lett.*, vol. 29, no. 1976, pp. 620–622, 1976.

[22] a. Richter, P. Steiner, F. Kozlowski, and W. Lang, "Current-induced light emission from a porous silicon device," *IEEE Electron Device Lett.*, vol. 12, no. 12, 1991.

[23] F. Namavar, H. P. Maruska, and N. M. Kalkhoran, "Visible electroluminescence from porous silicon np heterojunction diodes," *Appl. Phys. Lett.*, vol. 60, no. 20, pp. 2514–2516, 1992.

[24] M. Bruel, "Silicon on insulator material technology," *Electron. Lett.*, vol. 31, no. 14, pp. 1201–1202, 1995.

[25] K. Tanabe, K. Watanabe, and Y. Arakawa, "III-V/Si hybrid photonic devices by direct fusion bonding.," *Sci. Rep.*, vol. 2, p. 349, Jan. 2012.

[26] H. P. H. Park, a. W. Fang, J. E. Bowers, R. Jones, M. J. Paniccia, and O. Cohen, "An optically pumped silicon evanescent laser operating continuous wave at 60/spl deg/C," *2006 Opt. Fiber Commun. Conf. Natl. Fiber Opt. Eng. Conf.*, pp. 2–4, 2006.

[27] N. W. Ashcroft and N. D. Mermin, *Solid State Physics*. New York: Holt, Rinehart and Winston, 1976.

[28] J. A. Borders, "FORMATION OF SiC IN SILICON BY ION IMPLANTATION," *Appl. Phys. Lett.*, vol. 18, no. 11, p. 509, 1971.

[29] H. J. Round, "A note on carborundum," *Electr. World*, vol. 49, p. 309, 1907.

[30] D. Song, E. C. Cho, G. Conibeer, C. Flynn, Y. Huang, and M. A. Green, "Structural, electrical and photovoltaic characterization of Si nanocrystals embedded in SiC matrix and Si nanocrystals/c-Si heterojunction devices," *Sol. Energy Mater. Sol. Cells*, vol. 92, no. 4, pp. 474–481, 2008.

[31] O. J. Marsh and H. L. Dunlap, "Ion- implanted junctions and conducting layers in SiC," *Radiat. Eff.*, vol. 6, no. 34, pp. 301–311, 1970.

[32] J. A. Edmond, "Blue light emitting diode formed in silicon carbide," US4918497 A1990.

[33] S. Adachi, *Properties of group-IV, III-V and II-VI semiconductors / Sadao Adachi*. Hoboken, NJ: John Wiley & Sons, Ltd., 2005.

[34] L. I. Berger, "Properties of Semiconductors," in *CRC Handbook of Chemistry and Physics*, 95th ed., W. M. Haynes, T. J. Bruno, and D. R. Lide, Eds. Cleveland, OH: CRC Press, 2015, pp. 81–93.

[35] I. Institute, "Silicon Carbide: Thermal Properties." [Online]. Available: view-source:http://www.ioffe.rssi.ru/SVA/NSM/Semicond/SiC/thermal.html. [Accessed: 11-May-2015].

[36] W. D. Kingery, *Introduction to Ceramics*, 2nd ed. New York: Wiley New York, 1976.

[37] H. Morkoç, S. Strite, G. B. Gao, M. E. Lin, B. Sverdlov, and M. Burns, "Large-band-gap SiC, III-V nitride, and II-VI ZnSe-based semiconductor device technologies," *J. Appl. Phys.*, vol. 76, no. 3, pp. 1363–1398, 1994.

[38] R. W. Brander, "The Fabrication of SiC Electroluminescent Displays," *Mater. Res. Bull.*, vol. 4, pp. S187–S198, 1969.

[39] C. A. A. J. Greebe, *The physical properties of grown p-i-n junctions in silicon carbide*. Eindhoven, Netherlands: Philips Research Laboratories, 1963.

[40] M. Ikeda, T. Hayakawa, S. Yamagiwa, H. Matsunami, and T. Tanaka, "Fabrication of 6H-SiC light-emitting diodes by a rotating dipping technique: electroluminescence mechanisms," *J. Appl. Phys.*, vol. 50, no. 1979, pp. 8215–8225, 1979.

[41] R. W. Brander and M. P. Callaghan, "Cathodoluminescence of Ion Implanted SiC," *Phys. Status Solidi*, vol. 3, no. 2, pp. K143–K146, 1970.

[42] D. R. Hamilton, W. J. Choyke, and L. Patrick, "Photoluminescence of nitrogen-exciton complexes in 6H SiC," *Phys. Rev.*, vol. 131, no. 404, pp. 127–133, 1963.

[43] V. V. Artamonov, M. Y. Valakh, N. I. Klyui, V. P. Melnik, A. B. Romanyuk, B. N. Romanyuk, and V. A. Yuhimchuk, "Effect of oxygen on ion-beam induced synthesis of SiC in silicon," *Nucl. Instruments Methods Phys. Res. Sect. B Beam Interact. with Mater. Atoms*, vol. 147, pp. 256–260, 1999.

[44] J. K. . Lindner and B. Stritzker, "Mechanisms in the ion beam synthesis of SiC layers in silicon," *Nucl. Instruments Methods Phys. Res. Sect. B Beam Interact. with Mater. Atoms*, vol. 148, no. 1–4, pp. 528–533, Jan. 1999.

[45] J. Khamsuwan, S. Intarasiri, K. Kirkby, C. Jeynes, P. K. Chu, T. Kamwanna, and L. D. Yu, "High-energy heavy ion beam annealing effect on ion beam synthesis of silicon carbide," *Surf. Coatings Technol.*, vol. 206, no. 5, pp. 770–774, Nov. 2011.

[46] A. Nejim, P. L. F. Hemment, and J. Stoemenos, "SiC buried layer formation by ion beam synthesis at 950 °C," *Appl. Phys. Lett.*, vol. 66, no. 20, pp. 2646–2648, 1995.

[47] P. R. Poudel, B. Rout, D. R. Diercks, Y. M. Strzhemechny, and F. D. Mcdaniel, "Fluence dependant formation of β-SiC by ion implantation and thermal annealing," *Appl. Phys. A*, vol. 104, no. 1, pp. 183–188, Nov. 2010.

[48] D. J. Brink, J. Camassel, and J. B. Malherbe, "Formation of a surface SiC layer by carbon-ion implantation into silicon," *Thin Solid Films*, vol. 449, no. 1–2, pp. 73–79, Feb. 2004.

[49] Y. S. Katharria, S. Kumar, D. Kanjilal, D. Chauhan, J. Ghatak, U. Bhatta, and P. V. Satyam, "Effects of thermal and athermal processing on the formation of buried SiC layers," *J. Appl. Phys.*, vol. 105, no. 1, pp. 0–6, 2009.

[50] Z. An, R. K. Y. Fu, P. Chen, W. Liu, P. K. Chu, and C. Lin, "Fabrication of silicon carbide thin films by plasma immersion ion implantation with self-ignited glow discharge," *Thin Solid Films*, vol. 447–448, no. 03, pp. 153–157, Jan. 2004.

[51] K. Volz, K. Baba, R. Hatada, and W. Ensinger, "Silicon carbide and amorphous carbon film formation by plasma immersion ion implantation: a comparison of methane and toluene as plasma forming gases," *Surf. Coatings Technol.*, vol. 136, no. 1–3, pp. 197–201, Feb. 2001.

[52] W. Liu, M. Zhang, C. Lin, Z. Zeng, L. Wang, and P. K. Chu, "Intense blue-light emission from carbon-plasma-implanted porous silicon," *Appl. Phys. Lett.*, vol. 78, no. 1, pp. 37–39, 2001.

[53] P. Musumeci, L. Calcagno, M. G. Grimaldi, and G. Foti, "Optical properties of defects in ion implanted silicon carbide probed at λ=633 nm," *Appl. Phys. Lett.*, vol. 69, no. 4, p. 468, 1996.

[54] K. Volz and W. Ensinger, "Growth of the carbide, nitride and oxide of silicon by plasma immersion ion implantation," *Surf. Coatings Technol.*, vol. 156, no. 1–3, pp. 237–243, Jul. 2002.

[55] Z. An, R. K. Y. Fu, P. Chen, W. Liu, P. K. Chu, and C. Lin, "Silicon carbide formation by methane plasma immersion ion implantation into silicon," *J. Vac. Sci. Technol. B Microelectron. Nanom. Struct.*, vol. 21, no. 4, pp. 1375–1379, 2003.

[56] H. Dibaji, M. M. Larijani, a. Novinrooz, M. Salehkootahi, R. Afzalzadeh, and S. Noroozian, "The effect of methane dose and post annealing treatment on the formation of nano β-SiC buried layer in the silicon," *Surf. Coatings Technol.*, vol. 203, no. 17–18, pp. 2514–2520, Jun. 2009.

[57] L. Wang, Y. E. Zhao, D. Chen, and S. P. Wong, "Growth kinetics of stoichiometric SiC layers formed by high fluence carbon implantation into silicon using a metal vapor vacuum arc ion source," *Nucl. Instruments Methods Phys. Res. Sect. B Beam Interact. with Mater. Atoms*, vol. 227, pp. 282–288, 2005.

[58] M. Avrami, "Kinetics of Phase Change. I General Theory," *J. Chem. Phys.*, vol. 7, no. 1939, p. 1103, 1939.

[59] M. Nakamura, a. S. Byrne, E. Kitamura, T. Suzuki, S. Nagai, H. Sunaga, Y. Aoki, and H. Naramoto, "Enhanced photoluminescence detection of oxygen in silicon crystal by formation of a carbon–oxygen complex through carbon implantation and electron irradiation," *J. Appl. Phys.*, vol. 78, no. 7, p. 4407, 1995.

[60] F. Durand and J. C. Duby, "Carbon Solubility in Solid and Liquid Silicon- A Review with Reference to Eutectic Equilibrium," *J. Phase Equilibria*, vol. 20, no. 1, pp. 61–63, 1999.

[61] M. R. Brozel, R. C. Newman, and D. H. J. Totterdell, "Interstitial defects involving carbon in irradiated silicon," *J. Phys. C Solid State Phys.*, vol. 8, no. 2, pp. 243–248, 1975.

[62] L. Frey, J. Stoemenos, R. Schork, A. Nejim, and P. L. F. Hemment, "Synthesis of SiC by high temperature C+ implantation into SiO2 - The role of Si/SiO2 interface," *J. Electrochem. Soc.*, vol. 144, no. 12, pp. 4314–4320, 1997.

[63] S. A. Campbell, *Fabrication Engineering at the Micro- and Nanoscale*, 3rd ed. New York: Oxford University Press, 2008.

[64] J. F. Ziegler, *Ion Implantation Science and Technology*, 2000 editi. Edgewater, MD: Ion Implantation Technology Co., 2000.

[65] J. F. Ziegler, J. P. Biersack, and U. Littmark, *The Stopping and Range of Ions in Solids.* New York: Pergamon Press, 1985.

[66] S. Lombardo, a. Cacciato, K. K. Larsen, V. Raineri, F. La Via, V. Privitera, and S. U. Campisano, "High temperature annealing effects on the electrical characteristics of C implanted Si," *J. Appl. Phys.*, vol. 79, no. 7, p. 3464, 1996.

[67] C. Serre, A. Pérez-Rodríguez, A. Romano-Rodríguez, J. R. Morante, R. Kogler, and W. Skorupa, "Spectroscopic characterization plantation in silicon of phases formed by high-dose carbon ion implantation in siliocn," *J. Appl. Phys.*, vol. 77, no. 7, pp. 2978–2984, 1995.

[68] L. Liao, X. M. Bao, N. Li, Z. Yang, and N. Min, "Correlations of optical and structural properties of porous

b-SiC formed on silicon by C+-implantation," *Solid State Commun.*, vol. 95, no. 8, pp. 559–562, 1995.

[69] P. R. Poudel, P. P. Poudel, B. P. Sharma, J. Y. Hwang, M. El Bouanani, B. Rout, and F. D. McDaniel, "Synthesis of buried layers of β-SiC in Si by multiple energy carbon ion implantations and post thermal annealing," *Thin Solid Films*, vol. 524, pp. 35–38, Dec. 2012.

[70] D. J. Oostra, J. Politiek, C. W. T. Bulle-Lieuwma, D. E. W. Vandenhoudt, and P. C. Zalm, "Can Carbon-implanted Silicon be Applied as Wide-bandgap Emitter," *J. Mater. Res.*, vol. 11, no. 7, pp. 1653–1658, 1996.

[71] P. R. Poudel, B. Rout, D. R. Diercks, J. A. Paramo, Y. M. Strzhemechny, and F. D. Mcdaniel, "Effects of Thermal Annealing on the Formation of Buried β-SiC by Ion Implantation," *J. Electron. Mater.*, vol. 40, no. 9, pp. 1998–2003, Jun. 2011.

[72] L. Liao, X. M. Bao, Z. Yang, and N. Min, "Intense blue emission from porous β-SiC formed on C+-implanted silicon," *Appl. Phys. Lett.*, vol. 66, no. 18, p. 2382, 1995.

[73] X. M. Bao, L. Liao, N. Li, N. Min, Y. Gao, and Z. Zhang, "The formation and microstructures of Si-based blue-light emitting porousB-SiC," *Nucl. Instruments Methods Phys. Res. Sect. B Beam Interact. with Mater. Atoms*, vol. 119, pp. 505–509, 1996.

[74] N. Li, X. Wu, L. Liao, and X. M. Bao, "The electroluminescence from porous β-SiC formed on C+ implanted silicon," *Nucl. Instruments Methods Phys. Res. Sect. B Beam Interact. with Mater. Atoms*, vol. 142, no. 3, pp. 308–312, Jul. 1998.

[75] B. Garrido, M. Lopez, S. Ferre, A. Romano-Rodriguez, A. Perez-Rodriguez, P. Ruterana, and J. R. Morante, "Visible photoluminescence of SiO2 implanted with carbon and silicon," *Nucl. Instruments Methods Phys. Res. Sect. B Beam Interact. with Mater. Atoms*, vol. 120, pp. 101–105, 1996.

[76] L. T. Canham, "Silicon quantum wire array fabrication by electrochemical and chemical dissolution of wafers," *Appl. Phys. Lett.*, vol. 57, no. 10, p. 1046, 1990.

[77] R. K. Endo, Y. Fujihara, and M. Susa, "Calculation of the density and heat capacity of silicon by molecular dynamics simulation," *High Temp. Press.*, vol. 35/36, no. 5, pp. 505–511, 2003.

[78] M. Deguchi, M. Kitabatake, T. Hirao, N. Arai, and T. Izumi, "Synthesis of ß-SiC layer in silicon by carbon ion 'hot' implantation," *Japanese J. Appl. Physics, Part 1 Regul. Pap. Short Notes Rev. Pap.*, vol. 31, pp. 343–347, 1992.

[79] K. J. Reeson, "Mechanism of buried β-SiC formation by implanted carbon in silicon," *Thin Solid Films*, vol. 191, no. 1, p. 147, 1990.

[80] A. Pérez-Rodríguez, R. Kogler, L. Clavo-Barrio, C. Serre, A. Romano-Rodríguez, V. Heera, W. Skorupa, and J. R. Morante, "Ion beam assisted recrystallization of SiC/Si structures," *Nucl. Instruments Methods Phys. Res. Sect. B Beam Interact. with Mater. Atoms*, vol. 112, no. 4, pp. 334–337, 1996.

[81] W. G. Spitzer, D. A. Kleinman, and C. J. Frosch, "Infrared properties of cubic silicon carbide films," *Phys. Rev.*, vol. 113, no. 1, pp. 133–137, 1959.

[82] W. G. Spitzer, D. Kleinman, and D. Walsh, "Infrared properties of hexagonal silicon carbide," *Phys. Rev.*, vol. 113, no. 1, pp. 127–132, 1959.

[83] A. Ferrari and J. Robertson, "Interpretation of Raman spectra of disordered and amorphous carbon," *Phys. Rev. B*, vol. 61, no. 20, pp. 14095–14107, 2000.

[84] P. Martin, B. Daudin, M. Dupuy, a. Ermolieff, M. Olivier, a. M. Papon, and G. Rolland, "High-temperature

ion beam synthesis of cubic SiC," *J. Appl. Phys.*, vol. 67, no. 1990, p. 2908, 1990.

[85] H. Munekata and H. Kukimoto, "Electroluminescence in hydrogenated amorphous siliconcarbon alloy," *Appl. Phys. Lett.*, vol. 42, no. 5, pp. 432–434, 1983.

[86] E. Rotem, J. M. Shainline, and J. M. Xu, "Electroluminescence of nanopatterned silicon with carbon implantation and solid phase epitaxial regrowth.," *Opt. Express*, vol. 15, no. 21, pp. 14099–106, Oct. 2007.

[87] A. P. Baraban and Y. V. Petrov, "Charge state of luminescence centers in the Si-SiO2 structures subjected to sequential implantation with silicon and carbon ions," *Semiconductors*, vol. 42, no. 13, pp. 1515–1518, Dec. 2008.

[88] M. Ghezzo, D. M. Brown, E. Downey, J. Kretchmer, W. Hennessy, D. L. Polla, and H. Bakhru, "Nitrogen-Implanted S i c Diodes Using High-Temperature Implantation," *IEEE electron device Lett.*, vol. 13, no. 12, pp. 639–641, 1992.

[89] S. K. Purdy, A. P. Knights, M. P. Bradley, and G. S. Chang, "Light-Emitting Diodes Fabricated From Carbon Ions Implanted Into p-Type Silicon," *IEEE Trans. Electron Devices*, vol. 62, no. 3, pp. 914–918, 2015.

[90] J. R. McLeod, "Fabrication and Characterization of Nanocrystalline Silicon LEDs: A Study of the Influence of Annealing," University of Saskatchewan, 2014.

[91] P. R. Desautels, "Fabrication of Electroluminescent Silicon Diodes by Plasma Ion Implantation," Universit of Saskatchewan, 2009.

[92] S. J. Moloi and M. McPherson, "Current-voltage behaviour of Schottky diodes fabricated on p-type silicon for radiation hard detectors," *Phys. B Condens. Matter*, vol. 404, no. 16, pp. 2251–2258, 2009.

[93] H. P. Maruska, F. Namavar, and N. M. Kalkhoran, "Current injection mechanism for porous-silicon transparent surface light-emitting diodes," *Appl. Phys. Lett.*, vol. 61, no. 11, pp. 1338–1340, 1992.

[94] D. B. Dimitrov, "Current-voltage chracteristics of porous-silicon layers," *Phys. Rev. B*, vol. 51, no. 3, pp. 1562–1566, 1995.

[95] L. Magafas, N. Georgoulas, and A. Thanailakis, "Electrical properties of a-SiC/c-Si(p) heterojunctions," *Semicond. Sci. Technol.*, vol. 7, pp. 1363–1368, 1992.

[96] J. Hadzi-Vukovic, M. Jevtic, H. Rothleitner, and P. Del Croce, "Si and SiC Schottky diodes in smart power circuits: a comparative study by I – V – T and C – V measurements," *J. Phys. Conf. Ser.*, vol. 10, pp. 11–14, Jan. 2005.

[97] G. G. Qin, Y. M. Huang, B. Q. Zong, L. Z. Zhang, and B. R. Zhang, "A Comparison Study of Electroluminescence from Au/Native Oxide/P-Si and Au/Porous Si Diodes," *Superlattices Microstruct.*, 1994.

[98] T. Futagi, T. Matsumoto, M. Katsuno, Y. Ohta, H. Mimura, and K. Kitamura, "Visible light emission from a pn junction of porous silicon and microcrystalline silicon carbide," *Appl. Phys. Lett.*, vol. 63, no. 9, p. 1209, 1993.

[99] V. Aubry and F. Meyer, "Schottky diodes with high series resistance:," *J. Appl. Phys.*, vol. 76, no. 12, pp. 7973–7984, 1994.

[100] F. Chen, Y. Zhang, H. Lü, Y. Zhang, H. Guo, and X. Guo, "Fabrication and characteristics of a 4H-SiC junction barrier Schottky diode," *J. Semicond.*, vol. 32, no. 6, p. 064003, Jun. 2011.

[101] D. K. Schroder, *MATERIAL AND DEVICE SEMICONDUCTOR MATERIAL AND DEVICE Third Edition*, 3rd ed. Hoboken, NJ: John Wiley & Sons, Inc., 2006.

[102] R. W. Brander and R. P. Sutton, "Solution grown SiC p-n junctions," *J. Phys. D. Appl. Phys.*, vol. 2, no. 2, pp. 309–318, 1969.

[103] H. Y. Tai, C. H. Cheng, and G. R. Lin, "Blue-green light emission from Si and SiC quantum dots co-doped Si-Rich SiC p-i-n junction diode," *IEEE J. Sel. Top. Quantum Electron.*, vol. 20, no. 4, 2014.

[104] E. W. Williams and R. Hall, *Luminescence and the Light Emitting Diode*. Toronto, Ontario, Canada: Pergamon Press, 1978.

[105] T. Matsumoto, J. Takahashi, T. Tamaki, T. Futagi, H. Mimura, and Y. Kanemitsu, "Blue-green luminescence from porous silicon carbide," *Appl. Phys. Lett.*, vol. 64, no. 2, p. 226, 1994.

[106] W. A. Nevin, H. Yamagishi, M. Yamaguchi, and Y. Tawada, "Emission of blue light from hydrogenated amorphous silicon carbide," *Nature*, vol. 326, no. 6471, pp. 529–531, 1994.

[107] A. O. Konstantinov, A. Henry, C. I. Harris, and E. Janzén, "Photoluminescence studies of porous silicon carbide," *Appl. Phys. Lett.*, vol. 66, no. 17, pp. 2250–2252, 1995.

[108] T. Ma, J. Xu, K. Chen, J. Du, W. Li, and X. Huang, "Red–green–blue light emission from hydrogenated amorphous silicon carbide films prepared by using organic compound xylene as carbon source," *Appl. Phys. Lett.*, vol. 72, no. 1, p. 13, 1998.

[109] T. V. Torchynska, A. Díaz Cano, S. Jiménez Sandoval, M. Dybic, S. Ostapenko, and M. Mynbaeva, "Photoluminescence and Raman spectroscopy in porous SiC," *Microelectronics J.*, vol. 36, no. 3–6, pp. 536–538, Mar. 2005.

[110] D. Chen, Z. M. Liao, L. Wang, H. Z. Wang, F. Zhao, W. Y. Cheung, and S. P. Wong, "Photoluminescence from β-SiC nanocrystals embedded in SiO2 films prepared by ion implantation," *Opt. Mater. (Amst).*, vol. 23, no. 1–2, pp. 65–69, Jul. 2003.

[111] G. G. Qin, Y. M. Huang, J. Lin, L. Z. Zhang, B. Q. Zong, and B. R. Zhang, "Electroluminescence from Au/native oxide/p-Si and its correlation to that from Au/porous Si," *Solid State Commun.*, vol. 94, no. 8, pp. 607–612, May 1995.

[112] H. Mimura, T. Matsumoto, and Y. Kanemitsu, "Blue electroluminescence from porous silicon carbide," *Appl. Phys. Lett.*, vol. 65, no. 26, pp. 3350–3352, 1994.

[113] A. Pérez-Rodríguez, O. González-Varona, B. Garrido, P. Pellegrino, J. R. Morante, C. Bonafos, M. Carrada, and A. Claverie, "White luminescence from Si[sup +] and C[sup +] ion-implanted SiO[sub 2] films," *J. Appl. Phys.*, vol. 94, no. 1, pp. 254–262, 2003.

[114] P. P. Altermatt, J. Schmidt, G. Heiser, and A. G. Aberle, "Assessment and parameterisation of Coulomb-enhanced Auger recombination coefficients in lowly injected crystalline silicon," *J. Appl. Phys.*, vol. 82, no. 10, p. 4938, 1997.

[115] W. Shockley and W. T. Read, "Statistics of the Recombination of Holes and Electrons," *Phys. Rev.*, vol. 87, no. 46, pp. 835–842, 1952.

[116] T. Searle, Ed., *Properties of Amorphous Silicon and its Alloys*. London, UK: INSPEC, The Institue of Electrical Engineers, 1998.

[117] D. J. Lockwood, Z. Lu, and J. Baribeau, "Quantum confined luminescence in Si/SiO2 superlattices.," *Phys. Rev. Lett.*, vol. 76, no. 3, pp. 539–541, Jan. 1996.

[118] Z. H. Lu, D. J. Lockwood, and J. Baribeau, "Quantum confinement and light emission in SiO2/Si superlattices," *Nature*, vol. 378, no. 16, pp. 258–260, 1995.

[119] P. Van Mieghem, "Theory of band tails in heavily doped semiconductors," *Rev. Mod. Phys.*, vol. 64, no. 3, pp. 755–793, 1992.

[120] D. J. Lockwood and A. G. Wang, "Quantum Confinement induced photoluminescence in porous silicon," *Solid State Commun.*, vol. 94, no. 11, pp. 905–909, 1995.

[121] R. Dick, *Advanced Quantum Mechanics: Materials and Photons*. New York: Springer, 2012.

[122] C. Kittel, *Introduction to Solid State Physics*. New Caledonia: John Wiley & Sons, Inc., 2005.

[123] A. D. Yoffe, "Low-dimensional systems: quantum size effects and electronic properties of semiconductor microcrystallites (zero-dimensional systems) and some quasi-two-dimensional systems," *Adv. Phys.*, vol. 42, no. 2, pp. 173–262, 1993.

[124] J. Zhu, Z. Liu, X. L. Wu, L. L. Xu, W. C. Zhang, and P. K. Chu, "Luminescent small-diameter 3C-SiC nanocrystals fabricated via a simple chemical etching method," *Nanotechnology*, vol. 18, no. 36, p. 365603, 2007.

[125] J. P. Proot, C. Delerue, and G. Allan, "Electronic structure and optical properties of silicon crystallites: Application to porous silicon," *Appl. Phys. Lett.*, vol. 61, no. 16, pp. 1948–1950, 1992.

[126] E. G. Barbagiovanni, D. J. Lockwood, P. J. Simpson, and L. V Goncharova, "Quantum confinement in Si and Ge nanostructures : Theory and experiment Quantum confinement in Si and Ge nanostructures : Theory and experiment," vol. 011302, 2014.

[127] L. E. Brus, "Luminescence of Silicon Materials: Chains, Sheets, Nanocrystals, Nanowires, Microcrystals and Porous Silicon," *J. Phys. Chem.*, vol. 98, pp. 3575–3581, 1994.

[128] X. L. Wu, J. Y. Fan, T. Qiu, X. Yang, G. G. Siu, and P. K. Chu, "Experimental evidence for the quantum confinement effect in 3C-SiC nanocrystallites," *Phys. Rev. Lett.*, vol. 94, no. 2, pp. 026102–1, 2005.

[129] H. S. Mansur, "Quantum dots and nanocomposites.," *Wiley Interdiscip. Rev. Nanomed. Nanobiotechnol.*, vol. 2, no. 2, pp. 113–29, 2010.

[130] a. D. Yoffe, "Semiconductor quantum dots and related systems: Electronic, optical, luminescence and related properties of low dimensional systems," *Adv. Phys.*, vol. 50, no. 1, pp. 1–208, 2001.

[131] L. Pavesi, M. Ceschini, G. Mariotto, E. Zanghellini, O. Bisi, M. Anderle, L. Calliari, M. Fedrizzi, and L. Fedrizzi, "Spectroscopic investigation of electroluminescent porous silicon," *J. Appl. Phys.*, vol. 75, no. 2, p. 1118, 1994.

[132] L. Pavesi, M. Ceschini, and H. E. Roman, "Recombination dynamics in porous silicon," *Thin Solid Films*, vol. 255, no. 1–2, pp. 67–69, Jan. 1995.

[133] M. Wolkin, J. Jorne, P. Fauchet, G. Allan, and C. Delerue, "Electronic States and Luminescence in Porous Silicon Quantum Dots: The Role of Oxygen," *Phys. Rev. Lett.*, vol. 82, no. 1, pp. 197–200, Jan. 1999.

[134] J. Liu, S. Sundar Kumar Iyer, C. Hu, N. W. Cheung, R. Gronsky, J. Min, and P. Chu, "Formation of buried oxide in silicon using separation by plasma implantation of oxygen," *Appl. Phys. Lett.*, vol. 67, no. 16, p. 2361, 1995.

[135] J. M. Moyer, "Method of making p-n junction semiconductor unit," US2842466 A.

[136] W. Shockley, “Forming semiconductive devices by ionic bombardment,” 2787564.

[137] P. K. Chu, N. W. Cheung, C. Chan, B. Mizuno, and O. R. Monteiro, “Semiconductor Applications,” in *Handbook of Plasma Immersion Ion Implantation and Deposition*, A. Anders, Ed. New York: John Wiley & Sons, Inc., 2000.

[138] M. A. Lieberman and A. J. Lichtenberg, *Principles of Plasma Discharges and Materials Processing*. New York: John Wiley & Sons, Inc., 1994.

[139] M. a. Lieberman, “Model of plasma immersion ion implantation,” *J. Appl. Phys.*, vol. 66, no. 7, p. 2926, 1989.

[140] M. Risch and M. P. Bradley, “Prospects for band gap engineering by plasma ion implantation,” *Phys. Status Solidi*, vol. 6, no. S1, pp. S210–S213, May 2009.

[141] V. Herr, “A diamond cubic crystal viewed from the <110> direction, showing hexagonal ion channels.,” 2001. [Online]. Available: https://en.wikipedia.org/wiki/Ion_implantation#/media/File:Diamond_structure.png. [Accessed: 27-Mar-2014].

[142] J. F. Ziegler, “Particle interactions with matter.” .

[143] F. H. Stillinger and T. A. Weber, “Computer simulation of local order in condensed phases of silicon,” *Phys. Rev. B*, vol. 31, no. 8, pp. 5262–5271, 1985.

[144] G. Dearnaley, J. H. Freeman, Nelson, R. S., and J. Stephen, *Ion Implantation.* New York: American Elsevier Publishing Company, Inc., 1973.

[145] J. T. Anstey, “A Study of the Light Emission from SiNx Films,” McMaster University, 2011.

[146] M. Risch, “The Promise of Nitrogen Plasma Implanted Gallium Arsenide for Band Gap Engineering,” University of Saskatchewan, 2008.

[147] M. P. Bradley, P. R. Desautels, D. Hunter, and M. Risch, “Silicon electroluminescent device production via plasma ion implantation,” *Phys. Status Solidi*, vol. 6, no. S1, pp. S206–S209, May 2009.

[148] M. P. Bradley and C. J. T. Steenkamp, “Time-Resolved Ion and Electron Current Measurements in Pulsed Plasma Sheaths,” *IEEE Trans. Plasma Sci.*, vol. 34, no. 4, pp. 1156–1159, Aug. 2006.

[149] C. J. T. Steenkamp and M. P. Bradley, “Active Charge / Discharge IGBT Modulator for Marx Generator and Plasma Applications,” vol. 35, no. 2, pp. 473–478, 2007.

[150] F. Neri, F. Barreca, E. Fazio, E. Barletta, G. Mondio, S. Trusso, B. Brendebach, and H. Modrow, “Influence of the deposition parameters on the electronic and structural properties of pulsed laser ablation prepared Si[sub 1−x]C[sub x] thin films,” *J. Vac. Sci. Technol. A Vacuum, Surfaces, Film.*, vol. 25, no. 1, pp. 117–125, 2007.

[151] J. Narayan and O. W. Holland, “Growth in Ion-Implanted Silicon,” *Phys. Status Solidi*, vol. 73, no. 1, pp. 225–236, 1982.

[152] P. R. Desautels, M. P. Bradley, C. J. T. Steenkamp, and J. Mantyka, “Electroluminescence in plasma ion implanted silicon,” *Phys. Status Solidi*, vol. 206, no. 5, pp. 985–988, May 2009.

[153] N. B. Colthup, L. H. Daly, and S. E. Wiberley, *Introduction to Infrared and Raman Spectroscopy*, Third. San Diego, USA: Academic Press, Inc., 1990.

[154] Y. Wang, D. C. Alsmeyer, and R. L. McCreery, “Raman Spectroscopy of Carbon Materials: Structural Basis of Observed Spectra,” *Chem. Mater.*, vol. 2, no. 5, pp. 557–563, 1990.

[155] J. Als-Nielsen, *Elements of modern X-ray physics*. New York, USA: Wiley, 2001.

[156] J. Britten, “McMaster Analytical X-Ray Diffraction Facility (MAX).” [Online]. Available: http://www.chemistry.mcmaster.ca/facilities/xray. [Accessed: 17-Aug-2015].

[157] C. F. Macrae, I. J. Bruno, J. A. Chisholm, P. R. Edgington, P. McCabe, and E. Pidcock, “Mercury CSD 2.0 - New Features for the Visualization and Investigation of Crystal Structures,” *J. Appl. Crystallogr.*, vol. 41, no. 2, pp. 466–470, 2008.

[158] S. Bals, B. Kabius, M. Haider, V. Radmilovic, and C. Kisielowski, “Annular dark field imaging in a TEM,” *Solid State Commun.*, vol. 130, pp. 675–680, 2004.

[159] S. J. Pennycook, “Z-contrast stem for materials science,” *Ultramicroscopy*, vol. 30, pp. 58–69, 1989.

[160] D. E. Jesson and S. J. Pennycook, “Incoherent Imaging of Crystals Using Thermally Scattered Electrons,” *Proc. R. Soc. A Math. Phys. Eng. Sci.*, vol. 449, no. 1936, pp. 273–293, 1995.

[161] “FEI Titan 80-300 HB,” *McMaster University - Canadian Centre for Electron Microscopy*. [Online]. Available: http://ccem.mcmaster.ca/equipment-titan1.shtml. [Accessed: 17-Aug-2015].

[162] Z. Iqbal and S. Veprek, “Raman scattering from hydrogenated microcrystalline and amorphous silicon,” *J. Phys. C Solid State Phys.*, vol. 15, no. 2, pp. 377–392, 1982.

[163] K. W. Cheah, T. Chan, W. L. Lee, D. Teng, W. H. Zheng, and Q. Wang, “Multiple peak photoluminescence of porous silicon,” *Appl. Phys. Lett.*, vol. 63, no. 25, pp. 3464–3466, 1993.

[164] A. F. Zatsepin, E. A. Buntov, V. S. Kortov, D. I. Tetelbaum, A. N. Mikhaylov, and A. I. Belov, “Mechanism of quantum dot luminescence excitation within implanted SiO2:Si:C films.,” *J. Phys. Condens. Matter*, vol. 24, no. 4, p. 045301, Feb. 2012.

[165] H. Mimura, T. Matsumoto, and Y. Kanemitsu, “Light emitting devices using porous silicon and porous silicon carbide,” *Solid. State. Electron.*, vol. 40, no. 1–8, pp. 501–504, Jan. 1996.

[166] Y. Chao and E. Anglia, “Optical Properties of Nanostructured Silicon,” in *Comprehensive Nanoscience and Technology*, Oxford: Elsevier, 2011, pp. 543–570.

[167] B. Lojek, “A Light-Induced Annealing of Silicon Implanted Layers,” *Mater. Sci. Forum*, vol. 573–574, pp. 229–235, 2008.